Label-free optical biosensing with InGaAsP photonic crystal membrane nanocavities by means of photoluminescence

Ryckebosch, E.C.I.

Award date:
2009

Label-free optical biosensing with InGaAsP photonic crystal membrane nanocavities by means of photoluminescence

E.C.I. Ryckebosch

December 2009

Master thesis at the Department of Applied Physics
Photonics & Semiconductor Nanophysics
in cooperation with Molecular Biosensors for Medical Diagnostics

Supervisors:

M.Sc. Mehmet A. Dündar PSN
Dr. Leo J. van IJzendoorn MBx
Dr. Rob W. van der Heijden PSN

Professor:

Prof. Dr. Andrea Fiore

Abstract

A strong need exists for very small, multiplexed and sensitive optical biosensors for applications in pharmaceutical research, medical diagnostics, environmental monitoring and homeland security. Photonic crystal membrane nanocavities are a promising platform because their resonance spectra are highly sensitive to changes in the ambient refractive index. Using current semiconductor technologies, large arrays of nanocavities can be integrated to realize a lab-on-a-chip. Because the cavities have wavelength-sized dimensions, ultra-small sample volumes are sufficient.

In this report, the systematic investigation of the sensitivities of several types of InGaAsP photonic crystal membrane nanocavities with embedded InAs quantum dots is described. Proof is given that these nanocavities can be completely filled with aqueous solutions while the aqueous environment does not inhibit the detection of the resonance spectra. The sensitivities are dependent on the dimensions of the nanocavity, with smaller cavity types yielding higher sensitivities, and on the position of the cavity modes with respect to the photonic crystal band gap. Furthermore, the inverse correlation between sensitivity and quality factor, which affects the detection limit, was observed.

The functionalization of InGaAsP photonic crystal membrane nanocavities with proteins that act as a probe, and the subsequent label-free detection of target proteins was also investigated. It was found that functionalization of the membrane surface is possible, as well as the label-free detection, but both need further optimization.

From this work guidelines are obtained for the design of photonic crystal membrane nanocavity biosensors.

Contents

Chapter 1

Introduction

The goal of this master project is to investigate label-free optical biosensing with InGaAsP photonic crystal membranes. To understand the meaning of each of these words, an introduction is given to both optical biosensing and photonic crystals. Next, the aims of this project are formulated together with a motivation and this chapter ends with an overview of the structure of the report.

1.1 Biosensors

Generally, a biosensor consists of a substrate onto which probe molecules are attached and a transducer. When target molecules bind specifically to the probe molecules, the transducer translates this binding into a physical signal that can be detected. This signal can be either optical, mechanical, electrical or magnetical. An example of biochemical recognition in the form of an immunoassay is given in Figure 1.1. The sensor surface is functionalized with one type of antibodies, to which only antigens with a circular hole can bind. When a sample containing different types of antigens is applied, only antigens with circular holes will bind.

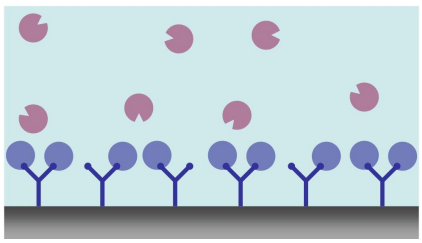

Figure 1.1: *A schematic representation of an immunoassay with biochemical recognition between antibodies and antigens.*

The development of next generation biosensors focusses on fulfilling three basic requirements: good sensor performance, multiplexing, low complexity and cost. The sensor performance is quantified by the detection limit and the

test sensitivity and the test specificity. Ideally, when performing for example an immunoassay as in Figure 1.1, all the antigens with circular holes should bind to the antibodies and no antigen with a triangular holes should bind. In practice, this is not always true; there will be antigens with circular holes that do not bind while some antigens with triangular holes do bind. The test sensitivity and specificity are a measure for these biding errors. The test sensitivity is defined as the number of antigens with circular holes that were bound divided by the total number of antigens with circular holes and the test specificity is given by the number of antigens with triangular holes that did not bind divided by the total number of antigens with triangular holes. In the ideal sensor, as well the test sensitivity as specificity are equal to one. The second requirement is that the new technology platform needs to have a high degree of multiplexing capabilities to maximize the number of biomolecules a sample can be tested for. To conclude, it also is important to minimize the steps in the sensor fabrication process and the sample preparation in order to have a commercially viable sensor platform.

1.2 Optical sensing and optofluidic systems

Optical sensors are sensors in which the biorecognition between two molecules is transduced into a detectable optical signal. Based on the detection of this signal, optical sensors can be categorized in two groups: fluorescence-based detectors and label-free detectors. When detection is fluorescence-based, either the target or a secondary probe molecule are labeled with a fluorescent tag. Figure 1.2 (a) shows a fluorescence-based immunoassay in which the secondary probe molecules are labeled. After binding the target antigens to the antibodies on the sensor surface, a washing step is performed after which a solution containing a second antibody, tagged with a fluorescent label, is applied. When the unbound secondary antibodies are washed away, the intensity of the fluorescence is a measure for the number of target antigens. With florescence-based detection even single molecules can be detected [1], but the disadvantages are the difficulty of labeling the molecules with the risk of changing their three-dimensional conformation and thus their biochemical recognition abilities and the necessity of washing steps to remove unbound molecules and unbound labeled biorecognition molecules.

These disadvantages do not play a role in label-free optical sensing. There are several detection methods for label-free optical sensing like optical absorption and Raman spectroscopic detection but this report focusses on refractive index sensing. For most label-free optical detectors, the light that is used to detect is concentrated near the sensor surface as is shown in Figure 1.2 (b). The evanescent field of this light decays exponentially away from the surface with a decay length of the order of tens to hundreds of nanometers. For the

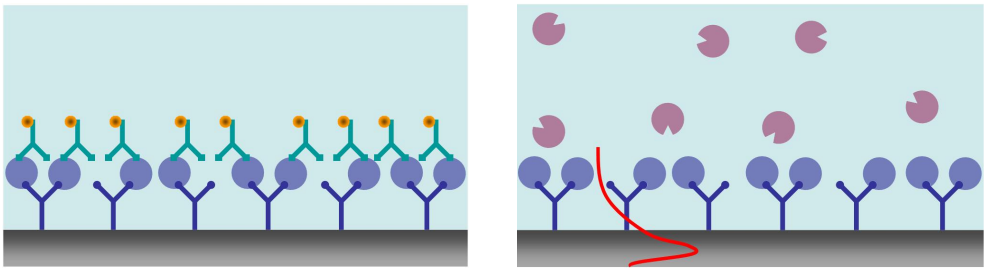

(a) (b)

Figure 1.2: *A schematic representation of (a) an immunoassay based on fluorescence detection fluorescence-based and (b) an immunoassay based on label-free detection with the evanescent tail of the light at the sensor surface.*

immunoassay of Figure 1.2 (b), where both the antibody and antigen have dimensions of the order of tens to hundreds of Angströms, this evanescent tail is able to detect the binding. Also in other configurations, the decay length is larger than the dimensions at which the binding takes place.

Refractive index sensing optical sensors can detect the small increase in refractive index when a target molecule binds to a probe but they can also detect changes in the refractive index of a bulk solution. In this report, the detection with bulk solutions is referred to as chemical sensing. The sensitivities of refractive index optical sensors are expressed in nanometers per refractive index unit (RIU). This sensitivity is not the same as the test sensitivity of paragraph 1.1 but they are related. Increasing the sensitivity in nm/RIU is a way to increase the test sensitivity [2].

Refractive index based label-free optical biosensors enclose different technology platforms like surface plasmon resonance (SPR), interferometer, ring resonator, optical fiber, waveguide and photonic crystal based biosensors. Since 2000, several optical biosensor devices have become commercially available but they are mostly based on SPR, interferometry or waveguides [3]. In the Appendix an overview is given of the detection limits of different designs of each platform. The lowest detection limits of each platform are approximately 10^{-7} RIU for bulk refractive index sensing which is one to two orders lower than for photonic crystal based biosensors. However it is possible for photonic crystal based biosensors to obtain similar values for the detection limit. The main advantage of photonic crystal based biosensors is that they have very small dimensions compared to the other platforms. Therefore sample volumes of only 0.1 to 1 fL are sufficient to do bulk refractive index measurements. In the tables in the Appendix, detection limits are given for bulk solutions and protein/bacteria/virus measurements.

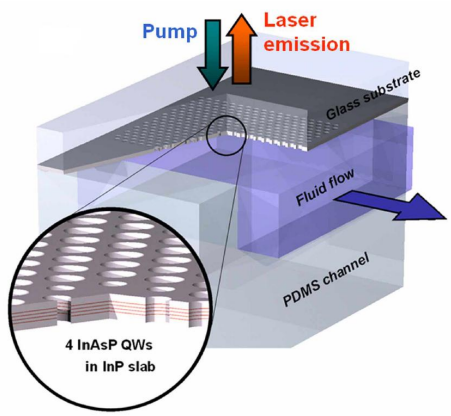

Figure 1.3: *Schematic representation of the microfluidic integration of a photonic crystal membrane cavity using polydimethylsiloxane (PDMS) [8].*

For optical biosensors to develop from the research area to practical applications, optofluidic integration is necessary. Several review papers can be found in literature on this subject [4–6]. Most of the microfluidic fabrication methods have been with soft lithography since it allows for easy and cheap fabrication of complex microfluidic structures while the material has a good optical transparency and quality [4, 7]. Also for photonic crystal membrane cavities examples of microfluidic integration can be found in literature [8–11].

There are currently three major target groups that can benefit from improving optical sensors for multi target sensing or for continuous monitoring [12]. First of all, the medical (and veterinary) diagnostics would benefit from both a multiplexed diagnostics device with biomarkers for specific diseases but also from a diagnostic technique for point-of-care (i.e. at the doctors office instead of in a lab) and self-testing purposes. There are already commercial optical biosensors that test for infectious diseases or heart attack markers, and alcohol or drugs abuse [13]. Secondly, homeland security agencies all over the world would benefit from a means to identify biothreats and explosives detection. Currently, the technology to detect biothreats exists and similar technologies are being tested for explosives detection and the tracking of both biothreats and explosives [14]. The third group consists of environmental regulatory agencies and heavily polluting or chemical factories. The factories need on-site monitoring systems to reduce the response time in case of pollution or the release of dangerous substances while the environmental agencies are mostly interested in optical biosensors for the monitoring of air, water and soil. Currently, there are already a lot of different optical sensors for environmental monitoring commercially available; examples can be found in [15, 16]

1.3 Photonic crystals

A photonic crystal is a periodic dielectric structure that has, as a result of this periodicity, a photonic band gap. The easiest way to explain the occurrence of the photonic band gap is to make the analogy between photons in a photonic crystal and electrons in a semiconductor crystal. In a semiconductor, the waves of electrons scatter at each layer of atoms they encounter. The scattered waves will interfere constructively if the de Broglie wavelength of the electron waves, given by $\lambda = \frac{h}{mv}$ with h Plancks constant, m the electron mass and v the speed of the electron, is close to the distance d between successive atom layers which is of the order of Ångströms. When this constructive interference, i.e. reflection, occurs over a range of wavelengths and in all directions through the crystal, one can say that these wavelengths are forbidden. This band of forbidden states is referred to as the electronic band gap.

Analogously, photonic crystals are composed of periodically arranged dielectric structures with a periodicity that is of the same order as the wavelengths of the photons one wishes to use for a specific application. This means that the periodicity can be centimeters (microwaves) or hundreds of nanometers (visible light), but always large compared to semiconductor crystals. When photons travel through the photonic crystal, there will be constructive or destructive interference of the waves depending on the direction in which they travel through the crystal, the refractive index and the periodicity of the crystal. Like with electrons in a semiconductor, a band with forbidden wavelengths arises which is called the photonic band gap. By locally disrupting the photonic crystal periodicity, locally states are created within the forbidden band just like doping does in semiconductors.

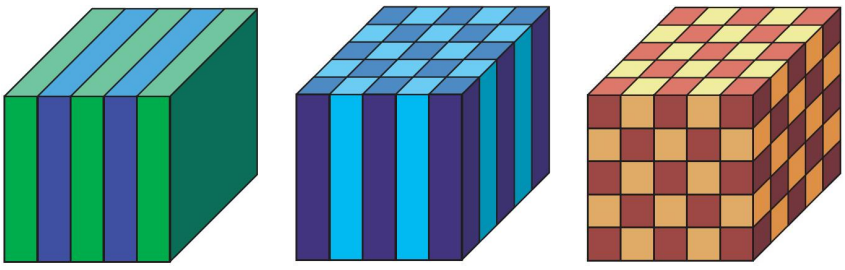

(a) (b) (c)

Figure 1.4: *Periodicity in one, two or three directions leads to (a) 1D photonic crystals, (b) 2D photonic crystals and (c) 3D photonic crystals [17].*

Photonic crystals can have one-dimensional (1D), two-dimensional (2D) or three-dimensional (3D) periodicity as is schematically shown in Figure 1.4. The simplest form of a photonic crystal is the one in Figure 1.4 (a) which is a one-dimensional periodic structure called a Bragg mirror. The propagation

of light through these structures was first studied by Lord Rayleigh in 1887 [18] who demonstrated the existence of a band gap. However, it was only in 1987 that Yablonovitch and John suggested the possibility of two- and three-dimensional periodic crystals with respectively two- and three-dimensional band gaps [19, 20]. A schematic representation of 2D and 3D periodicity is given in Figures 1.4 (b) and (c).

It took Yablonovitch until 1991 to produce for the first time a 3D photonic crystal [21]. This was only for electromagnetic waves in the microwave region since the dielectric structure had a periodicity of the order of millimeters. After this first proof of principle other groups tried different configurations which were all in the microwave regime since the scaling down of these structures proved to be very difficult [22]. Therefore Krauss et al. used techniques form the semiconductor industry to fabricate 2D photonic crystals at near-infrared wavelengths in 1996 [23]. Since then 2D photonic crystals have been made all over the world for various purposes ranging from the guiding, bending, and splitting of light to the slowing down of light and many others. In 2000, Noda et al. were successful at scaling down a 3D structure from the microwave to the near-infrared regime using advanced semiconductor techniques [24]. However this is not a mature fabrication process so if 3D confinement is necessary, it is advisable to use photonic crystals that have a 2D confinement due to their periodicity and that are so thin that total internal reflection occurs which confined the light in the third direction. This method combines (almost) 3D confinement with fabrication techniques that have become common knowledge.

As stated above, introducing a local defect, referred to as a cavity, into the photonic crystal periodicity locally changes the allowed wavelengths. Light of these wavelengths will reflect at the edges of the cavity so actually, by creating a defect an optical resonator is made. A resonator is characterized by its resonance spectrum and the wavelengths at which it resonates are, among other things, determined by the refractive index difference between the dielectric and the environment. This means that photonic crystal cavities can be used as refractive index sensing optical sensors.

1.4 Goal and motivation of this project

The main goal of this project is to develop photonic crystal membrane nanocavity based sensors that detect the binding of proteins onto the sensor surface via the change this induces in the refractive index. Since the characterizing resonance peaks of the photonic crystal cavities depend on the refractive index, this detection will be done by comparing resonance spectra. The major part of this project is the optimalization of the design of the photonic crystal membrane nanocavities to do this detection, i.e. what are the parameters that determine the sensor performance. These questions

need to be answered before looking at protein detection. What lies beyond the scope of this master project is the microfluidic integration of photonic crystal membrane nanocavities, the development of immunoassays and the design of a full lab-on-a-chip based on arrays of functionalized photonic crystal membrane nanocavities.

As was stated in paragraph 1.2, photonic crystal membrane nanocavities are a good candidate to be the next generation biosensors. Our research is new in the sense that until now, photonic crystal membrane nanocavities have been made mostly in silicon-based systems that can be easily incorporated in the current silicon platform. However, these devices need an external light source and access waveguides to make the cavities resonate. The next generation integrated photonic circuits will have sources and detectors built-in on the chip which allows researchers to look into photonic crystal nanocavities based on active III/V semiconductors. This offers the possibility for remote optical read-out by photoluminescence. A few groups have reported on the fabrication of III/V based photonic crystal membrane nanocavities with incorporated quantum wells but we report here on the first sensor with quantum dot embedded photonic crystal membrane nanocavities.

This report will start with a theoretical background of two-dimensional photonic crystal membranes in Chapter 2. In the next chapter the fabrication, characterization and desing of the cavities will be discussed. Chapter 4 starts with a theoretical description of the binding of proteins to a surface after which results will be shown for InP substrates. In Chapters 5 and 6 the results for bulk refractive index sensing and protein detection are described after which the conclusions are summarized.

Chapter 2

Theory

This chapter will start with the master equation which will be necessary to describe the propagation of light in waveguides, 2D photonic crystals (PhC), and PhC membranes. For a more thorough explanation of the theory behind photonic crystals is referred to [17, 25]. Attention is also given to cavities which are created by introducing defects into the PhC.

2.1 Derivation of the master equation

First of all, a theoretical framework is needed for the propagation of electromagnetic waves in a photonic crystal, a structure that consists of periodically arranged regions of different dielectric materials as was shown in Figure 1.4. The field of electromagnetism is governed by four fundamental equations, called the Maxwell equations. In SI units these four equations are given by

$$\nabla \cdot \mathbf{B} = 0 \tag{2.1}$$

$$\nabla \cdot \mathbf{D} = \rho \tag{2.2}$$

$$\nabla \times \mathbf{E} + \frac{\partial \mathbf{B}}{\partial t} = 0 \tag{2.3}$$

$$\nabla \times \mathbf{H} - \frac{\partial \mathbf{D}}{\partial t} = \mathbf{J} \tag{2.4}$$

In these equations, $\mathbf{E}$ and $\mathbf{H}$ are the electric and magnetic field, $\mathbf{D}$ and $\mathbf{B}$ the electric and magnetic flux density, ρ the free charge, $\mathbf{J}$ the current density and t the time.

Assuming that the field strengths of $\mathbf{E}$ and $\mathbf{H}$ are small and that the dielectric material is macroscopic, isotropic, transparent and that material dispersions can be ignored, means that $\mathbf{E}$ and $\mathbf{H}$ depend linearly on $\mathbf{D}$ and $\mathbf{B}$ and that $\mathbf{E}$ and $\mathbf{D}$ are related by ε_0 times the dielectric function $\varepsilon(\mathbf{r})$ which is real and positive.

With these assumptions $\mathbf{D}$ and $\mathbf{B}$ are related to $\mathbf{E}$ and $\mathbf{H}$ by

$$\mathbf{D}(\mathbf{r}) = \varepsilon_0 \varepsilon(\mathbf{r}) \mathbf{E}(\mathbf{r}) \tag{2.5}$$

$$\mathbf{B}(\mathbf{r}) = \mu_0 \mu(\mathbf{r}) \mathbf{H}(\mathbf{r}) \tag{2.6}$$

Equation 2.6 can be further simplified to $\mathbf{B} = \mu_0 \mathbf{H}$ because for most dielectrics the relative magnetic permeability $\mu(\mathbf{r})$ is very close to unity.

Assume there are no current ($\mathbf{J} = 0$) or free charges ($\rho = 0$), and using equations 2.5 and 2.6 the Maxwell equations can be written as

$$\nabla \cdot \mathbf{H}(\mathbf{r}, t) = 0 \tag{2.7}$$

$$\nabla \cdot [\varepsilon(\mathbf{r}) \mathbf{E}(\mathbf{r}, t)] = 0 \tag{2.8}$$

$$\nabla \times \mathbf{E}(\mathbf{r}, t) + \mu_0 \frac{\partial \mathbf{H}(\mathbf{r}, t)}{\partial t} = 0 \tag{2.9}$$

$$\nabla \times \mathbf{H}(\mathbf{r}, t) - \varepsilon_0 \varepsilon(\mathbf{r}) \frac{\partial \mathbf{E}(\mathbf{r}, t)}{\partial t} = 0 \tag{2.10}$$

Since these equations are all linear relations, the time and space dependency of both the electric and magnetic field can be separated by writing them as harmonic modes

$$\mathbf{E}(\mathbf{r}, t) = \mathbf{E}(\mathbf{r}) e^{-i\omega t} \tag{2.11}$$

$$\mathbf{H}(\mathbf{r}, t) = \mathbf{H}(\mathbf{r}) e^{-i\omega t} \tag{2.12}$$

Inserting these into equations 2.7 - 2.10 we find

$$\nabla \cdot \mathbf{H}(\mathbf{r}) = 0 \tag{2.13}$$

$$\nabla \cdot [\varepsilon(\mathbf{r}) \mathbf{E}(\mathbf{r})] = 0 \tag{2.14}$$

$$\nabla \times \mathbf{E}(\mathbf{r}) - i\omega \mu_0 \mathbf{H}(\mathbf{r}) = 0 \tag{2.15}$$

$$\nabla \times \mathbf{H}(\mathbf{r}) + i\omega \varepsilon_0 \varepsilon(\mathbf{r}) \mathbf{E}(\mathbf{r}) = 0 \tag{2.16}$$

Equations 2.13 and 2.14 require that both the electric and magnetic field are composed of transverse electromagnetic waves and equations 2.15 and 2.16 can be rewritten into one equation, called the master equation.

$$\nabla \times \left(\frac{1}{\varepsilon(\mathbf{r})} \nabla \times \mathbf{H}(\mathbf{r}) \right) = \left(\frac{\omega}{c} \right)^2 \mathbf{H}(\mathbf{r}) \tag{2.17}$$

Because for photonic crystals, the permittivity $\varepsilon(\mathbf{r})$ is a periodic function, the master equation has been reduced to a periodic eigenvalue problem. This means that the solutions can be obtained using Bloch's theorem

$$\mathbf{H}(\mathbf{r}) = \mathbf{H}_{n,\mathbf{k}}(\mathbf{r}) \cdot e^{i\mathbf{k}\cdot\mathbf{r}} \tag{2.18}$$

where n is the mode number and $\mathbf{k}$ the wave vector. Equation 2.18 has eigenvalues that satisfy

$$(\nabla + i\mathbf{k}) \times \left[\frac{1}{\varepsilon(\mathbf{r})} (\nabla + i\mathbf{k}) \times \mathbf{H}_{n,\mathbf{k}}(\mathbf{r}) \right] = \left(\frac{\omega_n(\mathbf{k})}{c} \right)^2 \mathbf{H}_{n,\mathbf{k}}(\mathbf{r}) \tag{2.19}$$

Most of the paragraphs in this chapter will be based on equation 2.18.

The master equation only gives solutions for the magnetic field $\mathbf{H}(\mathbf{r})$ but when this equation is solved and the frequencies of the modes are determined, equation 2.16 can be used to determine $\mathbf{E}(\mathbf{r})$.

2.2 The propagation of light in waveguides

2.2.1 Planar waveguides

Consider an infinite plane of dielectric material surrounded by air. This is called a planar waveguide and as can be seen from Figure 2.1, this structure has a constant dielectric function in the x and y direction but $\varepsilon(\mathbf{r})$ changes in the z direction when going from the dielectric material to air. This means that the system is invariant under all translational operators in the xy plane and that the modes are given by

$$\mathbf{H}_{\mathbf{k}_\parallel}(\mathbf{r}) = \mathbf{h}(z) e^{i\mathbf{k}_\parallel \cdot \boldsymbol{\rho}} \tag{2.20}$$

where $\mathbf{k}_\parallel = \mathbf{k}_x + \mathbf{k}_y$ and $\boldsymbol{\rho}$ is the projection of $\mathbf{r}$ in the xy plane.

Figure 2.1: *A planar waveguide.*

An important property of the planar waveguide is its ability to reflect light without any losses if the angle θ of the incoming light with respect to the plane is small enough. The refraction of light at the interface between two dielectrics is described by Snell's law, $n_1 \sin\theta_1 = n_2 \sin\theta_2$ and a schematic representation is given in Figure 2.2. For a planar dielectric waveguide surrounded by another dielectric, n_1 is the refractive index of the waveguide and n_2 of the surrounding dielectric and θ_1 and θ_2 are the angles the ray makes with the normal to the interface. If the incoming angle θ_1 is large enough so that $\theta_1 > \sin^{-1}(n_2/n_1)$, then Snell's law states that $\sin\theta_2$ should be larger than 1 but there is no angle θ_2 for which this is possible. With other words, transmission of light from the waveguide to the surrounding dielectric is not allowed and the light is totally reflected. This argumentation is only valid

when $n_1 > n_2$ so total internal reflection only occurs within the dielectric with the highest refractive index.

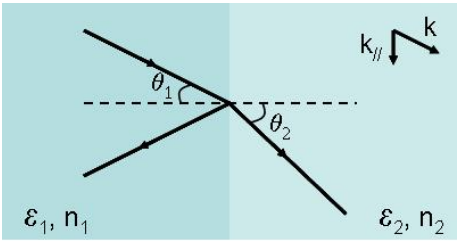

Figure 2.2: *The refraction of light at the interface of a waveguide* (n_1) *and the surrounding dielectric material* (n_2).

For the planar waveguide of Figure 2.1, only certain angles larger than the critical angle give rise to propagating modes. The relation between the mode frequencies ω and the wave vector $\mathbf{k}$ is called the dispersion relation. The dispersion relation (or band structure or band diagram) of a planar waveguide surrounded by air is shown in Figure 2.3 (a).

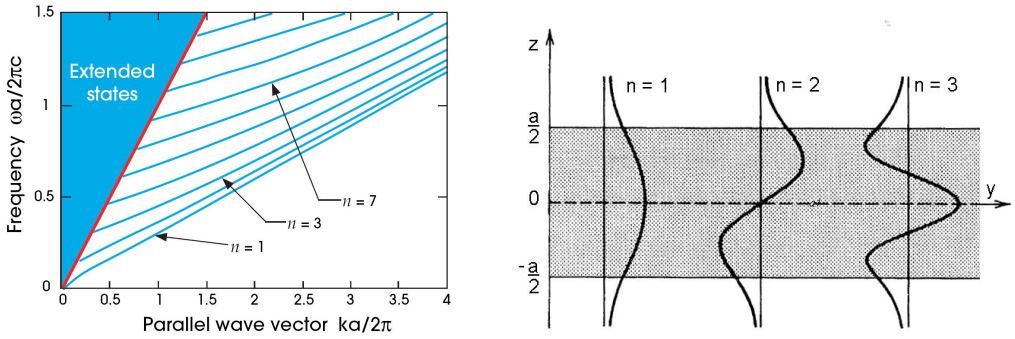

(a) (b)

Figure 2.3: *(a) The dispersion relation* $\omega_n(k_\parallel)$ *of a planar waveguide with thickness* a *and dielectric constant* ε*=11.4. The blue region is the light cone, the red line indicates the light line and the propagating modes are indicated by the blue lines [17], (b) The field distributions for the TE guided modes in a dielectric waveguide with thickness a [26].*

The modes that do not undergo total internal reflection are transmitted at the interface and they propagate into the air, or more generally the cladding dielectric, after being refracted. The boundary between modes that are localized in the dielectric and modes that refract into the surrounding air is called the light line which is given by $\omega = ck_\parallel/n_2$. At a large distance from the dielectric, the extended states must behave like regular plane waves characterized by

$$\omega = \frac{c|\mathbf{k}|}{n_2} = \frac{c}{n_2}\sqrt{k_\parallel^2 + k_\perp^2} \tag{2.21}$$

Because there is no limitation on the values for $k_\perp$, only that they need to be real, there will be modes with every possible frequency greater than $ck_\parallel$. This means there is a continuous spectrum of states above the light line. This area is the blue region in Figure 2.3 (a) which is called the light cone. The modes guided by the dielectric waveguide lay underneath the light cone because ε is larger which lowers the frequency. These solutions decay exponentially away from the dielectric which means that they need to have an imaginary $k_\perp$. For a fixed $k_\parallel$ the solutions form a discrete set of $\omega_n(k_\parallel)$ and they are labeled by the mode number n, starting with $n = 1$ for the lowest frequency. As Figure 2.3 (a) shows, there always is at least one mode since the mode $n = 1$ is always allowed.

The mode $n = 1$ is referred to as the first order mode or the fundamental mode, and all $n > 1$ are higher order modes. The field distributions of the first few modes are shown in Figure 2.3 (b). The condition to avoid higher order modes and work with a single mode waveguide is given by

$$\frac{2a}{\lambda} NA < 1 \tag{2.22}$$

with λ the wavelength in free space and NA the numerical aperture given by $\sqrt{n_1^2 - n_2^2}$ [26].

2.2.2 Periodicity leads to a photonic band gap

The Brillouin zone

When the waveguide is no longer the simple planar waveguide of Figure 2.1 but a waveguide with translational symmetry in the y direction, equation 2.18 can be rewritten and a primitive lattice vector and primitive reciprocal lattice vector can be defined.

For a system with discrete translational symmetry, the modes that can propagate are given by a Bloch state

$$\mathbf{H}_\mathbf{k}(\mathbf{r}) = \mathbf{u}_\mathbf{k}(\mathbf{r}) e^{i\mathbf{k}\cdot\mathbf{r}} \tag{2.23}$$

where $\mathbf{u}_\mathbf{k}(\mathbf{r})$ is a periodic function with $\mathbf{u}_\mathbf{k}(\mathbf{r}) = \mathbf{u}_\mathbf{k}(\mathbf{r} + \mathbf{R})$, where $\mathbf{R}$ is a real space lattice vector.

For a one-dimensional situation with a the lattice constant, the primitive lattice vector is given by $\mathbf{a} = a\hat{\mathrm{y}}$, and for $b = \frac{2\pi}{a}$ the primitive reciprocal lattice vector is defined by $\mathbf{b} = b\hat{\mathrm{y}}$. With these definitions the Fourier transformation of equation 2.23 in one dimension becomes

$$\mathbf{H}_\mathbf{k}(y) = \sum_m \mathbf{u}_{\mathbf{k},m}(y) e^{imby} e^{iky} \tag{2.24}$$

This introduces a periodicity in reciprocal lattice vector, implying that the Bloch states with wave vector k_y and with wave vector $k_y + mb$ are identical if m is an integer [27]. This implies that the mode frequencies are periodic in k_y so $\omega(k_y) = \omega(k_y + mb)$ so all allowed ω can be found with $k_y's$ within the range $\frac{-\pi}{a} < k_y \leq \frac{\pi}{a}$. This range is called the Brillouin zone. When the dielectric structure has a certain symmetry operation, the $\omega_n(\mathbf{k})$ function has that symmetry too. These operations (rotation, mirror-reflection and inversion symmetry) are therefore called the point group of the structure. As a consequence, one does not need to consider the $\omega_n(\mathbf{k})$ of the entire Brillouin zone. The smallest region within the Brillouin zone for which the $\omega_n(\mathbf{k})$ are not related by symmetry operators is called the irreducible Brillouin zone.

The photonic band gap

To understand the origin of the photonic band gap, one-dimensional photonic crystals in which several dielectric layers (multilayer structure) with period a are stacked onto each other in the z direction will be explored. This structure is periodic in the z direction and homogenous in the xy plane which allows one to write equation 2.23 as

$$\mathbf{H}_{n,k_z,\mathbf{k}_\parallel}(\mathbf{r}) = \mathbf{u}_{n,k_z,\mathbf{k}_\parallel}(z)e^{i\mathbf{k}_\parallel\cdot\boldsymbol{\rho}}e^{ik_z z} \tag{2.25}$$

with $\boldsymbol{\rho}$ the projection of $\mathbf{r}$ in the xy plane and $\mathbf{u}(z) = \mathbf{u}(z + R)$ with R an integer multiple of a. Because the 1D photonic crystal has continuous translational symmetry in the xy plane, the wave vector $\mathbf{k}_\parallel$ can assume any value but the wave vector k_z is restricted to the Brillouin zone $\frac{-\pi}{a} < k_z \leq \frac{\pi}{a}$ because of its discrete translational symmetry.

Looking only at waves that propagate in the z-direction ($\mathbf{k}_\parallel = 0$) and setting $k = k_z$, the dispersion relations $\omega_n(k)$ can be plotted. Figure 2.4 shows the dispersion relations of three different dielectric multilayer systems. Each layer has a thickness $0.5a$ and the dielectric constants vary between two consecutive layers. Figure 2.4 (a) shows the band diagram of homogeneous GaAs bulk material with $\varepsilon = 13$. The modes of this system all lie along a line given by $\omega(k) = \frac{ck}{\sqrt{\varepsilon}}$. Because the graphs are restricted to the Brillouin zone, the dispersion relation is folded back into the range $\frac{-\pi}{a} < k_z \leq \frac{\pi}{a}$ for values $k > \frac{\pi}{a}$ and $k < \frac{-\pi}{a}$.

Figures 2.4 (b) and (c) show the dispersion relations of a multilayer system with GaAs and GaAlAs and a multilayer system with GaAs and air, respectively. Because of the small, respectively large difference in ε between the different layers, a gap is created between the $n = 1$ and $n = 2$ branches of the band diagram. This means that for these specific frequencies, there is no allowed mode in the Brillouin zone and therefore this ω-region is referred to

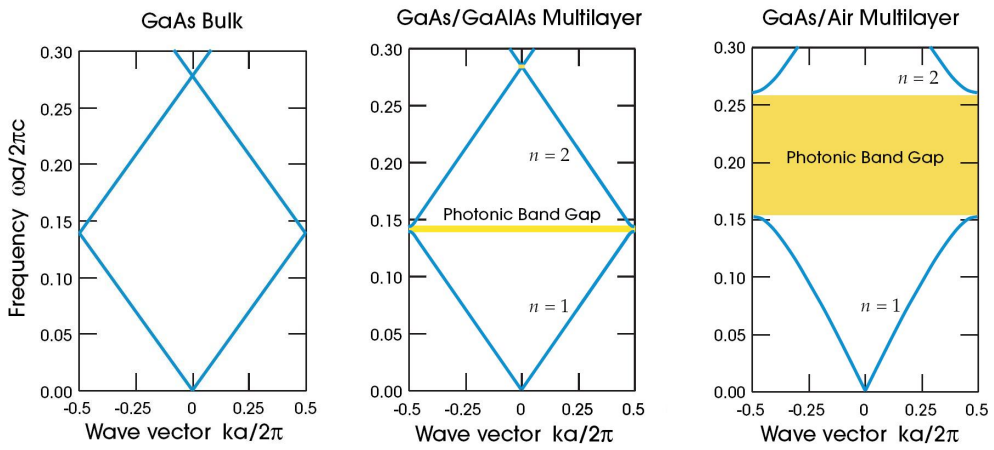

(a) (b) (c)

Figure 2.4: *The dispersion relations for three different multilayer systems for propagation in the z-direction, (a) $\varepsilon = 13$ for each layer, (b) ε alternates between 12 and 13, (c) ε alternates between 1 and 13 [17].*

as the photonic band gap.

The photonic band gap occurs at $k = \frac{\pi}{a}$ which is at the edge of the Brillouin zone, and corresponds to the Bragg reflection condition. Here the modes have a wavelength $2a$ so their nodes are located either in the low-ε or high-ε dielectric. Because low frequency modes center their energy in the high-ε layer and high frequency modes have more energy in the low-ε layer, the origin of the band gap and the difference between Figure 2.4 (b) and (c) can be understood. The mode below the band gap has more of its energy in the high-ε GaAs and the mode above the band gap has more of its energy in the lower-ε GaAlAs or air. Because the low-ε region is usually air, the convention is to refer to the band above the photonic band gap as the air band and to the band below the band gap as the dielectric band.

2.2.3 A periodic waveguide

To see the difference in band diagrams between a planar and a periodic waveguide one needs to go back to the planar waveguide. As shown in Figure 2.5 (a), the dielectric strip with $\varepsilon = 12$ extends in the x- and y-direction and it is known from paragraph 2.2.1 that the light is confined in the z-direction by total internal reflection. A periodic waveguide is created by introducing a periodic discontinuity in the strip in the y-direction as is shown in the inset of Figure 2.5 (b). Two restrictions are made; only light propagating in the in the xy-plane ($k_z = 0$) and with TM-polarization is taken into account. Both waveguides have translational symmetry in the y-direction but not in the z-direction, therefore k_y is conserved but k_z is not so $k = k_y$.

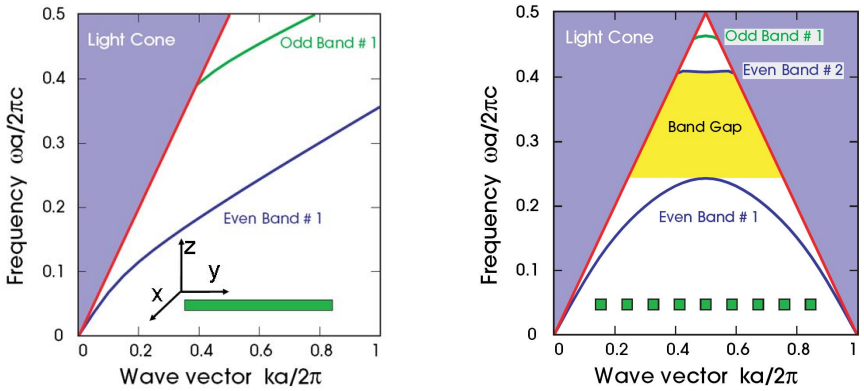

Figure 2.5: *Band diagrams for a planar (a) continuous and (b) periodic waveguide for the in-plane propagation light [17].*

For the planar waveguide of Figure 2.5 (a), the light cone ($\omega \geq ck/n$ with $n = n_{environment}$) encloses the extended states propagating in air as was explained in paragraph 2.2.1. Beneath the light cone ($\omega < ck/n$) the higher index of the dielectric waveguide pulls down modes that are guided by the waveguide. This property was previously described as total internal reflection but can in a more general way be referred to as index guiding. Because the waveguide is symmetric under reflections through the $z = 0$ plane, the guided modes are either even or odd with respect to $z = 0$.

The periodically discontinuous waveguide of Figure 2.5 (b) has a period a and each square of dielectric material has a size $0.4a \times 0.4a$. Light rays can not stay inside the dielectric squares so it seems impossible that the light in this waveguide is guided by total internal reflection. However, Bloch formulated a theorem that says that waves in a periodic structure can propagate without scattering. The periodic structure has Bloch modes as solutions with frequencies below the light cone. So because of the periodicity of the system, the wave vector $k = k_y$ is still conserved so there still is a light cone beneath which localized modes can exist as can be seen from Figure 2.5 (b).

An important difference between the planar and periodic waveguide are the values of k. For the planar continuous waveguide the wave vector is not restricted because of the continuous translational symmetry, but for the periodic waveguide the wave vector can be restricted to the Brillouin zone: $-\frac{\pi}{a} < k \leq \frac{\pi}{a}$. Because of the periodicity, the dispersion relation in the range $\frac{\pi}{a} < k < \frac{2\pi}{a}$ is identical to the dispersion relation the range $\frac{-\pi}{a} < k < 0$ which is the reverse of the dispersion relation in the range $0 < k < \frac{\pi}{a}$ (see paragraph 2.2.2). Because of this reversibility there also is a light cone in

the range $0 < k < \frac{\pi}{a}$. Analogously, the lowest band starts at $(k = 0, \omega = 0)$ and it reaches its maximum at $k = \frac{\pi}{a}$ after which it goes back to $\omega = 0$ at $k = \frac{2\pi}{a}$. Because this band is pulled down, a photonic band gap arises between the first two guided modes, just as in the multilayer systems of Figure 2.4 (b) and (c). The difference between the multilayer systems and the periodic waveguide is that the band gap only exists for the guided modes. The modes within the light cone can still exist for every ω. The photonic band gap of Figure 2.5 (b) is therefore called incomplete whereas the ones from Figure 2.4 are complete photonic band gaps.

2.3 Two-dimensional photonic crystals

The second step on the way to two-dimensional photonic crystal membranes are two-dimensional photonic crystals that are periodic in the x- and y-direction while homogenous and infinitely long in the z direction as was shown in Figure 1.4 (b). Consequently, $\varepsilon(\mathbf{r}) = \varepsilon(\mathbf{r} + \mathbf{R})$, k_z is not restricted and $\mathbf{k}_\parallel$ can be restricted to the Brillouin zone. Propagation is assumed to always be in-plane or $k_z = 0$. The Bloch states can now be written as

$$\mathbf{H}_{n,k_z,\mathbf{k}_\parallel}(\mathbf{r}) = \mathbf{u}_{n,k_z,\mathbf{k}_\parallel}(\rho) e^{i\mathbf{k}_\parallel \cdot \boldsymbol{\rho}} e^{ik_z z} \tag{2.26}$$

with $\boldsymbol{\rho}$ the projection of $\mathbf{r}$ in the xy-plane and $\mathbf{u}(\boldsymbol{\rho}) = \mathbf{u}(\boldsymbol{\rho} + \mathbf{R})$.

The modes that are allowed to propagate in the photonic crystal can be distinguished by their polarization. Transverse-electric (TE) modes have $\mathbf{E}$ in the xy-plane and $\mathbf{H}$ normal to the plane and transverse-magnetic (TM) modes have $\mathbf{E}$ normal to the plane and $\mathbf{H}$ in the plane. In the next paragraph, two different 2D photonic crystal structures are described and the importance of the polarization will become clear.

2.3.1 Dielectric columns and veins

Figure 2.6 (a) shows the TE and TM dispersion relations for light that propagates in the xy-plane of a square array of dielectric columns with radius $0.2a$, lattice constant a and $\varepsilon = 8.9$. The wave vector $\mathbf{k} = \mathbf{k}_\parallel$ is only plotted along the edges of the irreducible Brillouin zone. Because the points $\mathbf{k} = (0, 0)$, $\mathbf{k} = (\frac{\pi}{a}, 0)$ and $\mathbf{k} = (\frac{\pi}{a}, \frac{\pi}{a})$ are referred to as the Γ, X and M point respectively, the edges of the irreducible Brillouin zone are determined by ΓX, XM and $M\Gamma$. The dispersion relations can be restricted to these directions because the minimum and maximum of the dispersion lines, i.e. the points that determine the band gap, almost always occur at the edges of the Brillouin zone and often at a corner. This is also the case for the structures discussed in this chapter [17].

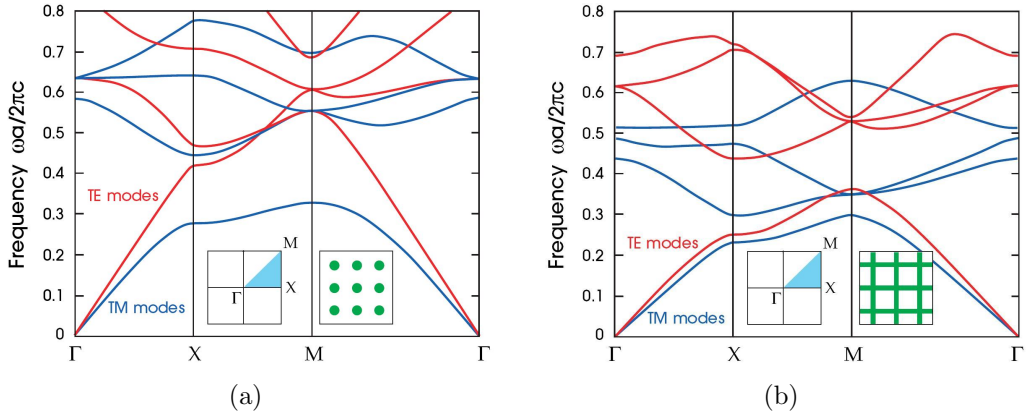

Figure 2.6: *The band diagram of (a) a square array of columns and (b) a square lattice of veins. The insets show the structures and their Brillouin zones with the irreducible Brillouin zones highlighted in blue [17].*

Figure 2.6 (a) shows that this structure of columns has a complete band gap for the TM modes between the first and second band. However, for the TE modes there is no band gap. Looking at the band diagram of a different 2D structure, a square grid of dielectric veins with thickness $0.165a$ and $\varepsilon = 8.9$ in Figure 2.6 (b), it is seen that there is no band gap for the TM modes and only a small one for the TE modes.

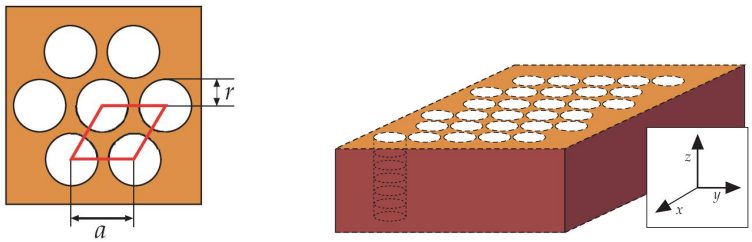

Figure 2.7: *Hexagonal structure of air holes (a) top view, (b) side view [17].*

The column and vein structures can be combined into the hexagonal array of air holes shown in Figure 2.7. This structure combines isolated high-ε regions that resemble the dielectric columns with a connected grid that resembles the veins. Figure 2.6 (a) showed that a isolated high-ε regions lead to a large TM photonic band gap. On the contrary, there was no TM photonic band gap for the square grid of dielectric veins; the connectivity of the veins led to a TE photonic band gap. In the square array of dielectric columns, the TE modes had to penetrate the low-ε regions resulting in no TE band gap. The square grid of dielectric veins does not have this problem because the mode can follow the high-ε veins, giving rise to a small TE band gap. Since the hexagonal array of air holes combines these features, it has a photonic band gap for both TE and TM modes as can be seen from

Figure 2.8. The complete photonic band gap, i.e. a band gap for the TE modes as well as the TM modes, only occurs for large $\frac{r}{a}$ values ($> 0.4a$). In practice much smaller value are used ($\sim 0.3a$) so there will only be a TE gap.

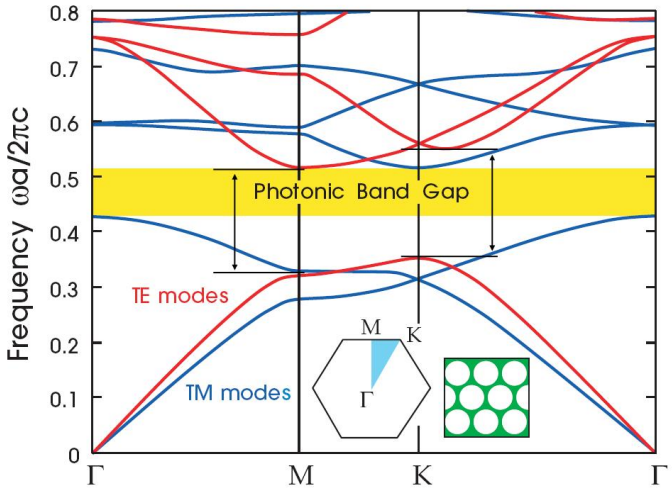

Figure 2.8: *The band diagram for the hexagonal structure of air holes with* $\varepsilon = 13$ *and* $\frac{r}{a} = 0.48$*. The blue lines represent TM band and the red lines TE bands. The inset also shows the irreducible Brillouin zone, shaded in light blue [17]. The stop gaps are indicated by the black arrows.*

2.3.2 Point and linear defects

For 2D photonic crystals with band gaps for the in-plane propagation of light, no modes are allowed with frequencies within the band gap. However, by slightly changing one (or a few) lattice site(s), a single localized mode (or a few modes) can be created with a frequency within the band gap because locally the periodicity is broken. For the hexagonal structure of air holes, one of the air holes can be removed or have an increased/decreased radius. Key is that the dielectric constant is changed compared to the original structure. The perturbation that is applied to the photonic crystal is localized to a certain point in the xy-plane which is why it is called a point defect. This defect is introduced to obtain a localized mode inside the band gap, implying that the mode needs to be evanescent because it can not propagate in the crystal. By changing one lattice site, a cavity is created with reflecting walls in the xy-plane because the photonic crystal reflects light with frequencies inside its band gap. If the cavity can support a single mode in the band gap, that light can not leave the cavity and the mode is related to the defect.

By means of point defects light can be localized, and by using linear defects light can be guided from one location to the other. This can be done by removing for example one line of air holes from the hexagonal structure of

air holes. Light that propagates along this line with a frequency within the band gap of the surrounding photonic crystal is guided along this linear defect.

2.4 Photonic crystal membranes

2.4.1 The dispersion relation of a photonic crystal membrane

With the background of the previous paragraphs, two dimensional photonic crystals with a finite thickness, also know as photonic crystal membranes can be understood. The finite thickness in the vertical z-direction introduces a different $\omega_n(\mathbf{k})$ behavior, shown in Figure 2.9. Like with the 2D photonic crystal, a hexagonal lattice of air holes with radius $r = 0.3a$ will be considered but now with a finite thickness of $0.6a$, as is shown in the inset of Figure 2.9. The membrane is surrounded by air which is why this structure is referred to as a suspended membrane. The structure has a discrete translational symmetry in the x- and y-direction so the in-plane wave vector $\mathbf{k}_{\|}$ is conserved, but the vertical wave vector k_z is not conserved. As in paragraph 2.2.1, the extended modes that propagate in air lay within the light cone for $\omega \geq c \mid \mathbf{k}_{\|} \mid$ and below the light line, the higher refractive index of the membrane has pulled down discrete guided bands. This structure has a TE-like band gap but it is not a complete band gap; only the guided modes have a band gap, the ones above the light cone do not.

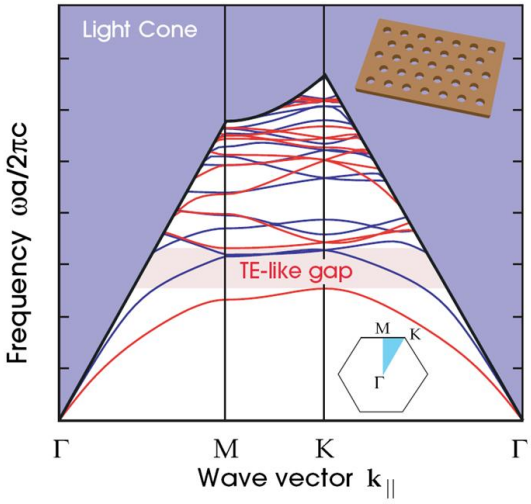

Figure 2.9: *The band diagram of a photonic crystal membrane. The shaded purple area is the light cone and below it are the guided modes localized to the membrane. Blue lines represent TM modes and red lines TE modes [17].*

2.4.2 Defects

Just as for a 2D photonic crystal, creating a point defect can result in a localized mode. Because a localized mode has no discrete k-value, but a distribution of k-values which may extend to values within the light cone, the localized mode(s) are leaky resonances, with intrinsic vertical radiation losses. The design challenge is to minimize the k-components within the light-cone. Examples of different point defects can be found in the next chapter.

By filling one line of air holes with dielectric material, the average dielectric constant of the photonic crystal membrane structure is increased which pulls bands down from the upper edge of the band gap as is shown in Figure 2.10. This structure is referred to as a W1 defect; 1 is used since one line of holes was removed and W stand for waveguide. In paragraph 2.3.2 it was explained why this structure guides light.

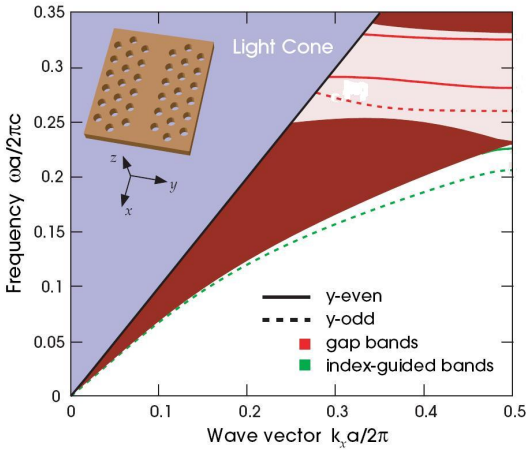

Figure 2.10: *The band diagram a photonic crystal membrane with W1 defect. Dark-red shaded regions indicate extended TE-like modes of the crystal. Guided modes are introduced both in the band gap (red lines) and below all the extended modes of the crystal (green lines) [17].*

In recent years, a new type of structure has been used that is able to guide and enhance light in low-index regions [28–34]. The structure is referred to as a slotted waveguide and an example is shown in Figure 2.11. The slotted waveguide is interesting for this project because the slot allows for a better interaction between matter (the sample analyte) and light. For the theoretical background of slotted waveguides is referred to [28] but an intuitive approach is given here. The structure of Figure 2.11 can confine and guide light when it is polarized with its electrical field perpendicular to the slot, i.e. for TE modes. This way the light strongly feels the discontinuity in the refractive index when going from the dielectric material n_W to the air slot n_S. The modes of the two waveguides have their evanescent field inside the

slot and if the slot width w_S is narrow enough, the tail of the two waveguides can overlap. They will then form one mode with a very high intensity and small volume which propagates through the slot (air) and is guided by the waveguide walls.

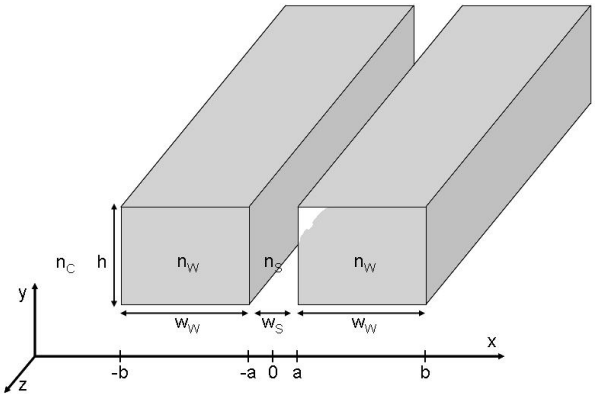

Figure 2.11: *The slotted waveguide. The refractive indices of the cladding, waveguide and slot are referred to as n_C, n_W and n_S, respectively. The waveguides have a height h and width $w_W = b - a$ and the slot has a width $w_S = 2a$ [28].*

2.4.3 The design of a cavity

As stated in paragraph 2.4.2, the challenge in designing a cavity is to reduce the k-components in the light cone because lossy modes are something to avoid. In other words, one wants to maximize the quality factor Q of the cavity mode, defined as the ratio of the power stored inside the cavity and the power lost during one mode period. The quality factor not only depends on the confinement of photons within the plane of propagation, but also on how strongly the photons are confined in the out-of-plane direction by total internal reflection or index guiding. As Figure 2.12 shows, the goal is to create cavity modes for which all angles ensure total internal reflection.

Noda et al. have developed an important design concept to create high-Q cavities to which they refer to as "Gaussian confinement"[36]. It is stated that if one wants to decrease the losses in the vertical direction, one needs to make sure that the envelope of the cavity mode field is a Gaussian function.

This concept can be explained by looking at the straightforward 1D cavity shown in Figure 2.13. This cavity consists of a dielectric material that is finite in the x- and z- direction and it is uniform in the y-direction. In the x-direction the cavity is confined by two perfect mirrors. These mirrors are perfect but the electromagnetic field may penetrate into the mirrors over a finite length.

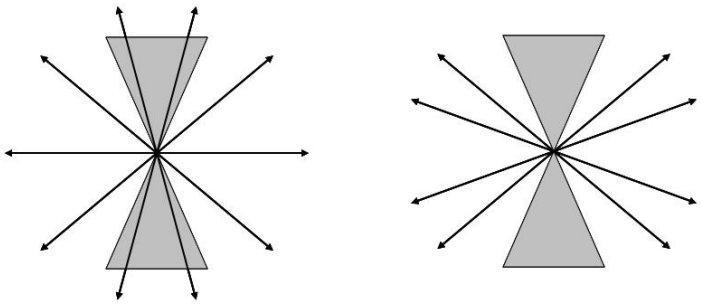

(a) (b)

Figure 2.12: *Components of the resonant mode that lay outside the grey regions will arrive at the dielectric interface at an angle that is large enough to have total internal reflection, (a) a few components of the resonant mode are lossy, (b) all components of the resonant mode are confined by total internal refraction [35].*

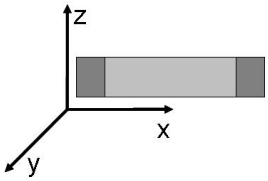

Figure 2.13: *A one-dimensional cavity.*

Two situations of this cavity will be explored in which the in-plane confinement is very different which results in different electric field profiles in the mirror (in the x-direction). With an abrupt mirror, photon confinement is caused by sharp reflections at the cavity walls which results in an electric field profile of the cavity mode with a rectangular envelope function, see Figure 2.14 (a). In the second situation, the photons are confined by a spatially distributed reflection and this causes the cavity mode electric field profile to have a Gaussian envelope function, as is shown in Figure 2.14 (b). The spatial Fourier transform spectra of both electric field profiles gives the plane wave components of the cavity mode and they can be seen in Figures 2.14 (c) and (d). Assuming that the wave vector of light in the surrounding air is k_0, only the plane wave components with $\mid k_{\parallel} \mid > k_0$ can be confined by total internal reflection and the region where $\mid k_{\parallel} \mid < k_0$ is called the leaky region because these are the k-values for which the plane wave components of the cavity mode are leaked into the air. Figures 2.14 (c) and (d) show clearly that the cavity with a rectangular envelope function has more leaky components than the cavity with a Gaussian envelope function.

How are cavities obtained with Gaussian envelope functions instead of rectangular ones? Abrupt changes in the electric-field profile results in rectangular envelope function so one needs to find a way to make the electric-field profiles

at the cavity edges more smooth. This can for example be done by modifying the holes surrounding a cavity. Adjusting the nearest neighbor holes induces a big increase in quality factor which can be further improved by modifying holes further away [37]. Modifying can mean shifting the holes further away from the cavity or reducing their radius.

The physical principle behind this phenomenon is that the Bragg reflection that confines the light in the cavity, depends on the summation of partial reflections at certain points near a cavity. When the holes near the cavity edge are modified, so is the condition for Bragg reflection. Because the phases of partial reflections are changed, a phase-mismatch is obtained that weakens the magnitude of the Bragg reflection. Because the reflection is less, more light penetrates the perfect Bragg mirror were it is reflected perfectly. Because of this, the electric-field profile at the cavity edge will be smoother.

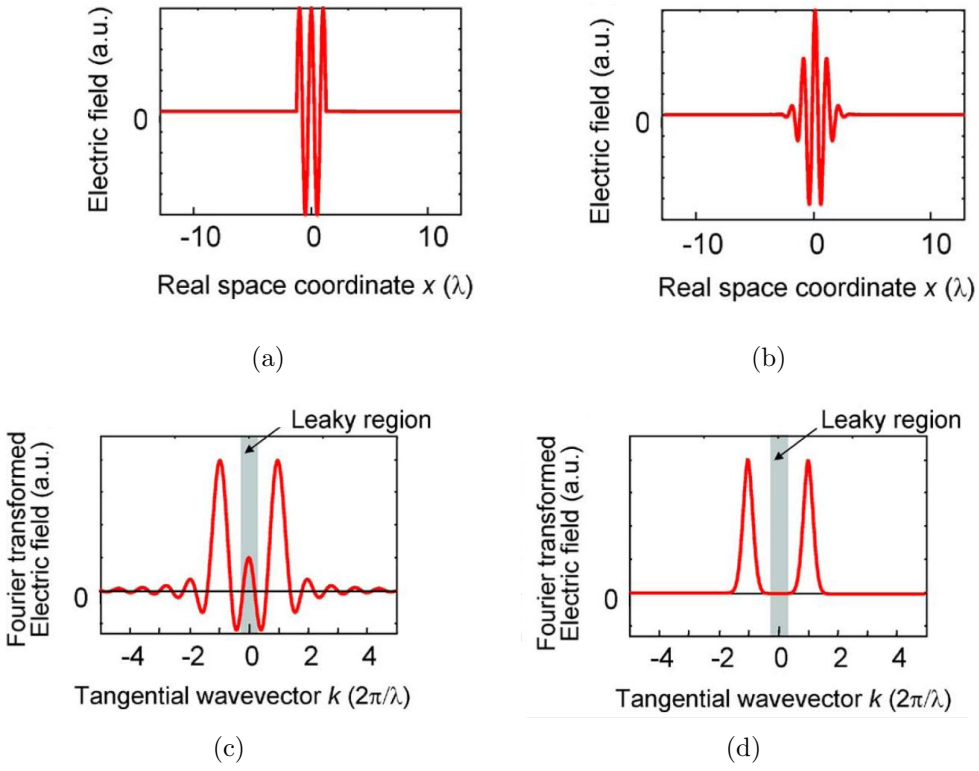

Figure 2.14: *Electrical field profiles of cavities with (a) a rectangular envelope function, (b) a Gaussian envelope function, (c) and (d) the respective Fourier transform spectra of (a) and (b) [36].*

Chapter 3

Photonic crystal membrane nanocavities

This chapter discusses the fabrication, the cavity designs and the characterization of the photonic crystal membrane nanocavities used further in this report. First the production process of photonic crystal membrane nanocavities (see Figure 3.1) will be discussed, starting from a bare InP wafer. The investigated cavity designs are both point defect cavities, of which the band structure was explained in Chapter 2, as well as linear defects in heterostructures. The dispersion characteristics of these heterostructure-like cavities will be explained in this chapter. The resonance spectra of the cavities will be obtained by performing photoluminescence experiments. The working principles as well as the photoluminescence set-up are therefore highlighted.

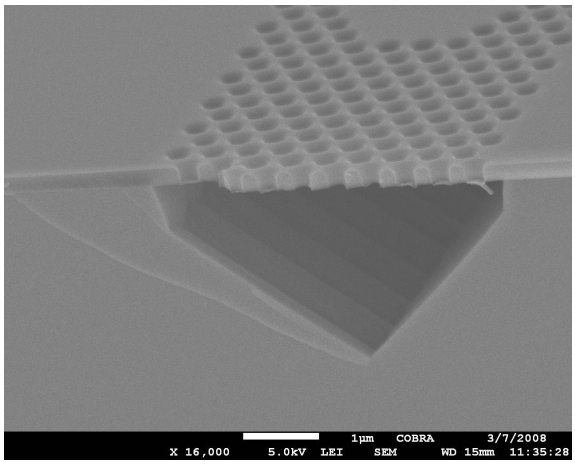

Figure 3.1: *A cross-sectional scanning electron microscope image of a free standing membrane.*

3.1 Typical dimensions

The typical dimensions of a sample, i.e. a piece of wafer on which the photonic crystal membranes are made, is between 0.5 and 1 cm^2. This is just a dimension that is easy to handle, the actual area on which the photonic crystal cavities are written is much smaller. Each photonic crystal (the hexagonal shapes in Figure 3.2) has a lattice constant a of approximately 500 nm and there are about 10 holes surrounding the defect in each direction. This means that each photonic crystal has a surface area of approximately 65 μm^2. Note that because the cavity has reflecting walls, the light is confined to 0.5 - 1 μm^2. The modal volume, i.e. the volume a specific mode occupies, is given by

$$V \equiv \frac{\int \varepsilon(\mathbf{r})|\mathbf{E}(\mathbf{r})|^2 d^3\mathbf{r}}{max[\varepsilon(\mathbf{r})|\mathbf{E}(\mathbf{r})|^2]} \tag{3.1}$$

which is typically given in cubic half-wavelengths $(\lambda/2n)^3$ where n is the refractive index of the slab [17]. For an InGaAsP membrane with $n = 3.37$ and at a wavelength of 1500 nm, the modal volume of a dipole mode is approximately 2.5 cubic half-wavelengths which corresponds to a volume of 0.28 μm^3 [38]. Each sample contains about 200 photonic crystals so the area they occupy on the sample is less than 5 mm^2.

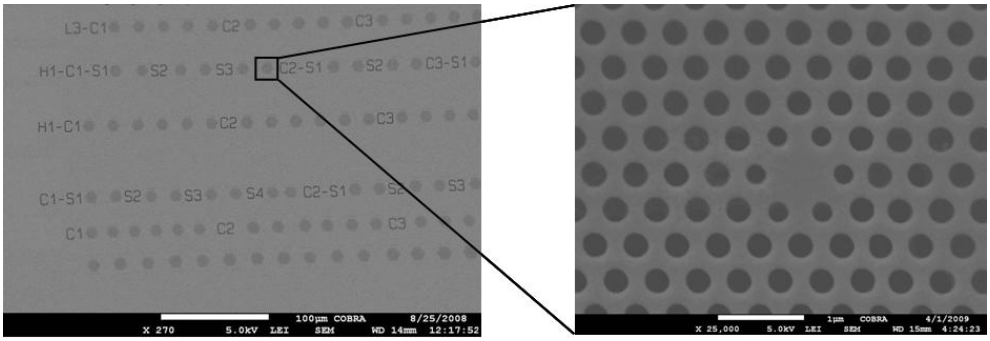

Figure 3.2: *A scanning electron microscope image of part of a sample, and a stronger magnification of one of the cavities.*

3.2 Fabrication process

The fabrication process starts with an InP (100) substrate. On top of this substrate a stack of In(Ga)(As)P layers is grown by metal-organic chemical vapor deposition, see Figure 3.3 (a). First a 1 μm InP buffer layer is grown directly onto the substrate, followed by the active InGaAsP layer. This layer is composed of 110 nm InGaAsP, a quantum dot layer and again 110 nm InGaAsP. ($\lambda = 1.25$ μm). This choice of layer thickness can be explained from equation 2.22. For InGaAsP membranes surrounded by air, the refractive indices are $n_1 = 3.37$ and $n_2 = 1$ and a typical wavelength is 1500 nm. Inserting

these values into equation 2.22, the maximal thickness a of the membrane is found to be ∼233 nm. The InGaAsP material is defined as $Q1.25$ which means that it has a band gap of approximately 1 eV. The quantum dots are created by first growing 1.2 monolayers GaAs on top of the InGaAsP. This interlayer is necessary to obtain InAs quantum dots with wavelengths around 1550 nm when 2 monolayers of InAs are deposited [39, 40]. The density of these InAs quantum dots is about 300 μm^{-2} per layer. To conclude, the active layer is capped with a thin layer (20 nm) of InP.

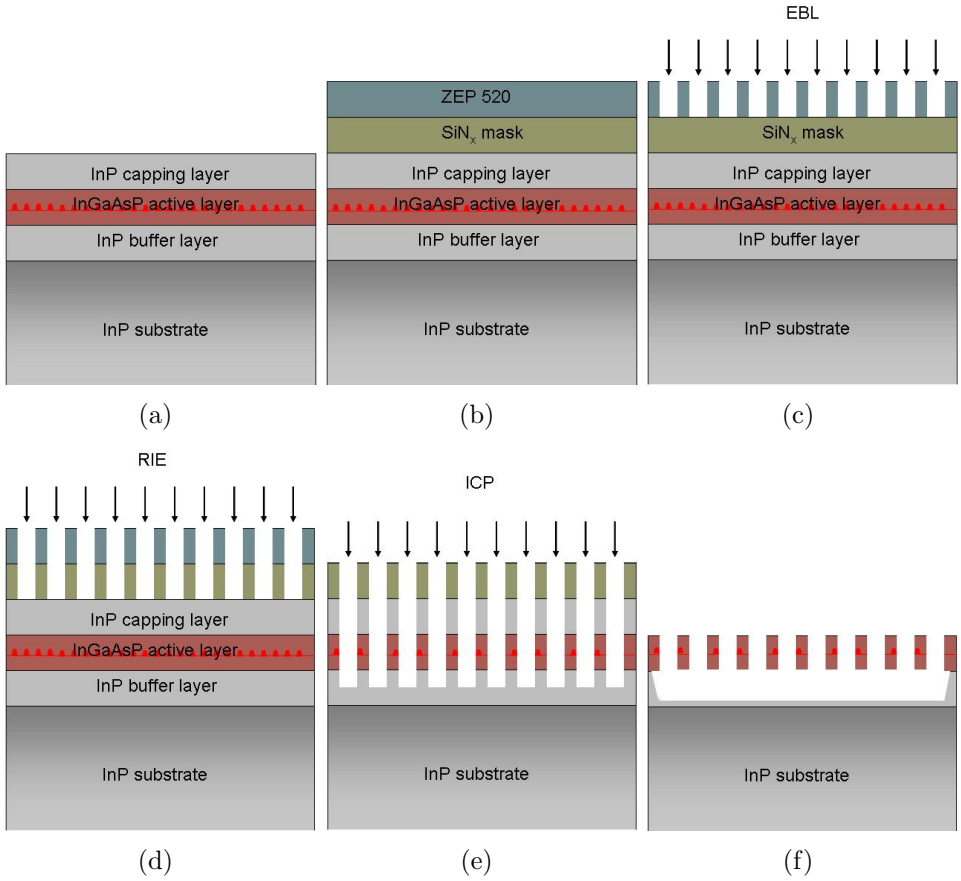

Figure 3.3: *Schematic overview of the fabrication process of photonic crystal membrane cavities (not drawn to scale).*

The PhC pattern can not be directly written into the semiconductor material. Two intermediate stages are necessary to ensure almost-perfect holes, and each of these intermediate steps requires an additional layer. Figure 3.3 (b) shows that these layers are a silicon nitride hard mask and a layer of electron-beam resist called ZEP 520. With plasma enhanced chemical vapor deposition a 400 nm layer of SiN_x is deposited and on top of that, a 350 nm ZEP 520 layer is spin coated.

By means of electron-beam lithography (EBL) at 30 keV, the hexagonal lattice PhC patterns are defined into the ZEP 520 layer as is shown in Fig-

ure 3.3 (c). As Figure 3.2 shows, neighboring photonic crystal cavities are 10 μm apart and the distance between different rows is at least 20 μm. This is done to reduce the interference of electrons used to create one photonic crystal with the photonic crystal next to it and cause an over exposure. Bombarding the resist with electrons lowers its molecular weight and during development, the exposed resist is removed. The pattern is now in the ZEP 520 layer and needs to be transferred into the SiN_x layer. This transfer is done by reactive ion etching (RIE) with CHF_3 after which the ZEP 520 is removed by an oxygen plasma. Next, the pattern is transferred into the InP/InGaAsP/InP layer stack by inductively coupled plasma etching (ICP) using Cl_2, Ar and H_2 (Figure 3.3 (e)). The SiN_x layer can now be removed by a 10% HF solution. The final step is a selective wet chemical etching step using a $HCl:H_2O = 4:1$ solution for 10 minutes at 2°C. This removes the InP cladding layer and undercuts the InGaAsP layer by removing part of the InP buffer layer. What remains is a free standing InGaAsP membrane as can be seen from Figure 3.3 (f). The structure is then given a final rinse with H_2O to remove any remaining acid.

3.3 Characterization of the cavities

3.3.1 Scanning electron microscopy

Scanning electron microscopy (SEM) is a technique in which high-energy electrons are bombarded at the surface which allows one to make an image of the surface. These images are used to see whether the design parameters are indeed the parameters that determine the cavities or whether there is a discrepancy between design and final product.

3.3.2 Photoluminescence

By incorporating quantum dots into the III/V structure, an active material is created. Quantum dots are artificial atoms with discrete energy levels. As a consequence, they can be excited by absorbing a photon and relax again by emitting one. This is a huge advantage compared to passive semiconductor materials like silicon. To characterize silicon photonic crystal cavities, waveguides need to be added and difficult and time-consuming transmission experiments are necessary. This especially is a disadvantage if one wants to do systematic investigations of hundreds of cavities. The experiments performed in this report to obtain the resonance spectra are quite easy and quick: by shining a laser spot onto the membrane, the quantum dots are excited and their emitted light is detected. This process is called photoluminescence (PL). The PL spectrum of an un-patterned surface is shown in Figure 3.4 (a). This is a very broad spectrum which is caused by the size-dispersion of the InAs quantum dots. They are self-assembled and therefore

it is impossible that they all emit light at 1500 nm. By patterning the PhC cavity into the membrane, most wavelengths between 1300 and 1600 nm will become forbidden, because they are in the band gap of the PhC lattice. The PL spectrum will have a few very sharp peaks at the resonance wavelengths of the nanocavities which lay inside the PhC band gap. This is shown in Figure 3.4 (b).

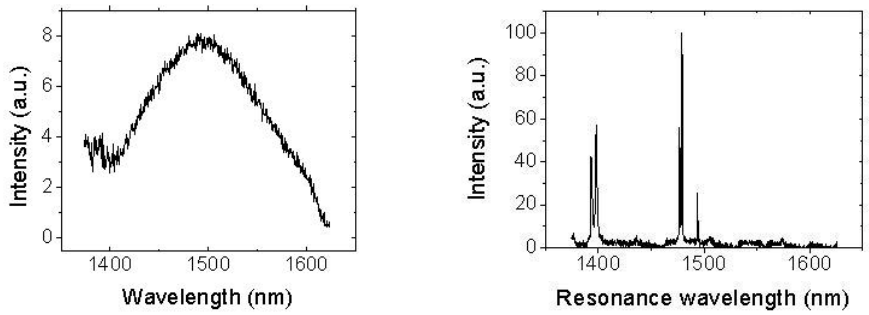

(a) (b)

Figure 3.4: *PL spectra of (a) an un-patterned InGaAsP surface, (b) a modified H1 cavity.*

The use of quantum dots in InP based structures is relatively new [39, 40]. Almost all previous groups working with In(Ga)(As)P membranes use one or more layers of quantum wells [8, 48–51, 71], only one group uses quantum dots in InP membranes [54]. For the experiments in this report the influence of the emitting material due to its absorption is minimal because of the low density of quantum dots. In most other experiments the amount of active material is maximized to compensate for the loss due to absorption, in order to obtain lasing. Under that condition the passive quality factor of the cavity (also known as the "cold "quality factor) is difficult to determine: for low excitation powers the quality factor is too low due to absorption, for high excitation the linewidth is very small due to lasing.

Room temperature micro-photoluminescence experiments are conducted using a continuous wave diode laser with wavelength $\lambda = 660$ nm. This set-up allows the focusing of the laser spot to an area of a few μm^2, which is why it is called micro PL. Low powers (approximately 30 μW) are used to avoid heating of the cavities (that would induce red-shifts of its own) and to avoid destroying the proteins. Figure 3.5 shows the entire PL set-up. The set-up is placed on a shock-absorbent optical table to prevent mechanical noises from interfering with the experiments. The sample is placed on a stage for which the x- and y-position can be controlled on a nanometer scale by means of piezo-positioners. The position in the z-direction (height) can be adjusted by focusing the laser light with the microscope objective. When looking through the microscope (with or without the camera), we see the sample in a way very similar to Figure 3.2.

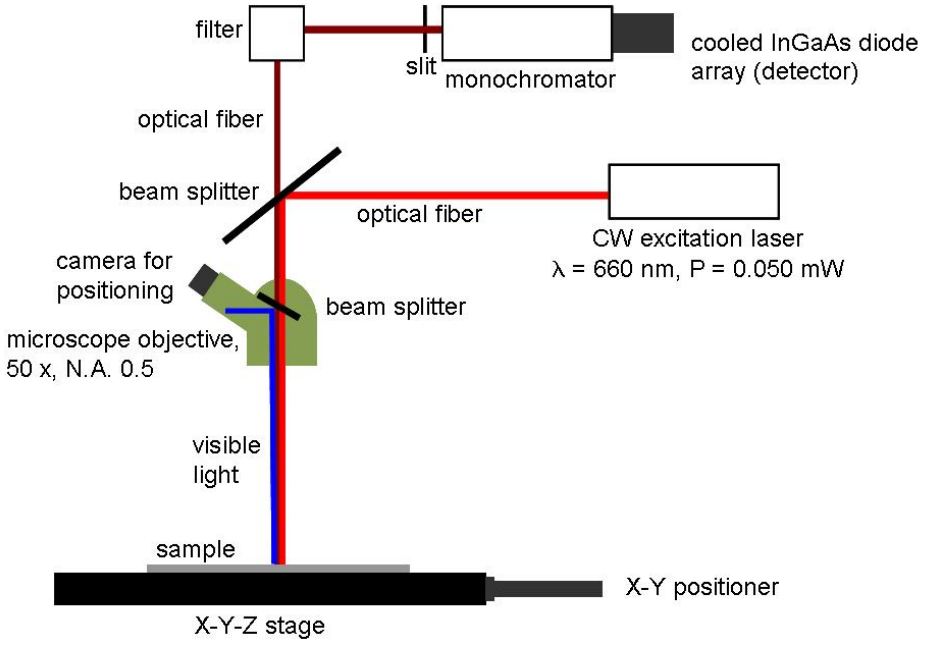

Figure 3.5: *A schematic representation of the photoluminescence set-up.*

During a PL experiment, first, the laser light (in an optical fiber) goes to a beam splitter that reflects about 30% of this light onto the sample. The laser spot is focused onto one of the cavities by an objective with a magnification of 50× and a numerical aperture of 0.5. Because visible light is used to focus the laser spot onto the cavity, a beam splitter is placed inside the microscope objective that reflects the visible light but transmits both all the laser and the emitted light. The light from the laser spot excites the quantum dots and they will emit light with wavelengths dependent on their size; typically the wavelength is between 1300 and 1600 nm. The same objective is used to collect the emitted light and light of these wavelengths is about 80% transmitted by the beam splitter. The beam splitter reflects best at the excitation wavelength (660 nm) and transmits best at the emitting wavelength (∼1500 nm). Afterwards the light is focussed into an optical fiber and it goes through a filter that cuts off any wavelengths below $\lambda =$ 1300 nm. Next the light enters the adjustable slit of the 50 cm monochromator. There the light is dispersed and the entire spectrum is recorded on an InGaAs diode array that is cooled by liquid nitrogen. The InGaAs array has 512 pixels, each 50 μm wide. The spectral resolution of this spectrometer is ∼0.3nm. The signal is sent to a computer where it can be read out with the program WinView (Superlogistics, Inc.). The analysis of the spectra is done with Origin (OriginLab Corporation); by fitting the peaks with a Lorentzian curve the resonance wavelength and the full-width-at-half-maximum of the peaks can be determined [41]. The quality factor defined in paragraph 2.4.3 can then be calculated since $Q = \lambda/\Delta\lambda$.

It should be noted that when the PL spectra of two photonic crystal membrane nanocavities with identical design parameters are compared, the positions of the resonance peaks are not exactly the same. Figure 5.4 shows the PL spectra of two H1$_r$ nanocavities with parameters $a = 530$ nm and $r = 0.22a$. The hexapole mode of sample 1 resonates at 1381.1 nm while for sample 2 this occurs at 1357.2 nm. Analogously, for the quadrupole peaks values are found at 1404.2 and 1410.6 nm for sample 1 and 1387.9 and 1396. nm for sample 2. However, these values are all within a 3% margin so for the sensitivities the effects will be neglected.

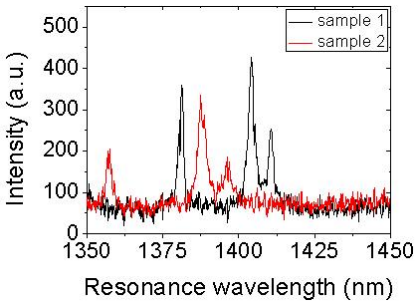

Figure 3.6: *PL spectra of two H1$_r$ cavities with the same lithographic parameters.*

3.3.3 Finite-difference time-domain simulations

Finite-difference time-domain (FDTD) simulations are a way to simulate the Maxwell equations in an isotropic medium, so also for our structures. This gives information about the mode profiles, the resonance spectra, etc.

The FDTD simulation method already existed long before two-dimensional photonic crystals were made for the first time. In 1966, Kane Yee developed this method to look at the scattering of an electromagnetic pulse by a perfectly conducting cylinder [42]. This method divides space and time into a discrete grid and calculates how the electric and magnetic fields evolve in time. This is done for discrete time steps Δt by means of a leap-frog approach.The electric fields at time t are calculated from the electric fields at $t - \Delta t$ and the magnetic field at $t - \Delta t/2$. Analogously, the magnetic field at $t + \Delta t/2$ is calculated from the magnetic field at $t - \Delta t/2$ and the electric field at t [17].

The reliability of the FDTD method is determined by the choice of grid and time spacing, Δx and Δt respectively. They both need to be as small as possible for the simulations to come as close as possible to the continuous Maxwell equations but the computer should be able to handle the calculation and the simulation time needs to stay reasonable. It makes sense that Δx

needs to be smaller than the lithographic parameters used and throughout this report, a grid spacing of $\frac{a}{16}$ was used in which a is the lattice constant in μm. This leads to a value for Δx or approximately 0.03 μm. The FDTD simulations lasted 65535 time steps with time spacing $\Delta t \sim 0.05$fs. For more information about the FDTD method is referred to [43].

3.4 Designs

This report deals with different cavity designs, all created in InGaAsP PhC membranes with a refractive index of 3.37 [44]. Independent of the design, the standard radius to lattice constant ratio $\frac{r}{a}$ of the photonic crystal pattern was always designed as 0.3. As seen in Chapter 2 this is not enough for a complete photonic band gap but it is for a TE-like band gap.
The cavity designs can be separated into two groups: the point defect cavities (paragraph 3.4.1) and the linear/heterostructure defects (paragraph 3.4.2). The different designs and the identification of the modes from the characteristic resonance spectra will be explained by looking at literature and simulations. For each cavity design, an overview will be given of the lithographic parameters used.

3.4.1 Point defects

H0 cavities

The point defect that needs the least changes to the photonic crystal pattern is a modified H0 cavity. The term H0 means that the cavity is made without leaving any holes out of the pattern and modified means that the nearest neighbor holes are reduced in radius or shifted outwards. The two types of cavities of Figure 3.7 are referred to as $H0_r$ (reduction only) and $H0_{s\&r}$ (shift and reduction). Actually, the simplest H0 cavity would be one in which only a single hole is modified. This design has already been thoroughly investigated and even patents have been obtained [45–47] which is why it was chosen not to look at this H0 design.

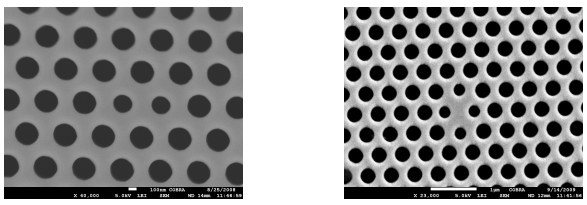

(a) (b)

Figure 3.7: *SEM images of two types of modified H0 cavities, (a) H0 reduction only, (b) H0 shift and reduction.*

The $H0_r$ cavity in Figure 3.7 (a) is created by reducing the radius of the two central holes in the x-direction of the photonic crystal pattern. From [48,

49] the modes of the photoluminescence spectra of the H0$_r$ cavity in Figure 3.8 (a) are identified as the (theoretically) doubly degenerate dipole (D1 and D2) mode and the non-degenerate monopole mode (M). The dipole mode is not truly doubly degenerate due to small asymmetries in the pattern, caused by small errors in the fabrication process. The peaks with wavelengths smaller than λ_{dipole} are peaks of higher order modes which will be neglected. The quality factors of the dipole peaks are ∼500 while the monopole mode has a quality factor of ∼1500.

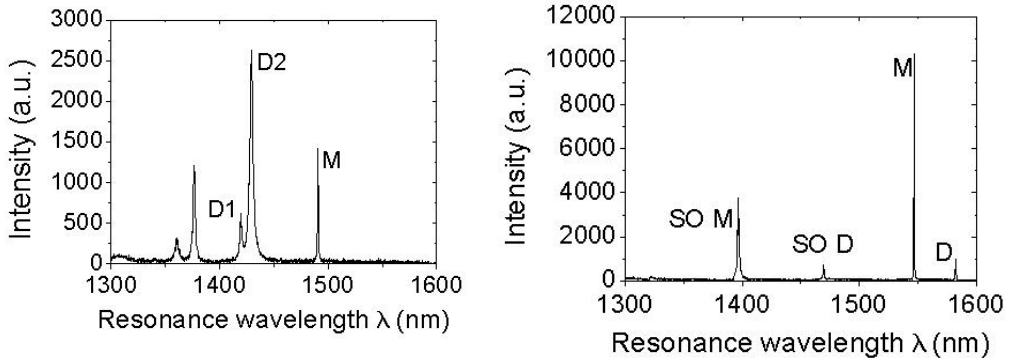

Figure 3.8: *PL spectra of the two modified H0 cavities, (a) H0$_r$ with parameters a = 530 nm and r_{red} = 0.17a, (b) H0$_{s\&r}$ with parameters a = 511 nm, r_{red} = 0.2a, s_x = 0.14a and s_y = 0.06a.*

The lithographic parameters of the H0$_r$ cavities used in this project are:

- the lattice constant a is 511, 518 or 530 nm
- the radius of the holes r is always $0.3a$
- the reduced radii are given by r_{red} with values between $0.17a$ and $0.22a$

The values for these parameters (and the lithographic parameters of all other designs) are not randomly chosen, a few guidelines were followed. First of all, the lattice constants a were chosen in such a way that the wavelengths of the resonances were between 1300 and 1600 nm because that is the range in which the quantum dots emit light. By slightly changing the modifications, the resonances are pushed through the band gap.

The H0$_{s\&r}$ cavity is created by reducing the radius of the two central holes in the x-direction and the two central holes in the y-direction and shifting these four holes outwards as shown in Figure 3.7 (b). From [48, 49] and FDTD simulations, the modes of the photoluminescence spectra of the cavity (Figure 3.8 (b)) are identified from left to right as an asymmetric second order monopole mode, a second order dipole mode, an asymmetric monopole

mode and an asymmetric dipole mode. Their mode profiles are shown in Figure 3.9. The reason that some modes are asymmetric remains unclear. It is not due to an asymmetry in the s_x and s_y values since it was not observed by the group of Baba [48, 49]. The quality factors of the H0$_{s\&r}$ cavities were approximately 800 and 1200 for the second order monopole and second order dipole mode while for the monopole and dipole modes high quality factors of 4000 and 2500 were observed.

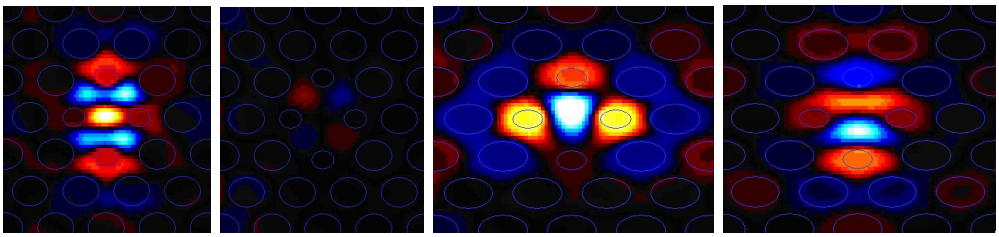

(a) (b) (c) (d)

Figure 3.9: *The simulated mode profiles for a modified H0$_{s\&r}$ cavity with parameters with parameters a = 511 nm, r_{red} = 0.22a, s_x = 0.12a and s_y = 0.01a, (a) asymmetric second order monopole mode, (b) second order dipole mode, (c) asymmetric monopole mode and (d) asymmetric dipole mode.*

The lithographic parameters of the H0$_{s\&r}$ cavities used in this project have the following values:

- the lattice constant a is 480, 499 or 511 nm
- the radius of the holes r is always 0.3a
- the reduced radii are given by r_{red} with values 0.2a, 0.22a or 0.3a (i.e. no reduction)
- the shift in the x-direction is given by s_x with values 0.12a, 0.14a or 0.16a
- the shift in the y-direction is given by s_y with values 0.06a or 0.1a

H1 cavities

The second point defect cavity design is the H1 cavity, which means that one hole is left out from the photonic crystal pattern. The cavities are modified by reducing the radius of the six nearest neighbor holes of the left-out hole as is shown in Figure 3.10 (a). This cavity design is referred to as H1$_r$. In the other type of H1, the nearest neighbors are not only reduced, they are also radially shifted outwards as is shown in Figure 3.10 (b). This cavity design is referred to as H1$_{s\&r}$.

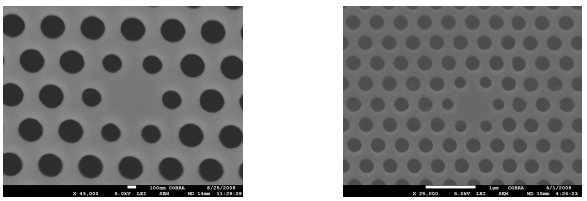

(a) (b)

Figure 3.10: *SEM images of the two modified H1 cavities, (a) H1 reduction only, (b) H1 shift and reduction.*

In this project the lithographic parameters of the $H1_r$ cavities are given by:

- the lattice constant a is 480, 499, 511, 518 or 530 nm
- the radius of the holes r is always $0.3a$
- the reduction of the radii is given by r_{red} with values between $0.17a$ and $0.26a$

and the lithographic parameters of the $H1_{s\&r}$ cavities are:

- the lattice constant a is 480, 499, 511, 518 or 530 nm
- the radius of the holes r is always $0.3a$
- the reduction of the radii is given by r_{red} with values $0.23a$, $0.24a$ or $0.25a$
- the shifts are given by s with values $0.025a$, $0.03a$, $0.04a$ or $0.05a$

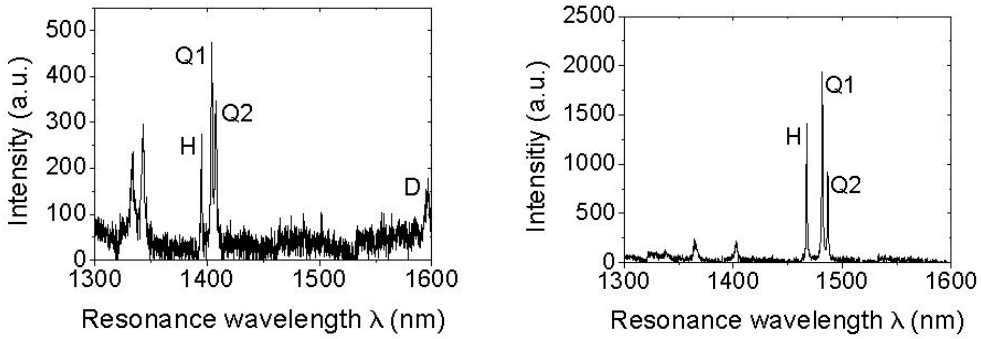

(a) (b)

Figure 3.11: *PL spectra of the two modified H1 cavities, (a) $H1_r$ with parameters $a = 511$ nm and $r_{red} = 0.22a$, (b) $H1_{s\&r}$ with parameters $a = 530$ nm, $r_{red} = 0.23a$ and $s = 0.05a$.*

Other groups have also investigated these designs [52–55] and together with Figures 3.12 (a) and (b) the modes in Figures 3.11 (a) and (b) can be identified as hexapole, quadrupole and dipole. The quadrupole as well as the dipole mode are doubly degenerate but this degeneracy is again lifted due to small, local fabrication errors that destroy the theoretical symmetry. However for the dipole mode it is not possible to see two peaks since the quality factor is too low. The quality factors for the H1 modes are on average 1500 for the hexapole peak and 1000 for the quadrupole peaks. However, for some of the $H1_r$ cavities the quadrupole peaks had quality factors of ∼2500 and the hexapole peaks values of ∼3000, proving that carefully modifying the cavities can substantially increase the quality factor.

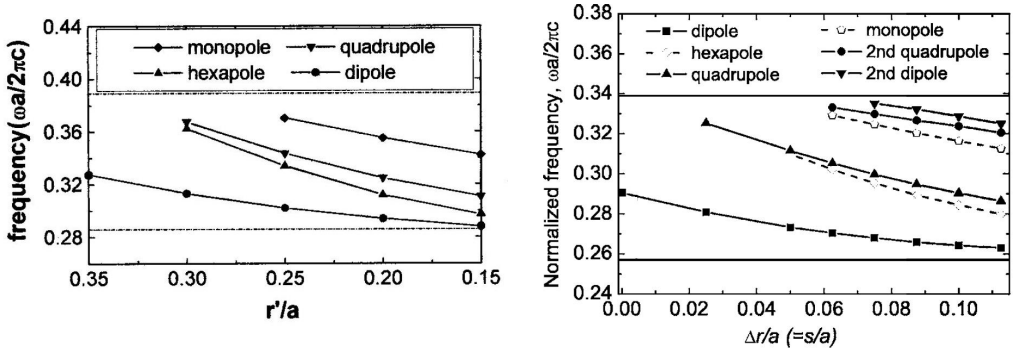

(a) (b)

Figure 3.12: *(a) Mode identification graph for $H1_r$ cavities. Simulation parameters: membrane thickness $t = 0.4a$, radius holes $r = 0.35a$, refractive index $n = 3.4$ [52]. (b) Mode identification graph for $H1_{s\&r}$ cavities. Simulation parameters: membrane thickness $t = 0.71a$, radius holes $r = 0.31a$, refractive index $n = 3.4$, the radii of the nearest neighbors are reduced by Δr and its position shifted outwards by s [53].*

The reason it is important to know the wavelength position of the modes, is that the sensitivity is determined by the value of the filling factor f. Different modes have a different overlap of the electromagnetic field with the holes and thus also a different filling factor f. Figure 3.13 shows the different modes of an $H1_{s\&r}$ cavity. It can be seen that the hexapole mode has the most overlap so its filling factor will be the largest. It is therefore expected that the hexapole mode will be the most sensitive, but also the most lossy mode with the lowest quality factor.

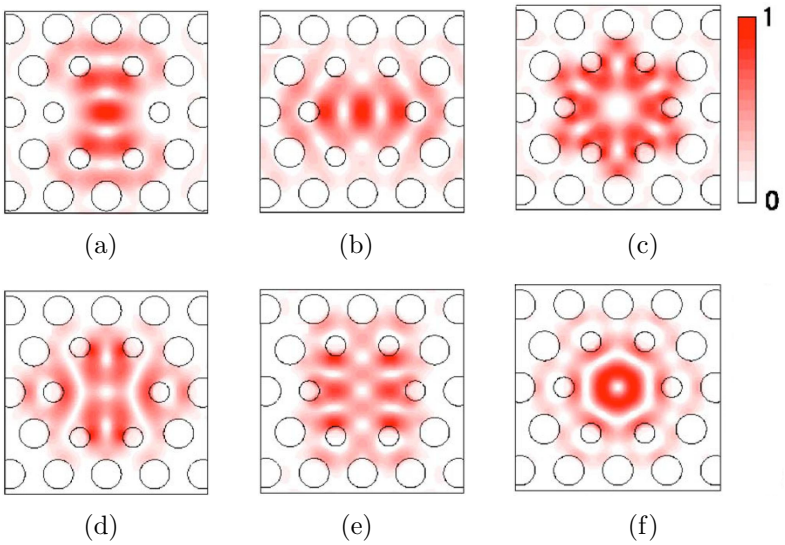

Figure 3.13: *Calculated electric field distribution for the modes of an $H1_{s\&r}$ cavity, (a) and (b) dipole mode, (c) hexapole mode, (d) and (e) quadrupole mode, (f) monopole mode [53].*

L3 cavities

The last point defect cavity design is the L3 cavity. As Figure 3.14 (a) shows, a line of three holes is left out of the pattern and the two holes at either end of the line are reduced in radius and shifted outwards. The average quality factors of the modes are 500, 500 and 1500 respectively.

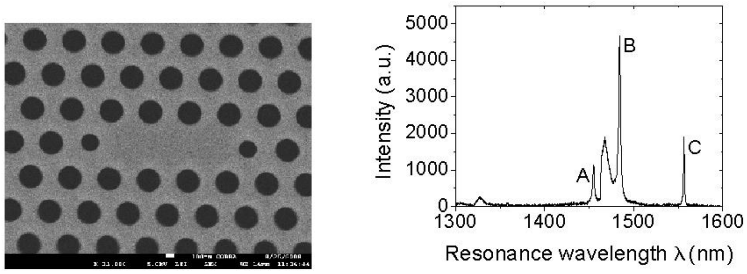

Figure 3.14: *(a) SEM image and, (b) PL spectrum of the modified L3 cavity.*

In this project several L3 cavities are used and their lithographic parameters are given by:

- the lattice constant a is 480, 499, 511 or 518 nm
- the radius of the holes r is always $0.3a$
- the radii of the two outer holes are reduced to 100 nm
- the two outer holes are shifted by s_x with values $0a$, $0.05a$ or $0.1a$

With the help of [56, 57] the modes in the photoluminescence spectrum of Figure 3.14 (b) can be identified. The mode profiles of modes A, B and C are given in figure 3.15.

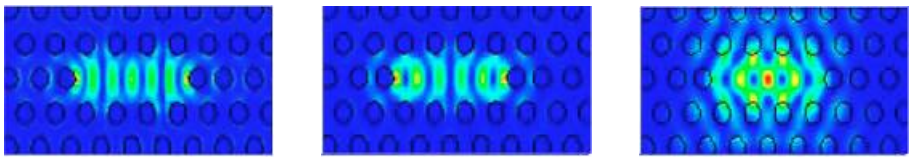

(a) (b) (c)

Figure 3.15: *Mode profiles of an L3 cavity with parameters a = 350 nm, r = 95 nm and the two outer holes are shifted by s = 0.15a (a) mode A, (b) mode B and (c) mode C [56].*

3.4.2 Linear defects combined with heterostructures

The second kind of cavities is a combination of linear defects and heterostructure defects. A photonic crystal heterostructure is a structure in which photonic crystal lattices with different lattice constants in the x-direction are placed next to each other. In the y-direction the same lattice constant holds for the entire structure. In Figure 3.16 heterostructures with two different lattice constants a_1 and a_2 and two boundaries is shown; therefore these structures are called a double-heterostructures. In Figure 3.16 (a) the white holes have a lattice constant a_1 in the x- and y-direction and the red holes have lattice constant a_2 in the x-direction and a_1 in the y-direction. For a positive defect a_1 is smaller than a_2 and for a negative defect as in Figure 3.16 (b), a_1 is largen than a_2.

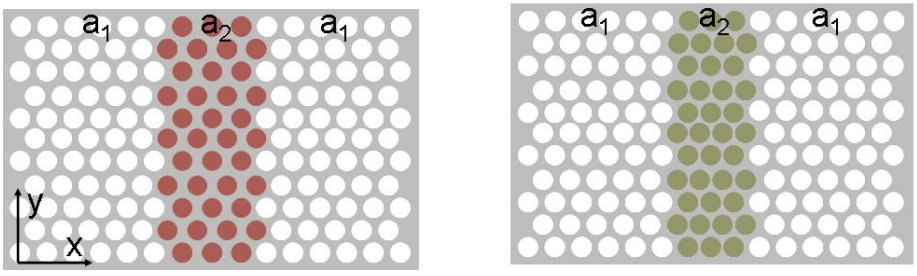

(a) (b)

Figure 3.16: *Photonic double-heterostructures with (a) a positive defect and (b) a negative defect.*

When a line of holes is removed from the double-heterostructure, a waveguide defect (W1) is created like in Figure 3.19 (a). As was seen in Chapter 2, a waveguide in a homogenous photonic crystal lattice creates several waveguide modes. These modes are inside the band gap of the photonic crystal

lattice (and also below the modes of the photonic crystal lattice). For a double-heterostructure waveguide, the waveguide modes are slightly shifted compared to in a homogenous photonic crystal latiice. If $a_1 < a_2$ the modes are shifted downwards in frequency as is shown in Figure 3.17, and if $a_1 > a_2$ the modes are shifted upwards in frequency. The mode profiles of modes a, b and c of Figure 3.17 are shown in Figure 3.18.

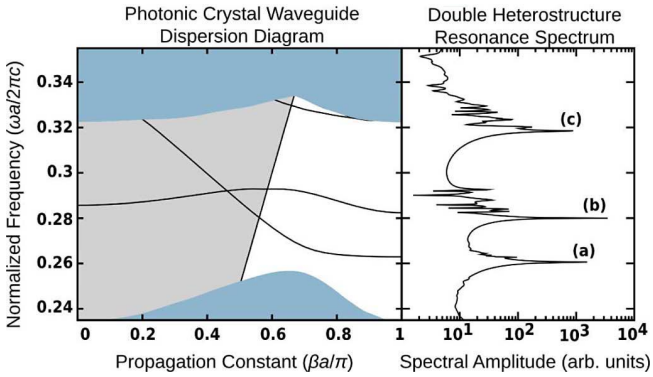

Figure 3.17: *On the left the simulated dispersion relation of a photonic crystal waveguide with the following parameters: lattice constant a_1, radius of the holes $r = 0.29a_1$, thickness of the membrane $t = 0.6$ and refractive index $n = 3.4$. On the right the calculated resonance spectrum for the corresponding double-heterostructure waveguide with $a_2 = 1.05a_1$ [62].*

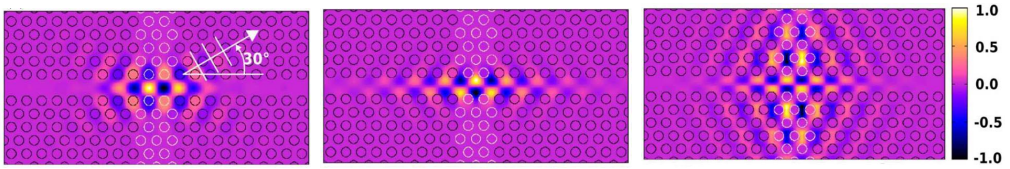

(a) (b) (c)

Figure 3.18: *The mode profiles of a double-heterostructure waveguide with parameters $a_2 = 1.05a_1$, radius of the holes $r = 0.29a_1$, thickness of the membrane $t = 0.6$ and refractive index $n = 3.4$ [62].*

In literature the waveguide double-heterostructure with positive defect is used as a cavity [60, 61]. Because locally the waveguide mode is brought down to lower frequencies, i.e. higher wavelengths, there are wavelengths that only exist in the part of the waveguide with lattice constant a_2. These modes therefore reflect at the a_1/a_2 interfaces which creates a cavity.

The lithographic parameters of the double-heterostructure waveguide cavities in this report are:

- the lattice constant a_1 is always 490 nm

- the lattice constant a_2 goes from 495 nm to 520 nm with steps of 5 nm
- the width of the photonic crystal lattice with lattice constant a_2 is 1-1.5μm (two to three holes)

Noda et al. have shown that the electric field profiles of the multi-heterostructure cavities come very close to the ideal Gaussian curves [36]. Because of this, high quality factors have been predicted and proven by experiments. However, the modal volume is approximately a factor of 6 higher than for the point defect cavities that were described earlier [64]. This implies that there is a higher overlap of the electromagnetic field of the modes with the holes, which should make these designs more sensitive to changes in the environmental refractive index. Because of their promise of high quality factors and sensitivities, heterostructure designs have been proposed and used in literature as refractive index sensors [33, 65, 66].

The principle of slots can also be introduced to double-heterostructures waveguides as in Figure 3.19 (b). For the W1 defect in Chapter 2, the dispersion relations all decreased for an increasing **k** but that was for what is called a high-index line defect. Because of the slot here it is a low-index line defect which results in increasing ω's for increasing **k**'s [63] as is shown in Figure 3.19 (c). Therefore if a_1 would be smaller than a_2, all the wavelengths inside the lattice with a_2 would be allowed to propagate into the lattice with a_1 and there would be no cavity. This is the reason that for the slotted double-heterostructure a_1 needs to be larger than a_2.

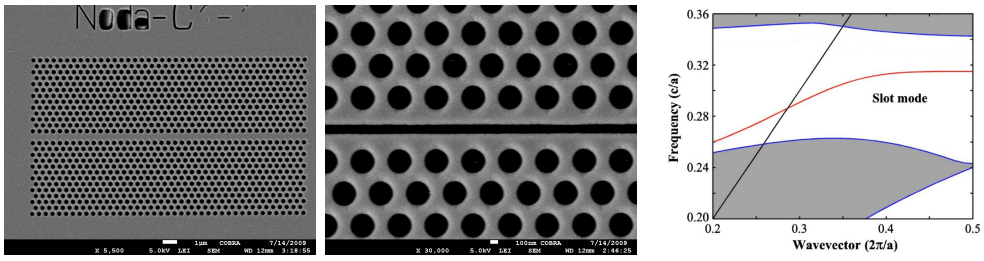

(a) (b) (c)

Figure 3.19: *SEM images of photonic heterostructures (a) double heterostructure, (b) slotted double heterostructure, (c) dispersion relation slotted double heterostructure [68].*

Like with the double-heterostructure waveguide, this slotted design has a high quality factor due to the Gaussian curves and a high modal volume as can be seen from Figure 3.20. However because of the air slot, liquids can infiltrate this structure easily which results in more overlap of the light with the liquid. It is therefore expected that high quality factors and a sensitivity that even exceeds the sensitivity of the double-heterostructure waveguides

will be obtained. Different slotted heterostructure photonic crystal cavities are proposed and used in literature as sensors [68–70].

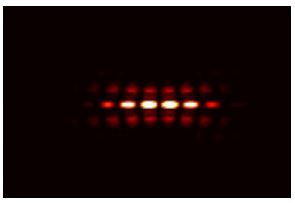

Figure 3.20: *The simulated mode profile of a slotted double-heterostructure waveguide with the following parameters: lattice constant a_1 = 490 nm, a_2 = 0.95a_1, radius of the holes r = 0.29a_1, thickness of the membrane 220 nm and refractive index n = 3.4 [67].*

The lithographic parameters of our slotted double-heterostructure waveguide cavities are:

- the lattice constant a_1 460, 470, 490 or 500 nm
- the corresponding lattice constants a_2 are 440, 450, 470 and 490 nm
- the width of the photonic crystal lattice with lattice constant a_2 is 1-1.5μm (two to three holes)
- the width of the slot is given by w with values between 0.3a and 0.45a

However, the PL spectra obtained for the double-heterostructures were not as was expected. Figure 3.21 (a) shows the PL spectra of a double-heterostructure with parameters a_1 = 490 nm and a_2 = 495 nm. Unlike in Figure 3.17, only one resonance peak was found, at λ = 1446.8 nm and the quality factor was only 162.6. Also for the slotted double-heterostructures, the spectra are not was what expected and the quality factors were low as can be seen in Figure 3.21 (b) for a structure with parameters a_1 = 490 nm, a_2 = 470 nm and slot width 0.3a. The reason for this is most probably a wrong choice of lattice constants.

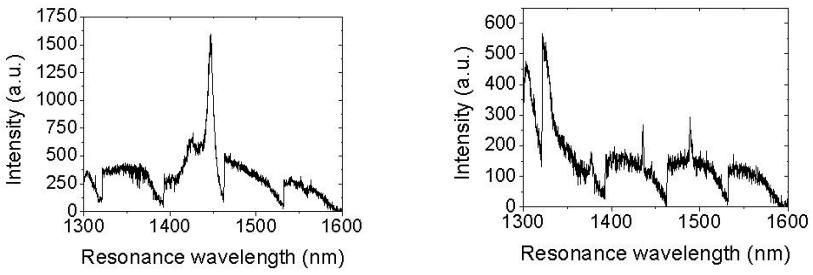

(a) (b)

Figure 3.21: *PL spectra of (a) a double-heterostructure and (b) a slotted double-heterostructure.*

Chapter 4

Binding of proteins to III/V semiconductor surfaces

This chapter is devoted to protein/surface interactions; more the binding between bovine serum albumin and III/V semiconductors. The properties of a protein are largely determined by its 3D configuration. The characteristic features of proteins and surfaces that strongly influence protein adsorption on the surface will be described. After this general introduction the focus will be on the protein bovine serum albumin (BSA), and its adsorption characteristics. This is followed by a literature overview on binding proteins, more specifically BSA, to (III/V) semiconductor surfaces. The last part of this chapter is about binding biotinylated BSA to different InP surfaces. The results of contact angle measurements, spectroscopic ellipsometry and experiments with streptavidin-coated beads will be shown and explained.

4.1 Fundamentals of proteins and their interactions with surfaces

4.1.1 Proteins

Proteins play an important role in the cell cycle, the immune system, and many other functions within the human body. They are organic structures made up from amino acids. As is shown in Figure 4.1, these building blocks consist of a central carbon atom with an amine group (-NH_2), a carboxylic acid group (-COOH), a hydrogen atom (H) and a rest group (R) which determines the properties of the amino acid. In nature, only 20 different rest groups appear and thus only 20 different amino acids exist. These rest groups determine whether the amino acid is positively or negatively charged or whether the amino acid is polar or non-polar, i.e. hydrophobic or hydrophilic [73].

The polymerization of amino acids results in a chain of amino acids, called a polypeptide. During this process, the amine group of one amino acid reacts

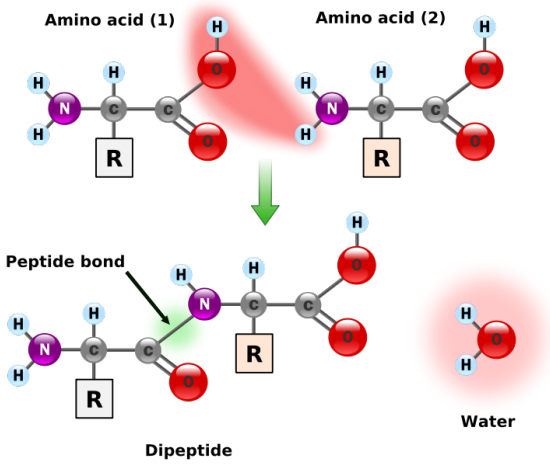

Figure 4.1: *Amino acids consist of an amine group, a carboxylic acid group, a hydrogen atom and a rest group. Two amino acids are linked to one another by a peptide bond [74].*

with the carboxylic acid group of a second amino acid. A water molecule is eliminated and a peptide bond is created (see Figure 4.1). This process can be repeated multiple times and the resulting chain of amino acids is referred to as the primary structure of the protein. A protein can contain only a few amino acids but also several thousands. A polypeptide is not just a linear chain of amino acids. Interactions between the different amino acids (hydrogen bonds) give rise to folding, bending and/or coiling of the chain which is called the secondary structure of the protein. Two regularly occurring secondary structures are the α-helix and the β-sheet, see Figures 4.2 (a) and (b). What happens often in the formation of a protein is the combination of a few secondary structures into one larger structure which is called a motif. When using α-helices and β-sheets, two of the possible motifs are the helix-turn-helix motif and the β-barrel motif, see Figures 4.2 (c) and (d). This interaction between different parts of the polypeptide chain are the result of four different types of interactions between rest groups.

The interactions between rest groups are either hydrophobic interactions between non-polar rest groups, ionic interactions between negatively or positively charged rest groups, covalent bonding or hydrogen bonds between polar rest groups. The hydrophobic interactions force the non-polar groups together, as far away from the aqueous environment as possible. Generally this means that the hydrophobic rest groups are folded towards the inside of the structure while the polar and ionized rest groups are oriented towards the outside. However, this is only a general rule. Hydrophobic amino acids can also be on the outside but then it is for a specific reason, for example to bind to other polypeptides or to a surface. The same is true for charged amino acids; when they are found on the inside of a polypeptide/protein it is often to stabilize the structure or to form an active binding site.

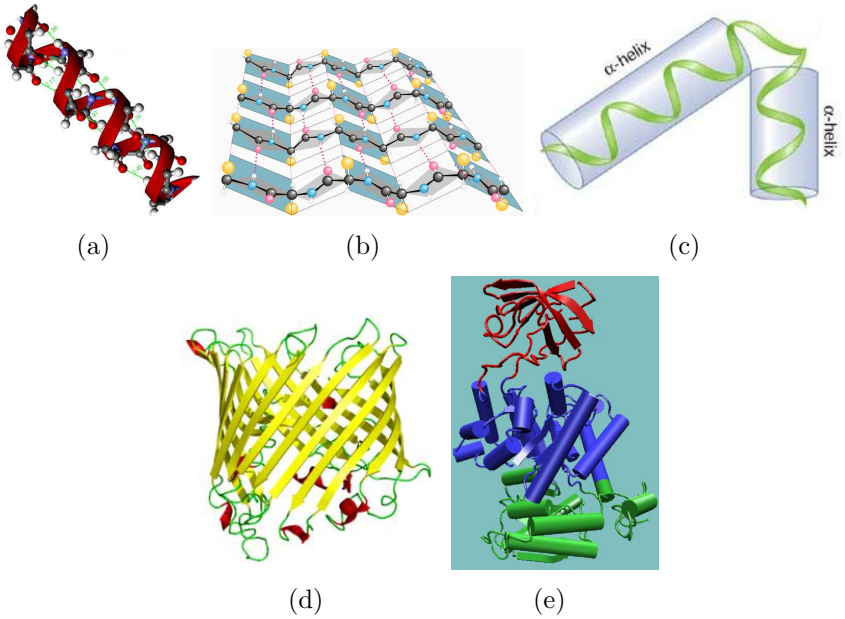

Figure 4.2: *Examples of secondary structures, motifs and domains, (a) α-helix [76], (b) β-sheets [77], (c) helix-turn-helix motif [78], (d) the β-barrel motif [79] and (e) the protein pyruvate kinase with its three domains [79].*

Several groups can be grouped together to form a unit that is referred to as a domain as the result of the same four interactions. The combination of domains like this and secondary structures is called the ternary structure of the protein. Again the four interactions between the rest groups of the polypeptide chains are responsible. The ternary structure is still a single long peptide chain but one that is able to perform certain functions. For example four α-helices can form an α-domain which can form an ion channel in a cell wall. Proteins are often composed of different domains and/or ternary structures (see Figure 4.2 (e)) that are either linked by hydrogen bonds, disulfide bonds or the same interactions as before except that they are now between amino acids on different polypeptide chains.

The conformation of a protein is very important because the function of the protein is determined by its structure. An example of this are antibodies: they are folded in such a way that only one specific protein, called the antigen, can attach at a specific binding site.

4.1.2 Protein adsorption on a surface

Before immersing a surface in a solution containing proteins, it is important to understand the general chemistry and physics behind protein adsorption onto a surface. Both proteins and surfaces have properties that affect the adsorption but but in the end, the adsorption is governed by the affinity of

the proteins towards the surface. The affinity K is defined as the ratio of the reaction rates $k_{adsorption}$ and $k_{desorption}$. Proteins with a high affinity will have a higher probability to adsorb on a surface and a lower probability to desorb. The protein and surface properties that are described in the following paragraphs all have their influence on either the adsorption or the desorption rate.

Protein properties

When proteins diffuse towards the surface, the proteins and the surface will interact by means of intermolecular bonds. This could be ionic bonds between negative and positive charges, hydrophobic interactions in which polar regions of the protein avoid non-polar regions of the surface and vice versa or charge transfer in which a stabilizing charge is transferred between two molecules. Which of these bonds will be formed depends on the properties of the protein.

The first of these properties is the size of the protein. It influences the affinity because larger proteins have a larger area that can interact with the surface as is shown in Figure 4.3. This means that larger proteins can adsorb, and stay adsorbed, more easily.

Figure 4.3: *The size dependence of protein-surface interactions.*

Since proteins are amino acid chains, the properties of the amino acids also have their influence on the adsorption of the protein. This leads to the second property: the charge of a protein. Depending on the pH of the buffer solution, the amino acids can be charged. This means that they are polar and thus more hydrophilic. As seen in paragraph 4.1.1, hydrophilic amino acids have a tendency to be on the outside of the protein where they can interact with the polar regions of the material surface. The negatively charged regions on the outside of the protein prefer the positively charged surface regions and vice versa. However, proteins adsorb the most at their isoelectric point which is defined as the pH of the buffer solution at which the proteins carry no net electrical charge, i.e. they are neutral. At this point the electrostatic repulsion with other proteins on the surface is reduced which leads to an increase in adsorption [72].

The third protein property that influences the adsorption is the hydrophobicity or hydrophilicity of the proteins. Hydrophobic (non-polar) regions tend

to adsorb to hydrophobic surfaces and hydrophilic (polar) regions tend to adsorb to hydrophilic surfaces. As stated before, when the protein is in solution, the hydrophobic regions tend to be on the inside of the protein. But when the protein adsorbs and unfolds, these regions may become exposed and free to interact with the surface and the protein loses its biochemical selectivity.

The (thermodynamic) stability of the protein is determined by its conformation. Proteins with a low stability have less internal bonding and/or cross-linking and they tend to adsorb more readily than more stable proteins. This is because they unfold more easily which results in more protein surface area that is free to interact with the surface.

Surface properties

Besides the protein properties, also the surface properties have their influence on the protein adsorption. If the surface is hydrophobic as in Figure 4.4 (a), binding will occur with the hydrophobic amino acids on the inside of the protein. For this the interface needs to be dehydrated and the protein needs to change its conformation in such a way that the hydrophobic parts are at the protein/surface interface and the hydrophilic parts at the protein/water interface. Therefore an increase in conformational changes are seen with hydrophobic surfaces. On a hydrophilic surface the interaction between surface and protein will occur via hydrogen bonds between the polar regions as can be seen in Figure 4.4 (b). However, hydrogen bonds can also be formed between the water molecules in the solution and the surface which leads to a competition between proteins and water molecules. Therefore hydrophilic surfaces will have less protein adsorption and no conformational chance is necessary. A second difference between hydrophobic and hydrophilic surfaces is the number of proteins that are/stay adsorbed. On a hydrophobic surface, the proteins will unfold which leads to a low desorption rate and thus a higher affinity.

The second surface property is the charge (distribution) of the surface. When the surface and the protein have opposite charges, they will be attracted to each other which leads to an increase in adsorption and like charges repel each other which leads to a reduction in adsorption. The surface potential influences the distribution of ions in the solution and also the interaction with proteins.

Thirdly the topography of the surface that plays an important role in the adsorption of proteins. If the surface roughness is increased, whether or not intentionally, more surface area is available for protein adsorption. Because proteins are so small (of the order of nm), small topological features can lead to a large increase in adsorption.

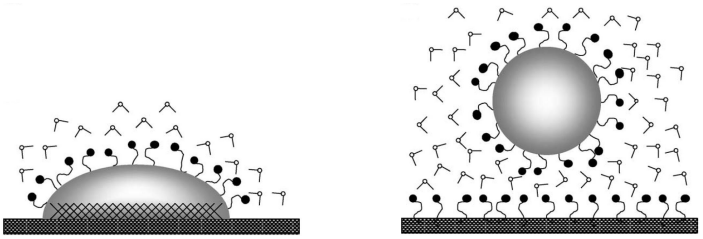

Figure 4.4: *Schematic representation of protein adsorption to (a) hydrophobic and (b) hydrophilic surfaces. Polar groups are shown as black dots and water molecules as white dots. The shaded area in (a) represents hydrophobic part of the surface [75].*

Also the heterogeneity of the surface is of interest. If the surface is not uniform, there will be regions that interact strongly with the proteins in regions for which the interaction is less.

The chemical properties of a surface can influence the adsorption of proteins. Therefore introducing surface functional groups like methyl (hydrophobic), hydroxyl (hydrophilic), amine (hydrophilic) or carboxyl (hydrophilic) groups will change the adsorption. It is also possible to bind self-assembled monolayers to the surface. Examples of self-assembled monolayers and III/V semiconductors will be given in paragraph 4.3.

4.2 Bovine Serum Albumin

4.2.1 The albumin protein

Serum albumin is the most occurring protein in human plasma. It performs several function in the human body, one of them being a transport vehicle for hydrophobic proteins by non-specific binding. Its bovine counterpart, bovine serum albumin (BSA), is widely used for biochemical applications as a stable surface covering molecule. It is made from approximately 600 amino acids which gives it a molecular weight of about 66 000 atomic mass units. Originally, BSA was considered to be an ellipsoid with dimensions 4×4×14 nm [80, 81], but later this was corrected to the heart-shaped structure shown in Figure 4.5 [82, 84]. BSA is a protein that has been thoroughly investigated, so in literature a good description of all its structures can be found [84]. The primary structure consists of three identical polypeptide chains [83].

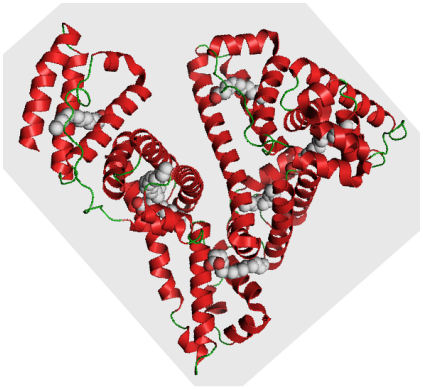

Figure 4.5: *The heart-shaped 3D structure of bovine serum albumin [84].*

4.2.2 Binding of BSA to a polystyrene surface

To illustrate the binding of BSA to a surface, the binding of BSA to polystyrene, a hydrocarbon chain with formula $(C_8H_8)_n$ will be discussed. Browne et al. have investigated the effects of treating the polystyrene surface to the adsorption of BSA [75]. They state that BSA has a higher adsorption on hydrophobic surfaces than on oxidized, i.e. hydrophilic, surfaces. Furthermore, adsorption onto non-oxidized polystyrene surfaces is the result from dispersion interactions (a type of van der Waals force) between non-polar amino acids. This implies that the protein needs to change its conformation because in an aqueous environment the non-polar amino acids are on the inside of the protein conformation. Adsorption on oxidized polystyrene surfaces can occur without a change in conformation due to an interaction of polar groups on the surface and the outside of the protein. But as was seen in Figure 4.4, this means that water molecules can interfere with these bonds, making it a relatively weak bond. It can be concluded that if one wants a stable bond between BSA and the surface, oxidation needs to be avoided.

Swerydo-Krawiec et al. state that BSA adsorption on a hydrophobic surface occurs gradually until full passivation of the surface is reached [87]. On the other hand, on hydrophilic surfaces the adsorption happens in two steps. In the beginning the affinity is very high but at a certain coverage, further BSA adsorption occurs with a lower affinity. This implies that BSA coverage on hydrophilic surfaces occurs via two different mechanisms but little is know about what these adsorption mechanism really are. Furthermore they say that the ternary structure of the protein is lost in controlled, discrete steps. The layer structure that is formed on the surface is very specific and it inhibits further protein adsorption, regardless of the chemical composition of the underlying layer. This is a very important property since it explains why only monolayers of BSA are formed on a surface.

4.2.3 Binding of biotin to streptavidin

The protein streptavidin is a protein that is famous for its interaction with another molecule called biotin or vitamin H. Together they form the strongest, non-covalent bond known in nature. There are two main reasons why this bond is so strong. First of all, there are van der Waals interactions between biotin and streptavidin and secondly, the surface polypeptide chains of streptavidin bury the biotin in the streptavidins interior which causes a conformation change in the quaternary structure of streptavidin [86]. As Figure 4.6 shows, each streptavidin molecule has four available binding sites for a biotin molecule.

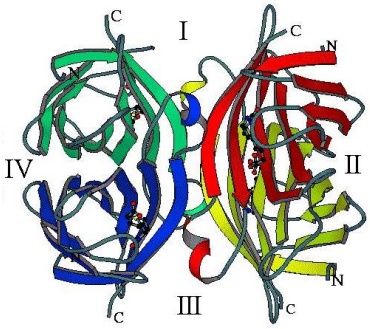

Figure 4.6: *The three-dimensional structure of streptavidin, the biotin binding sites are denoted with I, II, III and IV [85].*

The biotin molecule is very small (its molecular weight is only 244 atomic mass units) and can be easily bound to other proteins. In this report, biotin will be used to functionalize the surface of the BSA proteins which will make it possible to attach streptavidin molecules to the biotinylated BSA (bBSA).

4.3 Binding of proteins to III/V semiconductor surfaces

The binding of proteins to semiconductor surfaces is currently a hot topic, not only within the field of photonic crystals, but also for other biochemical sensor platforms based on (III/V) semiconductors [88–90]. There are three possibilities: directly binding the protein to the semiconductor surface, functionalizing the surface with a linker molecule that covalently binds to both surface and protein or functionalizing the surface with a self-assembled monolayer (SAM) for which the protein has a high affinity . Ideally one wants to obtain homogenous binding of proteins to a surface that has received (almost) no treatment and without using a linker molecule. This is however not always possible due to, among other things, surface heterogeneity and surface charge. In this literature overview both the direct binding of proteins to a III/V semiconductor surface and use of linker molecules will be discussed.

4.3.1 Binding by functionalizing the surface

By adsorbing first linker molecules onto the semiconductor surface, a uniform surface is obtained to which proteins can bind easily if the end group of the linker is chosen carefully. The covalent binding of linker molecules to metals has already been intensely investigated, this in contrast to III/V semiconductors. The reason for this is the presence of a thin layer of native oxide on the III/V semiconductors which can make the binding process more complicated. In 2007, Park & Ivanisevic were the first to do a systematic investigation of the use of linker molecules on InP surfaces [91]. Their goal was to find specific functional groups that would bind to the InP surface via covalent or ionic bonds. One of the advantages of covalent bonds is their stability which would give a long life-time to the biosensor applications. Another advantage is the control over the conformation of the linker molecule which in turn gives control over the selectivity and the specificity of the biosensor [94]. Park & Ivanisevic investigated the binding of both alkanethiols (hydrocarbon chains of different lengths ended at one side by a thiol group) and peptides (short chains of amino acids). Both hydrocarbon chains and peptides can be closely packed on a surface due to van der Waals forces and interactions between amino acids (4.1.1) respectively. Park & Ivanisevic found that monolayers of alkanethiols would self-assemble onto InP (100) surfaces via a bond between indium atoms on the surface and the sulfur atom of the thiol. Positively charged peptides would interact with the surface via ionic bonds.

Goede et al. have looked at peptide bonding on different III/V semiconductors [97]. They chose for peptides because they were interested in the material recognition properties of peptides. This is necessary when you have a surface made of different materials and you want the binding only to occur at one of them. Goede et al. took a peptide with a strong preference to bind to GaAs(100) and looked at the peptide adhesion coefficient, i.e. the percentage of surface area covered by the peptide, on different III/V semiconductors. Naturally, the peptide adhesion coefficient was the largest for GaAs(100) but more importantly, they were able to explain the differences in this coefficient between the different semiconductor surfaces. The peptide adhesion coefficient does not depend on the lattice constant or the band gap but on the electronegativity of the semiconductor. The chosen peptide had amino acids with mostly polar and basic rest groups and therefore prefered to bind to a surface with a certain surface polarity and acid binding sites. Additionally, the chemical composition and conformation of the peptide are important to optimize the peptide adhesion coefficient.

Estephan et al. looked at peptides because like Goede et al. they wanted material specific binding. More specifically, they used biotinylated peptides to control the position of biotin molecules on a semiconductor surface [92]. They observed that when they bound a biotinylated peptide specific for InP on an InP surface and next incubated this sample with streptavidin, a full

surface coverage of streptavidin molecules was formed. They state that the advantage of using small peptide linkers is that they can be used to immobilize other molecules onto semiconductors thereby opening new doors for the engineering of organic/inorganic hybrid devices like biosensors.

Wampler & Ivanisevic [93] have shown that octadecanethiol fully passivates an InP surface. Furthermore the octadecanethiol proofs to be a good surface to bind bBSA as is seen in Figure 4.7. Wampler & Ivanisevic were also able to attach streptavidin coated gold nanoparticles to the bBSA. This means they were able to adsorb the biotinylated BSA-streptavidin duo onto InP by functionalizing the surface. Several other groups have also obtained surface passivation of GaAs and InP surfaces with different thiols [98–103].

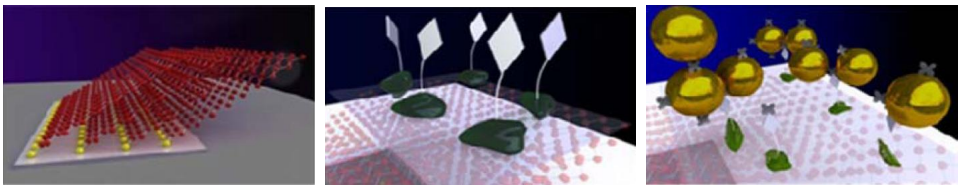

(a) (b) (c)

Figure 4.7: *Schematic representation (a) the binding of octadecathiol to InP, (b) the binding of biotinylated BSA to octadecanethiol and (c) the binding of streptavidin-coated gold nanoparticles to biotin molecules [93].*

4.3.2 Direct binding

Little work has been done on the direct binding of BSA to semiconductor surfaces. To the best of our knowledge, only Losurdo et al. have reported on the functionalization of Si(100) and GaAs(100) with BSA [95]. This group reports that the native oxide layer does not inhibit the formation of a monolayer of BSA, contrary to other biomolecules, since they only degreased their surfaces in a solution with trichloroethylene, acetone, methanol and deionized water. They also observe that the bond between BSA and GaAs is characterized by a strong electrostatic component, which was previously also stated by [96]. Because of this result and because it requires only little surface preparation, this report will look at the direct binding of proteins to a III/V semiconductor surface. To do this, several surface treatments were investigated in paragraph 4.4.

4.4 The binding of bBSA to InP

4.4.1 Experiments with streptavidin-coated beads

In this paragraph the binding of bBSA to treated InP(100) wafers with streptavidin-coated beads (Dynabeads, Invitrogen) is investigated. It is im-

possible to see individual bBSA molecules on the InP surface with a simple microscope but their presence can be detected by using the streptavidin-coated beads. They have a diameter of approximately 2.8 μm which is visible with a normal microscope.

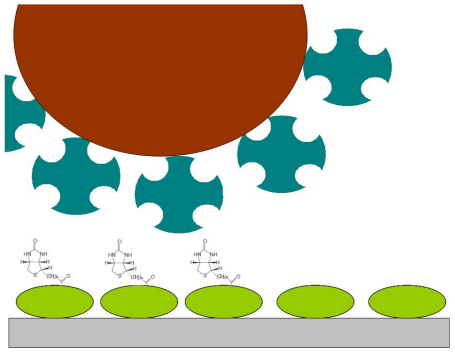

Figure 4.8: *The binding of a streptavidin-coated bead to a surface covered with biotinylated BSA (not drawn to scale).*

Before looking at InP surfaces, first a reference experiment with glass was done. First a circular, double-sided adhesive or spacer (SecureSeal Imaging Spacers, Grace Bio-Labs) was applied to a piece of glass as is seen in Figure 4.9 (a) and (b). Next the glass surface was incubated with either 2 mg/mL bBSA in a 0.14 mM citrate buffer with pH 6.8 (9 moles biotin per mole BSA, Pierce Biotechnology) or 10 mg/mL BSA in a 20 mM potassium phosphate buffer with pH 6.5 (Calbiochem) for respectively 20 hours and 1 hour at 4°C. Afterwards the samples were rinsed with Milli-Q water and blown dry with N_2.

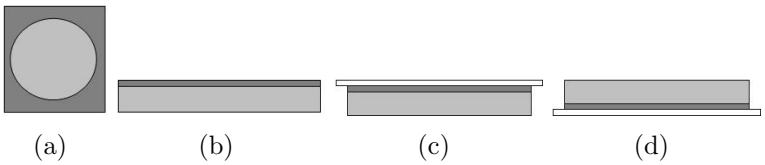

Figure 4.9: *Schematic representation of the glass samples (a) top view of the glass and adhesive, (b) side view of the glass and adhesive, (c) with cover glass and (d) rotated sample (not drawn to scale).*

Next, the samples, including blanks, were incubated with a 1:200 solution of the streptavidin coated beads in a 5 mM phosphate buffered saline solution. Earlier experiments had shown that at this concentration of salt, the Debye length is small enough for part of the rough beads to attach to the glass surface. This means that if no protein is on the surface, beads will bind and if BSA is on the surface, no beads will bind. On the contrary, if bBSA is on the surface, all beads should bind due to the strong interaction between biotin and streptavidin. After 15 minutes, the beads had had enough time to diffuse towards the surface and possibly bind and a thin cover glass was

placed on the adhesive and the sample is rotated as in Figures 4.9 (c) and (d). All unbound beads fell down because of gravity during the next 15 minutes. By means of inverted microscopy (Leica DMI5000 M, Leica Microsystems B.V.) images of the cover glass and next of the glass surface were taken. In Figure 4.11 the results of this reference experiment can be seen. For the blank glass surfaces it was expected to see beads that were non-specifically bound to the glass surface and beads that were laying loose on the cover glass as in Figure 4.10 (a). For the BSA glass surfaces it was expected to see all beads on the cover glass and no beads on the surface as in Figure 4.10 (b) and the exact opposite was expected for the bBSA glass surfaces as can be seen in Figure 4.10 (c).

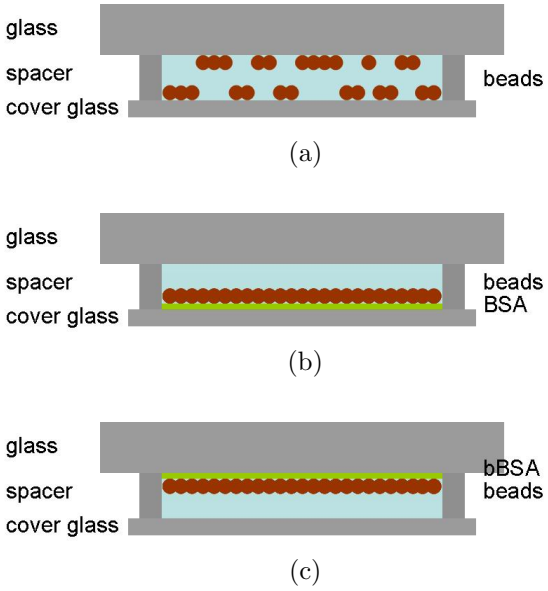

Figure 4.10: *Expectations for the glass samples for (a) the blank sample, (b) the BSA sample and (c) the bBSA sample. Figures not drawn to scale.*

The glass surface was marked with a scratch before the incubation which made it easy to focus on this plane with the microscope. Afterwards the focus plane was brought down ∼120 μm, i.e. to the top of the cover glass. The images taken with the microscope were analyzed with a MATLAB program (The Mathworks) that counted the number of beads. Figure 4.11 shows that for the blank samples, beads are both on the glass and on the cover glass, in this case 116 beads are on the cover glass and 151 on the glass surface itself. These experimental results agree with the expectation of Figure 4.10 (a). With a layer of BSA on the glass surface, the electrostatic interaction between the beads and the surface is prevented which is why on the glass surface no beads are counted and 373 on the cover glass. For the bBSA incubated glass surface 287 beads are found on the glass surface and no on the cover glass. So also for the incubated glass surfaces, the results match the expectations. The large, grey, unfocussed spots in the images of Figure 4.11 are probably dust particles.

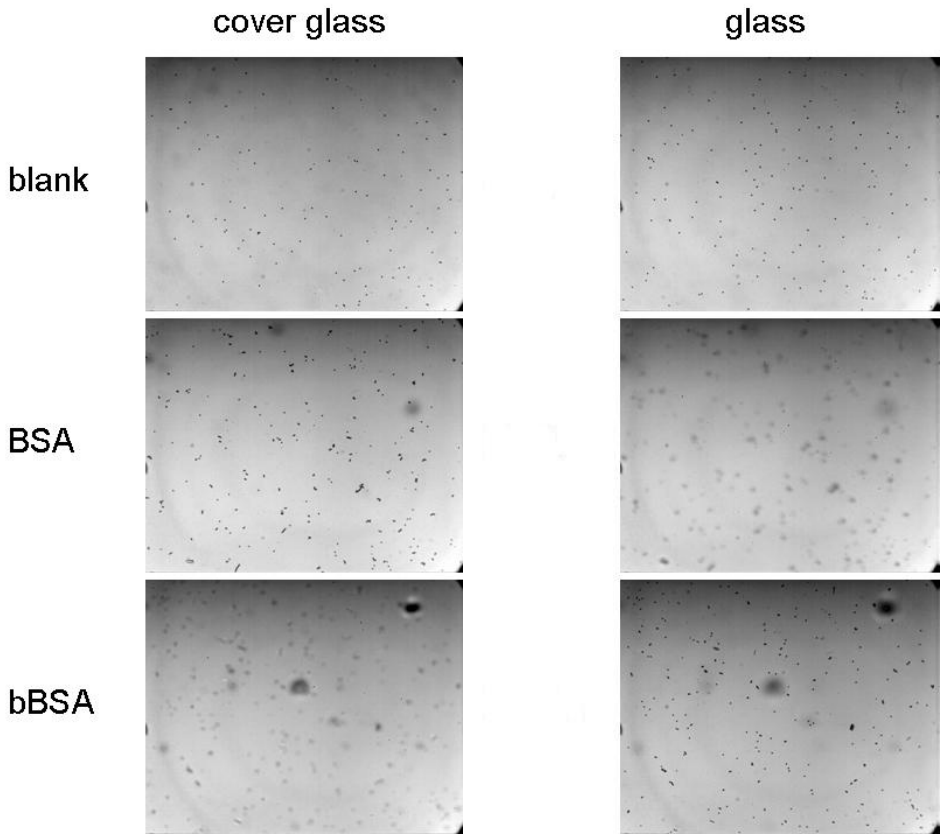

Figure 4.11: *Results of the glass samples for the blank sample (top row), the BSA sample (middle row) and the bBSA sample (bottom row). Microscope images were taken at magnification 20× for (a) the cover glass and (b) the glass surface.*

InP surfaces with different surface treatments were investigated to see on which surface bBSA binds best. There was an untreated InP sample, a sample that had undergone an oxygen plasma for 10 minutes, a sample that was etched with a H_20:H_3PO_4 = 10:1 solution for 5 minutes and a sample that first had the oxygen treatment and next the etch. Four samples of each treatment were used for these bead experiments. Different than with the glass samples, only a small drop of bBSA solution was applied to the sample. This drop did not fully cover the InP surface so the beads were only expected to bind on a small circle. The bBSA was again incubated for 20 hours at 4°C after which it was rinsed and blown dry. Next the samples were incubated with BSA for 1 hour at 4°C. BSA will only bind to the free InP surface and will be washed of the bBSA covered surface (see paragraph 4.2.2). Next the beads were applied, 15 minutes later the cover glass is applied and the sample was rotated and 15 minutes later we looked at it through the inverted microscope.

The number of beads differed for different samples with the same treatment, probably because the number of beads in each drop was not the same, but a general trend between the different treatments was observed. When the average of four samples is taken for each treatment, the number of counted beads are given in Table 4.1. The observed trend is that the number of beads on the InP surface increased from no treatment to H_3PO_4 treatment, to O_2 treatment and to O_2 and H_3PO_4 treatment. At the same time the number of beads on the cover glass decreased from no treatment to H_3PO_4 treatment, to O_2 and H_3PO_4 treatment and to O_2 treatment.

Table 4.1: *The average number of beads on the InP surface and the cover glass for each of the four treatments.*

treatment	InP surface	cover glass
No	75	186
O_2	185	83
H_3PO_4	121	148
O_2 and H_3PO_4	266	99

The samples with both the oxygen and etch treatment had the highest number of beads on the InP surface combined with a low number of beads on the cover glass. An example of these images is given in Figure 4.12. On these samples the edge of the bBSA drop was also clearly visible as is shown in Figure 4.13.

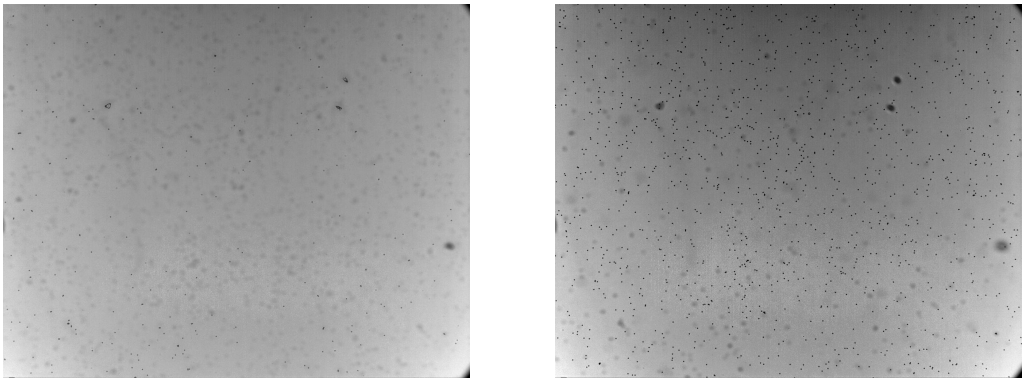

(a) (b)

Figure 4.12: *Microscope images of an InP substrate with O_2 and H_3PO_4 treatment (magnification 10×). The images are taken within the bBSA circle and focused on (a) the cover glass and (b) the InP surface. the number of beads on the cover glass is 175, on the InP surface 1310.*

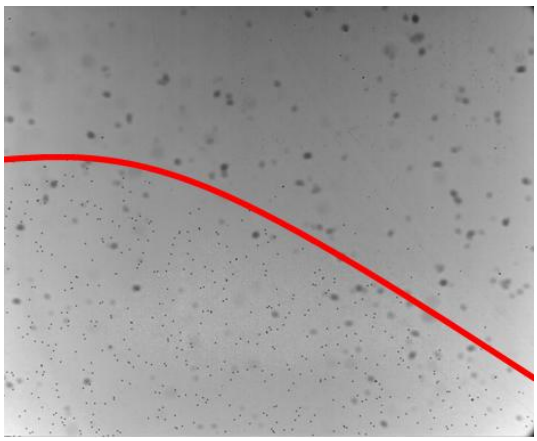

Figure 4.13: *Microscope image of the edge of the bBSA drop (left bottom corner) on the InP surface with O_2 and H_3PO_4 treatment (magnification 10×). The (unfocused) larger dark grey areas are clusters of beads on the cover glass.*

4.4.2 Contact angle measurements

To investigate the hydrophobicity/hydrophilicity of the different InP surfaces, contact angle measurements with a drop of water were performed. As is shown in Figure 4.14, during a contact angle measurement both the bottom of the water drop and its tangent line need to be aligned with a cursor. The value of the contact angle can then be read out at the intersection of the tangent with the goniometer.

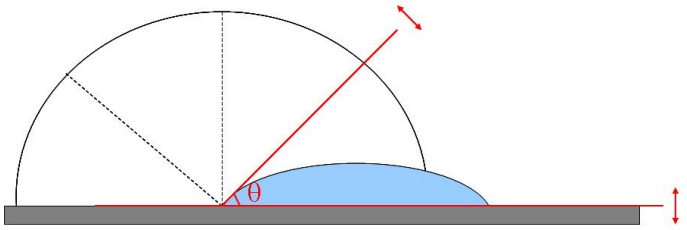

Figure 4.14: *An example of a contact angle measurement were the contact angle θ is 45°.*

Table 4.2 shows the results that were obtained for two contact angle measurements for all four treated InP surfaces. By definition, only surfaces with $\theta > 90°$ are hydrophobic so the first conclusion that can be drawn is that none of the surfaces are truly hydrophobic. But decrease in hydrophilicity is seen when going from O_2 treatment, to O_2 and H_3PO_4 treatment, to H_3PO_4 treatment and to no treatment.

Table 4.2: *The results from contact angle measurements with a water drop.*

	no treatment	only O_2	only H_3PO_4	O_2 and H_3PO_4
measurement 1	69°	8°	50°	14°
measurement 2	66°	9°	40°	15°

4.4.3 Spectroscopic ellipsometry

To get an idea of the layer thickness of the adsorbed bBSA layer, spectroscopic ellipsometry experiments were performed. Spectroscopic ellipsometry is a good method to obtain more information about the structure and the optical constants of thin film structures. By irradiating *s*- and *p*-polarized light waves onto a sample at its Brewster angle, useful information can be obtained from the change in the polarization of these light waves. Generally light waves are distinguished by the oscillatory direction of its electric field. For *p*-polarization, the electric fields of both incident and reflected light waves oscillate in the plane of incidence while for *s*-polarization the electric fields of the incident and reflected light waves oscillate perpendicular to the plane of incidence as in Figure 4.15. The Fresnel equations lay on the basis of ellipsometry and for reflection amplitude coefficients they are given by

$$r_p = \frac{n_t \cos(\theta_i) - n_i \cos(\theta_t)}{n_t \cos(\theta_i) + n_i \cos(\theta_t)} \tag{4.1}$$

$$r_s = \frac{n_i \cos(\theta_i) - n_t \cos(\theta_t)}{n_i \cos(\theta_i) + n_t \cos(\theta_t)} \tag{4.2}$$

where i and t stand for incoming and transmitted and the angles θ are the angles between the light ray and the plane of incidence. As is seen from equations 4.1 and 4.2, *s*- and *p*-polarized waves have different reflection coefficients which is something that is used in spectroscopic ellipsometry since experiments are done at the Brewster angle. By definition, the Brewster angle is the angle of incidence at which *p*-polarized light is completely transmitted. At this angle, the difference between r_p and r_s is maximized. Since spectroscopic ellipsometry measures the ratio r_p/r_s of these reflection amplitude coefficients (see further), the measurements are most sensitive at the Brewster angle.

As is shown in Figure 4.16, ellipsometry measures two values, ψ and Δ that express the amplitude ratio and phase difference between *s*- and *p*-polarized waves respectively. These two parameters are defined by $\rho \equiv \tan\psi \cdot e^{i\Delta}$ which is defined by the ratio of the amplitude reflection coefficients for *p*- and *s*-polarization. To go from the two measured quantities ψ and Δ to information about the structure or the value of optical constants, a schematic

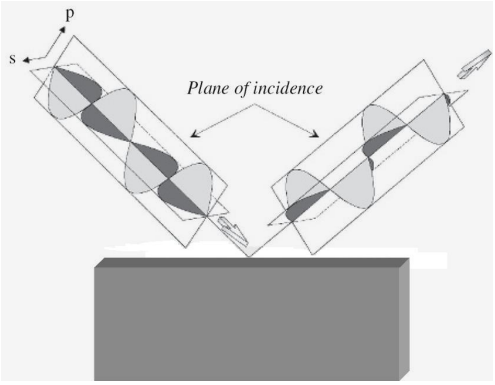

Figure 4.15: *The reflection of s- and p-polarized light waves [105].*

representation of the structure containing the complex refractive index and layer thickness of each layer is needed.

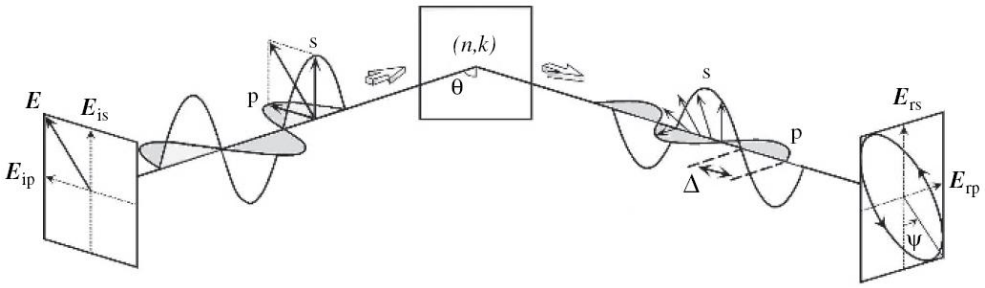

Figure 4.16: *The measurement principle of spectroscopic ellipsometry [105].*

In Figure 4.17 (a) such a schematic representation is shown. This figure also shows that when the light absorption in a thin film is small, optical interference occurs between the multiple reflections. Because the incident angle is the Brewster angle, this interference is destructive. The value of ρ is determined by the complex refractive indices N_0, N_1 and N_2, by the thickness of the layer d and by the angle of incidence θ_0. The complex refractive index of air is $N_0 = 1$ and the values of N_2 and θ_0 are usually known. The transmission angles θ_1 and θ_2 can be calculated from the angle of incidence θ_0 via Snell's law.

In the (ψ,Δ) spectra shown in Figure 4.17 (b), the optical interference effect appears in the energy region where optical light absorption is relatively small, $h\nu < 2.5$ eV. From the analysis of this interference pattern, the thickness of the thin film d can be estimated. If d is determined from this analysis, the only unknown parameter of ρ is $N_1 = n_1 - ik_1$. The two values (n_1,k_1) can be obtained from (ψ,Δ). The low-energy region gives values for the optical constants and the thickness of the thin film; the high-energy region gives information on the band structure and surface roughness. At these high energies, light absorption in the samples generally increases and the pene-

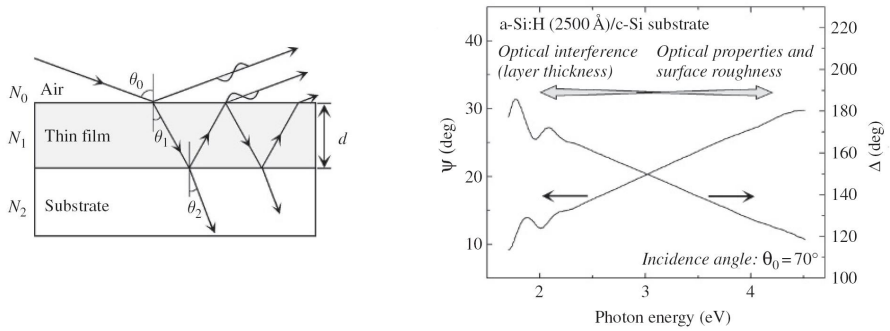

(a) (b)

Figure 4.17: *(a) A schematic representation of an air/thin film/substrate structure and (b) (ψ,Δ) spectra obtained from an amorphous silicon (a-Si:H) thin film (252 nm) on a crystalline Si (c-Si) substrate [105].*

tration depth of light becomes smaller which means that optical interference becomes negligible.

At low energies the refractive index as a function of the wavelength can be determined by fitting the collected spectra to an appropriate optical model. In the simplest case, when the layers are transparent and homogeneous, the refractive index n as a function of the wavelength λ can be described using a Cauchy model which is given by

$$n(\lambda) = A + \frac{B}{\lambda^2} + \frac{C}{\lambda^4} \tag{4.3}$$

with A, B and C constants fitted by the model.

In this report, spectroscopic ellipsometry (SE) was used as a non-invasive technique to analyze the surface of the treated InP to obtain information on the surface coverage with bBSA as was also done by [95, 104]. InP wafers with two different treatments were investigated; one sample had received the O_2 treatment of 4.1 and the second sample had received both the O_2 and H_3PO_4 treatment. This choice was made since most of the streptavidin-coated beads bound to these surfaces in paragraph 4.4.1. For each of these samples, a reference measurement of the treated surface was taken and a measurement with a layer of bBSA. For the calculations, both InP wafers, that in practice contain an oxide layer, were simplified into one layer of InP with standard optical values. As is shown in Figure 4.18, the obtained spectra[1]have wave numbers between 5500 and 8500 cm^{-1} which corresponds to a wavelength range of 1175-1820 nm or a photon energy between 0.65 and 1.05 eV. This means that these measurements are in the energy range in which light absorption is small and the values N_1 and d can be determined.

The obtained (ψ,Δ) spectra are shown in Figure 4.18. For the sample with O_2 treatment only, the calculated thickness was 1.4 nm and for the sample with O_2 and H_3PO_4 treatment the thickness was 1.5 nm.

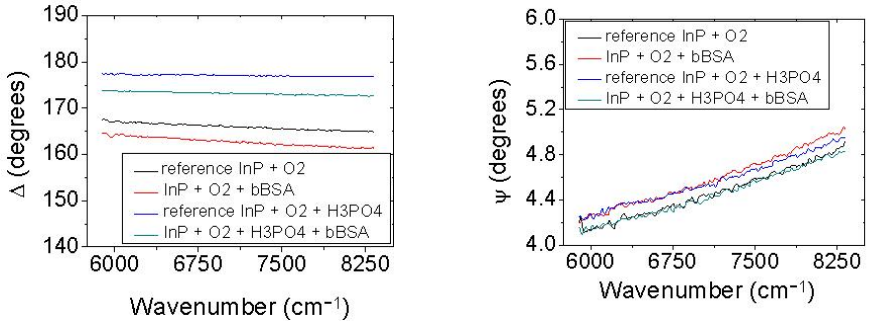

(a) (b)

Figure 4.18: *Spectroscopic ellipsometry measurements on our samples as a function of wavelength.*

The spectra were fitted with to Cauchy model of equation 4.3 with values A = 1.353, B = 1096.2 10^2 and C = 643.9 10^7 for the O_2 treated InP and values A = 1.651 , B = -3120.4 10^2 and C = 2078.3 10^7 for the O_2 and H_3PO_4 treated InP. At 1550 nm, the calculated refractive index of the bBSA layer was 1.4 for the sample with O_2 treatment only and 1.525 when the sample had also received an H_3PO_4 etch. For comparison, the refractive index of proteins, and thus also of bBSA, is typically 1.445 [109].

The thicknesses that are obtained, 1.4 or 1.5 nm, are too small (see paragraph 4.2.1). Both treatments give rise to hydrophilic surfaces, see Table 4.2, so it is expected that the BSA molecules will not unfold but keep their full volume which is approximately 4 nm when they are flat on the surface or 14 nm when they stand tall on the surface. The bBSA layer thickness observed by [93], is 1.35 nm but this was on a hydrophobic surface so the BSA molecules were unfolded. However, the spectroscopic ellipsometer can not see a difference between a surface fully covered with a 1.4/1.5 nm layer and a surface on which bBSA molecules stand separately from each other. It could be that we are in the latter situation and that this is the reason the SE measurements underestimate the thickness. However, if this was the case, the calculated refractive index should not exceed the value of 1.445. Also the large difference in calculated refractive index values for the bBSA layer can not be explained. A more thorough investigation is needed in which more attention is given to the layer structure and the fitting parameters. At this point we can only state that the addition of a layer is observed after bBSA incubation which gives us the confidence to say that if the fitting is optimized, spectroscopic ellipsometry can be used in the future to investigate bBSA binding to InP surfaces.

[1]These measurements and subsequent fitting were done by T. de Vries.

4.4.4 Conclusions

Because Losurdo et al. have shown that it is possible to bind BSA directly to a III/V semiconductor surface it was decided to try and bind bBSA directly to InP. Whether this was successful or not was investigated with both bead experiments and spectroscopic ellipsometry. The samples with both the oxygen and etch treatment had the highest number of beads on the InP surface and the lowest number of beads on the cover glass, and therefore we chose to give our photonic crystal membranes the same oxygen and etch treatment before incubation them with bBSA. From the contact angle measurements, we know that this results in relative hydrophilic surfaces.
The spectroscopic ellipsometry measurements show that a layer of bBSA is created on the treated InP surfaces but in order to make confident statements regarding the thickness of the adsorbed layer, more reference measurements are needed and more attention needs to be given to fitting the obtained spectra with the Cauchy model.

Chapter 5

Chemical sensing

This chapter will consider chemical sensing with PhC membrane cavities, which is the detection of changes in ambient refractive index from the resonance spectra. In the next chapter PhC membrane cavities will be incubated with solutions that contain proteins, therefore it is necessary to know whether a solution really fills the holes and the area underneath the membrane. This chapter will start by explaining the main parameters of refractive index sensing optical biosensors; the sensitivity, the filling fraction and the detection limit. Refractive index sensing is an area of interest for several groups all over the world, so we will start with a literature overview of what has already been done in this field. Next the systematic investigation of the sensitivity 80 PhC membrane cavities will be discussed. Part of the results in this chapter are also published in [111].

5.1 Sensors: basic working principles and definitions

The goal of this project is to detect changes in the ambient refractive index with photonic crystal membrane cavities, or to use the photonic crystal membrane cavities as a refractive index sensor, also called a refractometer. This is done by looking at the resonance spectra of the cavity, taken at different ambient refractive indices. The easiest experiment is to immerse the photonic crystal membrane in a liquid, for example water, as in Figure 5.10. Increasing the environmental refractive index causes the peaks in the resonance spectrum to shift towards the red. The wavelength λ of a peak divided by its full-width-at-half-maximum $\Delta\lambda_{FWHM}$ determines the quality factor Q of that cavity mode.

There are two important parameters that describe the sensor performance: the sensitivity and the detection limit of the sensor. The sensitivity is defined as the change in the transduction signal in response to biorecognition. The value of the sensitivity increases if the interaction between matter and light is increased. The detection limit is the smallest change in the transduction

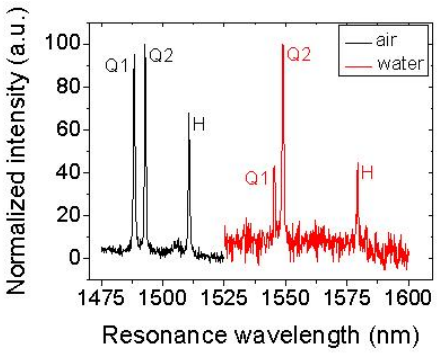

Figure 5.1: *The resonance spectra of a photonic crystal membrane cavity before and after water infiltration. Q1 and Q2 are the resonance peaks of the (nearly degenerate) quadrupole mode, and H is the hexapole mode of the cavity.*

signal that can be accurately obtained so it is determined by the noise of the transduction signal.

5.1.1 The sensitivity

The first important parameter of a refractive index sensor is its sensitivity S, defined as

$$S = \frac{\Delta\lambda}{\Delta n} \tag{5.1}$$

with $\Delta\lambda$ the shift in resonance wavelength and Δn the change in refractive index. The value of the sensitivity can be easily determined from resonance spectra like Figure 5.10. However, even though this definition is very practical to work with, it says not everything about the sensitivity of the cavity. The shift in resonant wavelength $\Delta\lambda$ and the change in refractive index Δn are also related by

$$\frac{\Delta\lambda}{\lambda} = f \cdot \frac{\Delta n}{n} \tag{5.2}$$

with f the filling fraction that quantifies the relative optical overlap of the mode with the air/liquid in the holes, therefore $0 \leq f \leq 1$ [112]. The wavelength λ is the free space resonance wavelength of the cavity and the refractive index n is the refractive index of the liquid. Using equation 5.2, equation 5.1 can be written as

$$S = f \cdot \frac{\lambda}{n} \leq \frac{\lambda}{n} \tag{5.3}$$

The theoretical maximum sensitivity S_{max} is thus defined as $\frac{\lambda}{n}$. This is a theoretical maximum, that can never be obtained in practice because a full overlap of the mode with the hole is impossible. However, the goal is to have a high sensitivity and this the highest value for f as is practically possible.

5.1.2 The detection limit

A second important parameter is the detection limit DL of a sensor. The detection limit is the smallest change in refractive index δn that the refractometer can still accurately detect. It is determined by the ratio of the smallest spectral shift $\delta\lambda$ that can be accurately detected, i.e. the sensor resolution, and the sensitivity. Roughly speaking $\delta\lambda$ might be set to be the resonance linewidth $\Delta\lambda_{FWHM} = \lambda/Q$. However, accurate fitting procedures may determine peak shifts with a resolution better than the linewidths of the peaks. The resolution is determined by three factors: the amplitude noise of the signal, fluctuations in temperature and the spectral resolution. The latter two can be neglected in to our experimental set-up (see next chapter) but the amplitude noise needs to be taken into account because the accuracy of fitting depends on the signal-to-noise ratio. The standard deviation of the resulting spectral variation is given by

$$\sigma_{\delta\lambda} = \frac{\Delta\lambda_{FWHM}}{4.5 \cdot (SNR^{0.25})} \tag{5.4}$$

with SNR the signal-to-noise ratio (not in dB but in numbers) [113].

The resolution is taken as three times the standard deviation of the noise of the system

$$R = \frac{3 \cdot \Delta\lambda_{FWHM}}{4.5 \cdot (SNR^{0.25})} \tag{5.5}$$

Therefore the detection limit can we written as

$$DL = \frac{R}{S} = \frac{3 \cdot \Delta\lambda_{FWHM}}{4.5 \cdot (SNR^{0.25}) \cdot S} \tag{5.6}$$

Using $Q = \lambda/\Delta\lambda$ this becomes

$$DL = \frac{3 \cdot \lambda}{4.5 \cdot (SNR^{0.25}) \cdot Q \cdot S} \tag{5.7}$$

All the variables in equation 5.7 can be obtained by comparing two resonance spectra as in Figure 5.10.

Interpreting equation 5.7, to obtain a sensor with a low detection limit one needs a large signal-to-noise ratio, a high sensitivity and a high quality factor.

5.1.3 Competing properties

Reference [114] shows that f and Q are two competing properties of photonic crystal membranes and they can not both be maximized. This can be

understood since maximizing f means maximizing the overlap of light with the holes which increases the losses and decreases Q. However, to maximize the sensitivity, f needs to be maximized. To solve the dilemma between maximizing S and Q, Tomljenovic-Hanic et al. introduced whet they call the figure of merit M, given by

$$M = f \cdot Q \tag{5.8}$$

For photonic crystal membrane nanocavities, this figure M needs to be optimized. The theoretical study of the figure of merit performed by Tomljenovic-Hanic et al. showed that to obtain the highest possible M, the quality factor needs to be optimized in spite of the negative effect this has on the filling factor.

5.2 Literature overview

In literature, lot of reports can be found on refractive index sensing with photonic crystal based devices. Examples are among others one dimensional PhCs [115], PhC fibers [116] and PhC waveguides [66] but the focus here will be on the literature of photonic crystal membrane cavities.

The group that was the first ever to publish their research on photonic crystal membrane cavities for refractive index sensing is the group of Scherer from the Californian Institute of Technology [71] in 2003. Over the years they have published several articles in which they optimize a modified H0 lasing cavity in InGaAsP membranes with quantum wells as active material [9]. From photoluminescence experiments during infiltrations with isopropanol and methanol they obtained sensitivity values up to 245 nm/RIU [9]. Shortly after, Grots group from Agilent Technologies reported on a similar H0 cavity in a silicon-on-insulator (SOI) based system [117]. This group had to use waveguides to excite their cavities and they obtained a sensitivity of ∼200 nm/RIU and a detection limit smaller than 10^{-3}.

The next report came in 2008 from the group of Baba, based on InGaAsP membranes with a quantum well. This group has been optimizing (lasing) $H0_{s\&r}$ cavities [48–50] and their highest experimental sensitivity is 400 nm/RIU [50]. Since these cavities lase, the spectral linewidth is very high (of the order of pm) so the detection limit will be well below 10^{-6}.

The group of Krauss have quoted a sensitivity value 1538 nm/RIU for their slotted double-heterostructures using SOI technology [68, 118]. They obtained these numbers by infiltrating their structures with solutions of caster sugar and deionized water. Care should be taken in interpreting these results since 1538 nm/RIU exceeds the theoretical maximum for λ ∼1600 nm and n ∼1.33 RIU. They explain this surprisingly high figure by an increase in

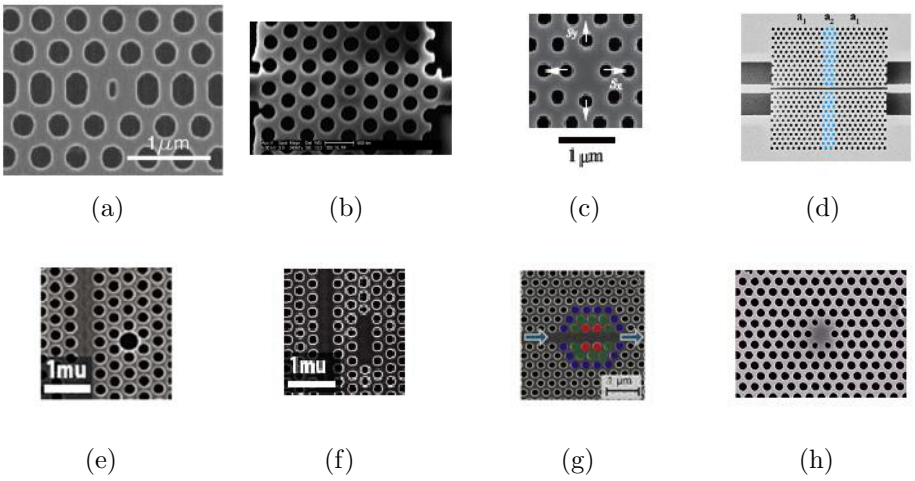

(a) (b) (c) (d)

(e) (f) (g) (h)

Figure 5.2: *SEM images of the cavity designs of the different groups (a) Scherer, (b) Grot, (c) Baba, (d) Krauss, (e)-(g) Finley, (h) Lee.*

wettability; increasing the concentration of caster sugar improves the wettability and therefore the penetration of the solution into the slots improves too and leads to large shifts ($\Delta\lambda = 18$ nm) for very small changes in refractive index ($\Delta n = 0.0117$). For a quality factor of 4000 and a sensitivity of 1538 nm/RIU this group obtains a detection limit of 7.8 10^{-6} RIU. However, because the sensitivity depends on a partial filling, it is not possible to calibrate this sensor. Finley et al. performed infiltrations with water and isopropanol for three types of cavities: a modified H0 cavity, a modified L3 cavity and a width modulated cavity which is a PhC waveguide in which several of the holes have a shift perpendicular to the waveguide orientation [119, 120]. They found sensitivity values of approximately 155, 65 and 105 nm/RIU respectively with corresponding detection limits of 0.018, 0.006 and 0.003 RIU.

The group of Lee et al. have quoted a sensitivity value of ∼50 nm/RIU for their microfluidic system based on an InP membrane with InAsP quantum wells with lasing $H1_{s\&r}$ cavities [8]. They state however that the InP surface is hydrophobic which is the reason their holes are only partially filled and the sensitivity is lower than expected.

5.3 Systematic investigation of the sensitivity

5.3.1 Experimental method

To look at the sensitivity of the PhC membrane nanocavities, they were infiltrated with Milli-Q water. The experimental method will be described before turning to the results. In Chapter 4 was seen that the InP substrates that received both the O_2 and H_3PO_4 treatment were the best for bBSA adsorption. For this reason the wafer that holds the InGaAsP PhC membrane nanocavities was given this very same treatment. Since the area on which the cavities are made is very small, it is sufficient to apply a droplet of water onto the surface for the infiltration experiments. However, because of the curvature of the droplet it could be that the laser light does not get to the cavity properly or that the collection of emitted light is distorted. Additionally, the absorption of light by water could be an issue.

To understand this issue, the penetration depth of light in water as a function of the wavelength was investigated. The penetration depth $\delta = 1/\alpha$, with α the absorption coefficient, is defined as the depth at which the intensity of light inside water drops to 1/e of its original value. From Figure 5.3 (a) can be seen that the penetration depth in water at the excitation wavelength (660 nm) is approximately 275 cm which causes no problems for our experiments. However, as Figures 5.3 (b) and (c) show, the emitted light with wavelengths between 1300 and 1600 nm has a penetration depth between 340 and 1500 μm [121]. The light can thus travel multiple times from one side of the cavity to the other, a distance of approximately 1 μm. However it does cause a problem for the collection of emitted light from the cavities since a droplet of water is several millimeters high.

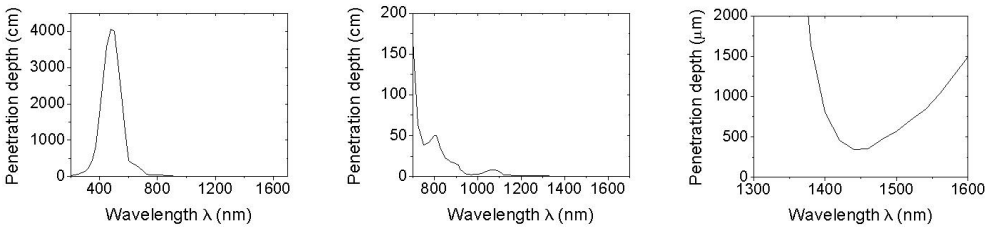

(a) (b) (c)

Figure 5.3: *The penetration depth of light in water for different wavelength ranges [121].*

To avoid these problems with the absorption of water, a thin cover glass (grade No.0 which corresponds to a thickness between 85 and 130 μm) was placed on top of the droplet and gently pushed it down as is shown in Figure 5.4 (d). Figures 5.4 (a) and (b) show that placing a cover glass on the

PhC membrane does not change the position of the resonance peaks (the differences are within the resolution limit), only the intensity of the collected light decreased slightly. Adding a water droplet shifts the resonance peaks towards the red, see Figure 5.4 (c). The resonance wavelengths and quality factors are determined from Lorentzian fits that give the values for λ and $\Delta\lambda$.

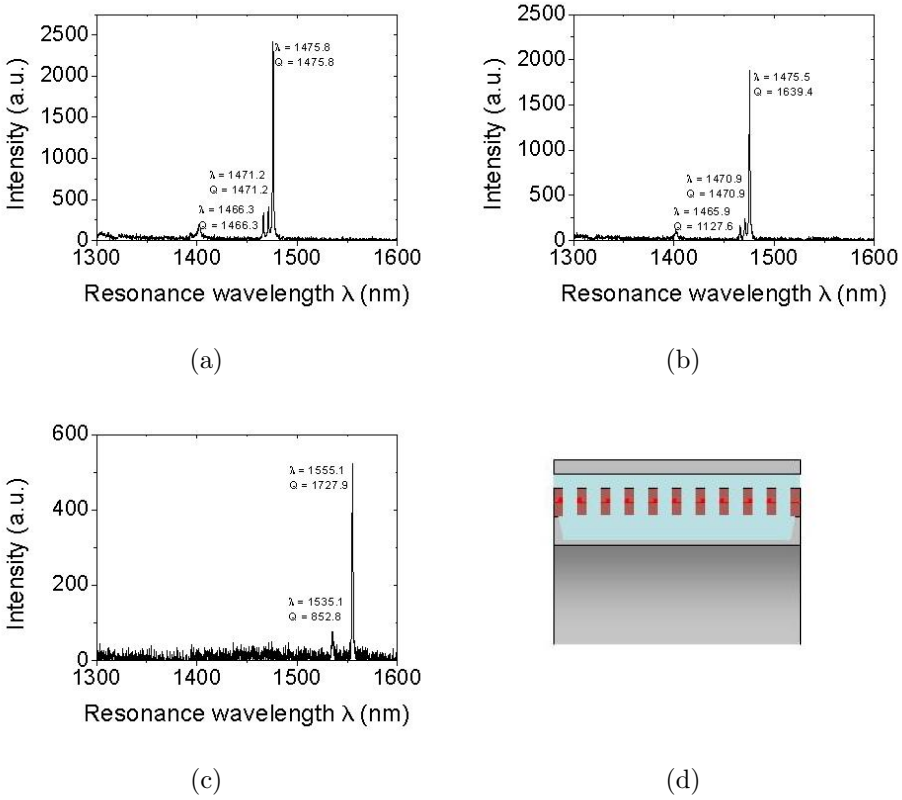

Figure 5.4: *The influence of a cover glass and a droplet of water on the PL spectrum of an $H1_{s\&r}$ cavity with parameters a = 511 nm, reduced radius 0.23a and shift 13 nm. The PL spectra are measured in (a) air, (b) air with a cover glass on top of the membrane, (c) water with a cover glass on top of the water layer and (d) a schematic representation of the infiltration (not drawn to scale).*

Because we slightly press down the cover glass is slightly pressed down, the thickness of the water layer. As is shown in Figure 5.4 (c) this layer is thin enough to allow the collection of light. Figure 5.4 shows that the intensity of the resonance peaks decreases in water but the noise stays the same for all three measurements. The quality factors increases when the cover glass is applied and a second time when water is applied. The shift from 1475.8 to 1639.4 corresponds to a decrease in spectral linewidth $\Delta\lambda_{FWHM}$ of 1.0 to 0.9 nm while the spectral linewidth stays 0.9 nm when going from 1636.4 to 1727.9, which means that the increase in Q is only caused by the increase in λ. The first increase in Q can maybe be explained by the fact that the average refractive index increases when the cover glass is applied which may reduce

the out-op-plane losses [122]. The decrease in collected signal points out that part of the emitted light is absorbed but we have no idea of the thickness of the water layer. To get an idea of the thickness, Beer-Lambert's law, which relates the intensity to the distance light travels through the material, i.e. the path length, was used. Beer-Lambert's law is given by

$$I(z) = I_0 \cdot e^{-\alpha z} \tag{5.9}$$

with I the intensity as function of the path length z, I_0 the intensity when no water is present and α the absorption coefficient of water which is wavelength dependent. The highest intensity in Figure 5.4 (b) is approximately 1900 which is taken as I_0 and this is at a wavelength of 1475.5 nm. By inserting these values in equation 5.9, together with α from [121], the graph of Beer-Lambert's law in Figure 5.5 is obtained. From Figure 5.4 (c) is seen that the collected intensity of the same mode for a water measurement decreases to about 530. Figure 5.5 shows that this corresponds to a penetration depth of approximately 60 μm. This means that the light travels a distance of 60 μm through water, meaning that the thickness of the water layer is 60 μm, which is smaller that the penetration depth.

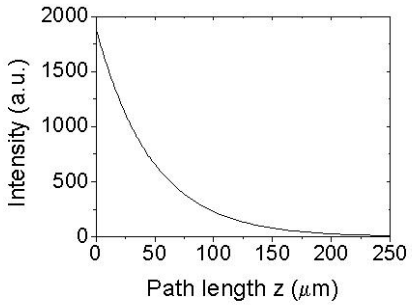

Figure 5.5: *Beer-Lambert's law for the water experiment of Figure 5.4. The loss in intensity that is observed corresponds to a path length of approximately 60 μm.*

Since the heterostructure designs did not give a PL spectrum we could work with, their sensitivity was not investigated. The sensitivity of the five point defect cavities was investigated systematically, irrespective of the variation of the quality factors with the different designs. Because the active III/V structure allows us to do fairly quick PL experiments, we are able to present the PL spectra of 80 cavities: 11 $H0_r$, 37 $H0_{s\&r}$, 12 $H1_r$, 11 $H1_{s\&r}$ and 9 L3 cavities.

A striking observation is that different measurements of the same cavity, give reproducible resonance spectra when a day or a few weeks are in between two measurements. Reproducible means that the observed variations in λ are within the resolution limit of our set-up. It is also known that the

temperature dependence of the cavities is 0.1 nm/°C [123] but this has no effect on the observed wavelengths since 0.1 nm is smaller than the resolution limit.

5.3.2 Design dependence

After infiltrating the PhC membrane cavities with water, the resonant wavelengths are red-shifted due to the increase in the ambient refractive index as was shown in Figure 5.4. When working with water, the change in refractive index $\Delta n = n_{water} - n_{air}$ is given by 0.3330. The sensitivities of the five designs are determined from these red-shifts with the definition of sensitivity $S = \Delta\lambda/\Delta n$. Sensitivities between 100 and 425 nm/RIU (refractive index unit) were observed. The maximum sensitivities for the five designs are shown in Table 5.1. They are among the highest reported in literature so far [8, 119], and compare favorably with cavities with central holes [124] or slots [68] made specifically to maximize sensitivity. The sensitivity is also defined as $S = f \cdot \lambda/n$ and the values for the thus obtained filling fractions f are also given in Table 5.1. Note that in practice, the filling fraction can never be close to 1, because then the light would not be confined anymore. Therefore we can not expect for the experiments to even get close to the maximum sensitivity. Table 5.1 shows filling fractions of ∼0.4 which already is a high value.

Table 5.1: *The maximum observed sensitivities.*

Cavity design	Sensitivity (nm/RIU)	Mode	Filling fraction
$H0_r$	390	dipole	0.38
$H0_{s\&r}$	390	SO dipole	0.38
$H1_r$	310	hexapole	0.29
$H1_{s\&r}$	425	hexapole	0.41
L3	110	A	0.10

The highest sensitivity was obtained for one of the $H1_{s\&r}$ cavities and the L3 cavities tend to have the lowest values. For an interpretation of these data, it is necessary to look in more detail to the variations with cavity designs and with the different modes of each design. This is done in the next paragraph.

5.3.3 Mode dependence

Besides being design dependent, the sensitivity also depends on the mode. In Figure 5.6 it is seen that the quadrupole peaks (Q1 and Q2) shift approximately 55 nm after water infiltration and the hexapole peak (H) 70 nm which results in sensitivities of 165 and 210 nm/RIU, respectively.

By looking back at equation 5.3, it can be seen that the maximum sensitivity is determined by the ratio of the resonance wavelength and the refractive index of water. For example, for the hexapole peak of Figure 5.6,

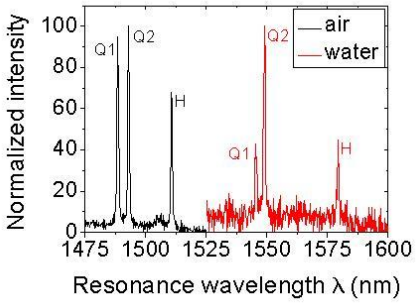

Figure 5.6: *The mode dependence of the sensitivity for a modified $H1_r$ cavity. The quadrupole peaks are denoted by Q1 and Q2, the hexapole peak by H.*

this is 1133 nm/RIU. By comparing this value with the sensitivity of 210 nm/RIU which was experimentally observed, it can be concluded that the filling fraction of this hexapole mode is approximately 20%. Additionally, the maximum sensitivity for the quadrupole peaks is 1120 nm/RIU and experimentally found a sensitivity of only 165 nm/RIU was found which results in a filling fraction of approximately 15%. The difference in sensitivity between the quadrupole modes and hexapole modes results from this 5% difference in hole filling fraction between the two modes. With the current software it is not possible to directly calculate the overlap of the electromagnetic field with the holes, i.e. f. Qualitatively however, this difference can be explained from Figure 3.11 which suggests that the electromagnetic field profile of the hexapole mode indeed has more overlap with the holes that the quadrupole modes.

In Table 5.2, for each mode of the five cavity designs the average measured sensitivity, corresponding average filling fraction and the theoretical maximum sensitivity was determined. The maximum observed sensitivities of Table 5.1 already have a filling fraction below 0.5 but the average observed sensitivities differ even more from their theoretical maximum values.

Table 5.2 shows a lot of important trends. First of all, as with the example of Figure 5.6, for each cavity type it can be understood why some modes have higher filling fractions than others. A stronger overlap of the electromagnetic field, i.e. a higher filling fraction, is generally obtained when going from monopole to dipole, quadrupole and hexapole. From the $H0_{s\&r}$ cavities is seen that higher order modes are more sensitive than first order modes. Higher order modes have a higher filling fraction since they are less confined to the dielectric. Furthermore the asymmetric monopole mode has a strong overlap with the holes (see Figure 3.7) and is therefore in this case slightly more sensitive than the asymmetric dipole mode.

Table 5.2: *The average observed sensitivities by mode.*

Cavity design	Mode	Average S (nm/RIU)	Maximum S (nm/RIU)	Average f
$H0_r$	dipole	308	1037	0.30
	monopole	262	1077	0.24
$H0_{s\&r}$	second order monopole	202	1035	0.20
	second order dipole	221	1051	0.21
	monopole	163	1100	0.15
	dipole	143	1121	0.13
$H1_r$	dipole	112	1124	0.10
	hexapole	258	1087	0.24
	quadrupole	193	1087	0.18
$H1_{s\&r}$	dipole	96	1055	0.08
	hexapole	284	1067	0.27
	quadrupole	191	1081	0.18
L3	mode A	86	1101	0.08

The second trend is that decreasing the size of the cavity ($H1_{s\&r} > H1_r > H0_{s\&r} > H0_r$) influences the filling fraction. Take for example the dipole mode that they all have, by decreasing the cavity, the average f increases from 0.08 to 0.30 which corresponds to an increase in sensitivity of about a factor of 3. This property is also seen for the monopole mode. For the hexapole mode f stays constant when going from $H1_{s\&r}$ to $H1_r$ the hexapole mode tends to be concentrated to the perimeter of the cavity and so is less dependent on the size. The filling fraction of the quadrupole mode even decreases for decreasing cavity size. A clear reason for this is not known.

5.3.4 Dependence of position in the band gap

The analysis of the sensitivities of 80 cavities shows an important trend that holds for all five designs but which will be first illustrated for the $H0_{s\&r}$ cavities since we have the most data for them. Figures 5.7 (a) and (b) show that the sensitivity scales as a function of the normalized frequency a/λ, irrespective of the lithographic parameters (lattice constant a, reduction r, shift s). The sensitivity increases when the cavity modes are lithographically tuned from the dielectric band ($a/\lambda = 0.29$) to the air band ($a/\lambda = 0.37$). The physical reason behind this phenomenon is again the overlap of the electromagnetic field with the holes. Recently, it was theoretically shown that modes closer to the air band have more overlap [114] and therefore they are more sensitive to the changes in refractive index inside the holes. This means that if the modes are lithographically tuned to be closer to the air band, their filling fraction and thus also their sensitivity are increased.

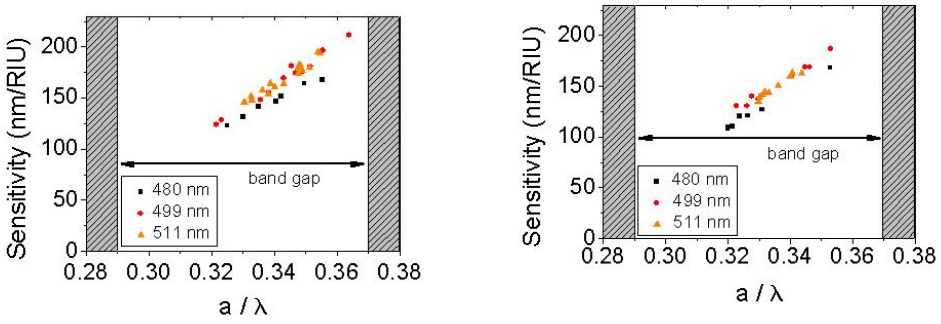

Figure 5.7: *The band gap dependency of the sensitivity for the modified $H0_{s\&r}$ cavities. Each data point represents a mode of a cavity with a different a, r and s. The band gap of the host photonic crystal goes from 0.29 to 0.37 a/λ, (a) the monopole mode and (b) the dipole mode.*

Notice that the observed modes do not go below $a/\lambda = 0.32$ which corresponds to a wavelength of approximately 1560 nm for a lattice constant of 500 nm. At this point, the sensitivity is still ∼150 nm/RIU which for a water infiltration results in a shift in resonance wavelength $\Delta\lambda$ of about 40 nm, yielding a resonance peak at $\lambda = 1600$ nm which is at the edge of what the spectrometer can detect. If $a/\lambda < 0.32$, the resonance peak will shift out of our detection range which is why there are no data point there.

Figures 5.8 (a) and (b), show that also for the $H0_r$ and $H1_r$ cavities the sensitivity can be lithographically tuned as a function of a/λ. However the $H0_r$ dipoles are found outside of the band gap and inside the air band ($a/\lambda > 0.37$). The reason these modes can exist inside the air band is because they still lay within the ΓK stop gap.

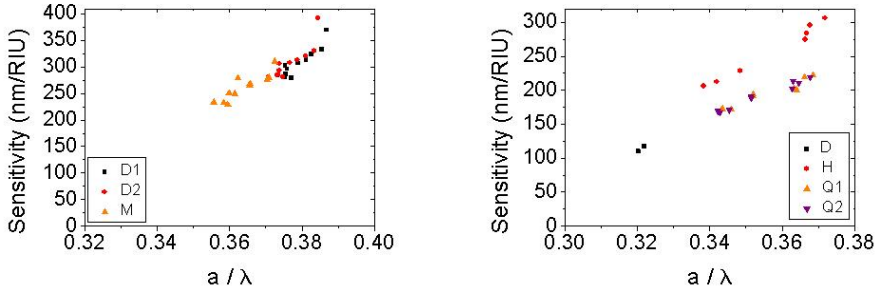

Figure 5.8: *The band gap dependency of the sensitivity for the modified (a) $H0_r$ and (b) $H1_r$ cavities.*

5.4 Investigation of the detection limit

5.4.1 Experimental method

To investigate the detection limit, only water infiltrations were performed, but also infiltrations with different sugar/water solutions. The same experimental method as in 5.3.1; a droplet and a cover glass were applied after which a PL experiment was done. The sugar/water solutions tha were used contained increasing concentrations of sugar (sucrose) which corresponds to an increasing refractive index of the solution as can be seen in Table 5.3.

Table 5.3: *The refractive indices for the different sugar/water solutions [125].*

Sugar concentration (% weight/weight)	Refractive index
0	1.3330
2.6	1.3367
6.0	1.3417
9.3	1.3467
12.5	1.3517
15.6	1.3567
18.7	1.3617

Between different infiltrations, the PhC membrane was rinsed with Milli-Q water and blown dry with N_2. Next a PL spectrum in air was taken and compared to a reference spectrum of the cavity, taken before the first infiltration. If the differences in resonance peak positions between the reference spectrum and this PL spectrum were within the resolution limit, the next infiltration was started.

5.4.2 The competition between S and Q

The detection limit is determined by the ratio of the resolution of the sensor and the sensitivity as was seen in paragraph 5.1. From equation 5.7 was seen that it was necessary to maximize the signal-to-noise ratio, the sensitivity and the quality factor to optimize (i.e. minimize) the detection limit. Furthermore, to optimize the figure of merit $M = f \cdot Q$, it was most important to maximize the quality factor instead of the filling fraction (and thus the sensitivity). This can be explained by looking at Figure 5.9 which shows that the sensitivity, again determined from water infiltrations, tends to decrease as the quality factor (measured in air) increases. However, at high Q's the decrease in S seems to become less. This inverse correlation between S and Q is again the result from the variation in overlap of the electromagnetic field with the holes, with other words, it is dependent on f. Cavities with a high Q have a strong confinement of the light to the dielectric material, whereas cavities with a high sensitivity have a strong overlap of the light with the

holes which means that they have higher losses and thus a lower Q.

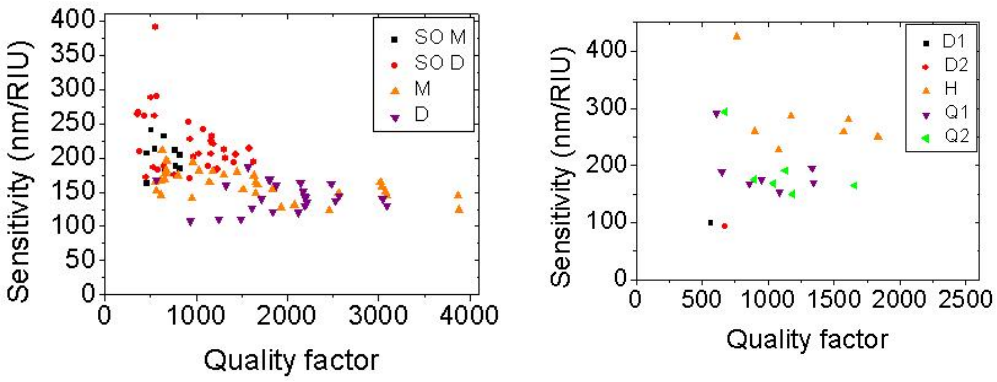

(a) (b)

Figure 5.9: *The sensitivity as a function of the quality factor for all modes of (a) a modified H0$_{s\&r}$ cavity, SO M stands for second order monopole, SO D for second order dipole, M for monopole and D for dipole and (b) modified H1$_{s\&r}$ cavity.*

This inverse correlation between S and Q poses a problem because we need to maximize both S and Q to minimize the detection limit. However, the inverse correlation is not linear. Figure 5.9 (a) shows that S can drop 200 nm/RIU while Q is increased to 4000 but the sensitivity of the monopole and dipole mode converge to a certain value, as well as the values of the hexapole and quadrupole modes. However, S is limited by a theoretic value of the order 10^3 while experimental Q values of 10^6 have been obtained [126] and theoretical predictions show that quality factors of 10^9 are possible [36]. Therefore to obtain the sensor with the lowest detection limit, first Q should be maximized and then look at how to maximize S at this maximum Q.

5.4.3 The detection limit

By doing infiltrations with the sugar/water solutions of Table 5.3, the detection limits of and H1$_{s\&r}$ and L3 cavity were investigated. The parameters of the H1$_{s\&r}$ cavity are $a = 511$ nm, $r = 0.23\,a$ and $s = 13$ nm, for the L3 cavity the parameters are $a = 511$ nm, $s = 25$ nm, $r = 0$. Figure 5.10 (a) shows that the (normalized) shape of the resonance peaks of the H1$_{s\&r}$ cavity does not change, the quality factor stays the same in air and in the sugar/water solutions (∼1500). For the sugar/water infiltrations of this H1$_{s\&r}$ cavity, red-shifts of about 1.2 nm are observed for an increase in refractive index of 0.005 RIU. This yields a sensitivity of approximately 240 nm/RIU and an estimated detection limit of approximately 0.001 RIU. This is not very low but it can be much improved by using cavities with lower spectral linewidths $\Delta\lambda_{FWHM}$. Both by decreasing the cavity linewidth to realistic (lasing) values of the order of tens of pm [49] and improving the signal-to-noise ratio,

detection limits of $\sim 10^{-6}$ and lower are well within reach. For the L3 cavities the sensitivities ($\sim$120 nm/RIU) and Q ($\sim$400) were too low to clearly differentiate between the peaks of different sugar water solutions since the detection limit for the L3 cavities was approximately 0.0075 RIU. Figure 5.10 (b) shows that when steps of 0.010 RIU are taken, one can distinguish the peaks in the L3 spectrum.

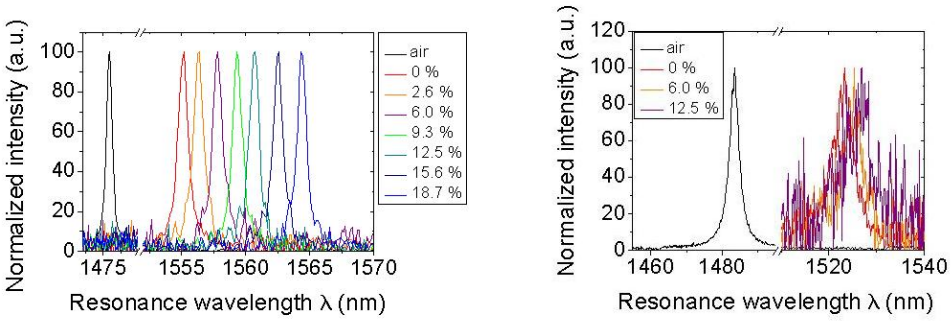

(a) (b)

Figure 5.10: *The PL spectra of (a) a modified $H1_{s\&r}$ cavity and (b) a modified L3 cavity after infiltration with different sugar/water solutions.*

5.4.4 Comparison with simulations

One of the reasons for doing these infiltration experiments is to see whether the holes are fully filled with the applied liquid. This is of importance for the protein adsorption in Chapter 6. To confirm full filling, the experimental results for the infiltration with different sugar/water solutions were compared to simulations. Three different scenarios were simulated; only liquid on top of the membrane surface, liquid on top of the membrane and in the holes and liquid on top of the membrane, in the holes and in the area underneath the membrane. These three possibilities are referred to as surface filling, surface-hole filling and total filling and are explained in Figure 5.11 (b). As is seen from Figure 5.11 (a), the experimental results closely resemble the total filling line. We can therefore conclude that we have total filling of the holes. Unlike Kim et al. or Di Falco et al. [8, 67], we do not suffer from air-pockets or high surface tension, respectively. Therefore every shift in wavelength only depends on the change in ambient refractive index and not on the good/worse infiltration.

Figure 5.11 also shows that the relation $\Delta\lambda/n$ is not linear since $\Delta\lambda$ increases more strongly for higher values of n. This second-order polynomial behavior of the form $\Delta\lambda = an^2 + bn + c$ was previously also observed by Chow et al. [117].

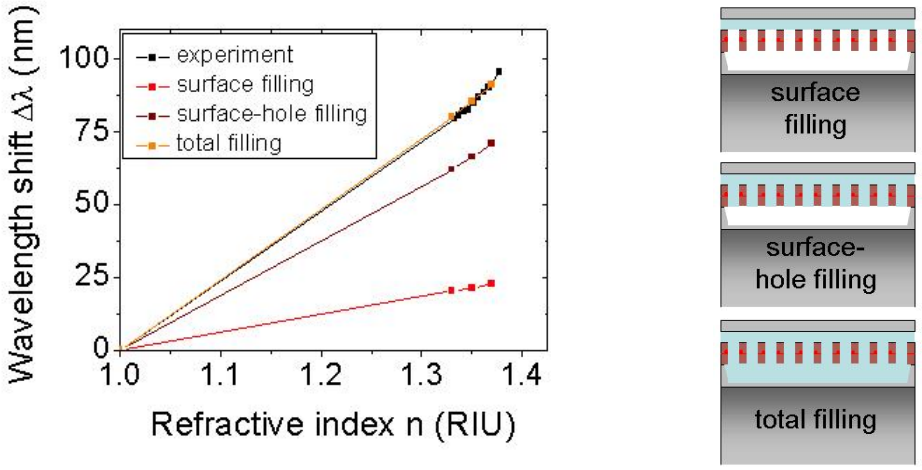

(a) (b)

Figure 5.11: *(a) The experimental and simulated resonance wavelengths of a modified $H1_{s\&r}$ cavity after infiltration with different sugar/water solutions and (b) a schematical representation of the different simulated situations (not drawn to scale).*

5.5 Conclusions

From this chapter, three important conclusions can be drawn. First of all, the small holes that form the photonic crystal can be infiltrated with a liquid. More importantly the holes and the area underneath the membrane are fully filled which means that the sensitivity is not influenced by changes in the filling of the holes. Therefore the sensitivity is only dependent on changes in the filling fraction. Different designs, modes and lithographic parameters result in different filling fractions and thus different sensitivities.

The second conclusion is that there is an inverse correlation between the sensitivity or filling factor and the quality factor. Increasing the filling factor implies increasing the spectral losses of the cavity and therefore decreasing the quality factor. However to maximize the detection limit one needs to maximize both the sensitivity and the quality factor. Since the theoretical maximum of the sensitivity is of the order of 10^3 and the highest experimental quality factors are currently of the order of 10^6, there is more room to optimize the quality factor than the sensitivity.

Last but not least, we can state that we have found sensitivities for all five designs that compare nicely to other literature values as is shown in Table 5.4. It should be said that for the sensitivity of the $H0_{s\&r}$ and $H1_{s\&r}$ cavities, the respective values of 390 and 425 nm/RIU are outliers. When discarding these values, the next maximum sensitivity values for these cavity designs are 290 and 285 nm/RIU respectively. The reason for these two outliers is currently

Table 5.4: *Overview of the sensitivities of PhC membrane cavities in literature.*

System	Design	S (nm/RIU)	DL (RIU)	Reference
InGaAsP QW	H0 laser	245	-	[71]
SOI	H0	200	$< 10^{-3}$	[46]
InGaAsP QW	$H0_{s\&r}$ laser	400	$< 10^{-6}$	[50]
SOI	slotted DHS	1538	-	[67]
SOI	H0	155	$18{\cdot}10^{-3}$	[119]
	L3	65	$6{\cdot}10^{-3}$	[119]
	WMC	105	$3{\cdot}10^{-3}$	[120]
InP/InAsP QW	$H1_{s\&r}$ laser	50	-	[8]
InGaAsP/InAs QD	$H0_r$	390	10^{-3}	[111]
	$H0_{s\&r}$	290/390	10^{-3}	[111]
	$H1_r$	310	10^{-3}	[111]
	$H1_{s\&r}$	285/425	10^{-3}	[111]
	L3	110	10^{-2}	[111]

not understood. A universal reading of the sensitivity with respect to the resonance position in the band gap is demonstrated. Additionally, a clear relation between sensitivity and cavity type and even cavity mode, has been established. These observation provide simple design guidelines for photonic crystal cavity sensors.

Chapter 6

Biosensing

For photonic crystal membrane nanocavities to become a viable candidate as refractive index sensing optical biosensors, the cavities need to be able to detect the change in refractive index that is induced when performing an immunoassay. This means that after creating arrays of PhC membrane nanocavities on a wafer, different antibodies would be attached to different cavities along the membrane after which a reference spectrum would be taken. When a sample containing antigens is then applied, binding between probe (antibody) and target (antigen) molecules will occur and the shift in resonance wavelength this gives can be detected.

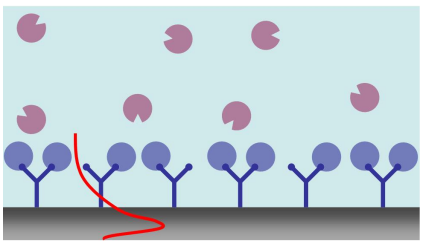

Figure 6.1: *Schematic representation of an immunoassay with a refractive index sensing optical biosensor (not drawn to scale).*

This chapter will first look at recent literature in the field of photonic crystal cavity based optical biosensors for protein detection. It will become clear that all groups use a BSA-based detection scheme to demonstrate the potential of their devices as a new optical biosensor platform. After the literature overview, a description of our experiments and a discussion of the results will be given.

6.1 Literature overview

The field of photonic crystals cavities as label-free optical detectors of proteins is very new since the first paper published on the topic dates back to only 2007 when Lee and Fauchet first described the functionalization of a

silicon photonic crystal microcavity for the detection of BSA and streptavidin [124]. After oxidizing and treating the oxidized silicon surface with amino-propyltrimethoxy-silane, they immobilized the probe molecules, the protein glutaraldehyde, which caused the resonance peak to shift 1.1 nm towards the red as is shown in Figure 6.2 (a). Next they applied the target molecules, BSA, which resulted in a second red shift of 1.7 nm. For the glutaraldehyde-BSA coupling, a detection limit of 2.5 fg was observed but this binding is non-specific. By using sulfo-NHS-LC-LC-biotin as probe molecule and streptavidin as target molecule, they demonstrated the specific binding capabilities of their structure. By comparing their results with simulated data, they concluded that the glutaraldehyde layer in their experiments was 7Å and their BSA layer was 10Å. Additionally, ellipsometry experiments were performed on a flat oxidized silica wafer to verify these thicknesses. The ellipsometry results indicated a glutaraldehyde layer thickness of 7 ± 1Å and a BSA layer thickness of 15 ± 5Å. The inconsistency in BSA layer thicknesses was never solved.

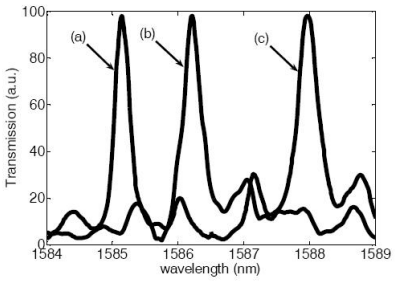

Figure 6.2: *(a) The resonance spectrum after oxidation and silanization, (b) the resonance spectrum after glutaraldehyde incubation and (c) the resonance spectrum after BSA binding [124].*

The next articles on the label-free detection with photonic crystal cavities are all from 2009. Dorfner et al. and Zlatanovic et al. both published articles on the shift in wavelength due to protein adsorption as a function of time on SOI based photonic crystal cavities [46, 120]. Dorfner et al. investigated H0, L3 and width-modulated cavities (see Figure 5.1 (e)-(g)) for which they found a BSA detection limit of 15.6 ± 2.9 fg, 4.5 ± 1.0 fg and 4.0 ± 0.6 fg, respectively. Zlatanovic et al. looked into a different H0 design and a different binding mechanism. They functionalized the surface with biotinylated BSA after which they applied the anti-biotin antibody as target molecule. The detection limit of anti-biotin was found to be smaller than 4.5 fg for this device.

Most recently, Kita et al. have reported on the binding of BSA to a glutaraldehyde-functionalized InGaAsP photonic crystal membrane surface [51]. Their $H0_{s\&r}$ cavities showed an average blue shift of the resonance peaks of 0.8 nm after glutaraldehyde incubation, which they state is possibly due to gluratic acid etching the membrane, and an average red shift of 1.2 nm for BSA binding.

However there is substantial spreading of the experimentally observed wavelength shifts; for glutaraldehyde, $\Delta\lambda$ between -1.7 and 0.7 nm were observed and for BSA values between 0.4 and 2.4 nm.

6.2 Detection of the binding of proteins

6.2.1 Experimental method

We chose to work with biotinylated BSA as probe molecule and streptavidin as target molecule. This choice is motivated by the fact that BSA has good surface coverage abilities and the fact that the biotin-streptavidin bond is one of the strongest non-covalent interactions in nature.

The PhC membrane cavities were given a treatment with O_2 and H_3PO_4 (see Chapter 4), which caused the resonance peaks to shift between 10 and 15 nm towards the blue, depending on design and mode. An example of this is shown in Figure 6.3 for an $H1_{s\&r}$. The resonance spectrum that was taken after the treatment was taken as a reference. The biotinylated BSA (bBSA) molecules were bound to the membrane surface during either a one-hour or a twenty-hour incubation period at 4°C. The buffer solution containing the bBSA was a 0.14 citrate buffer with pH 6.8 (Pierce Biotechnology). The membrane was then rinsed with Milli-Q water and blown dry with N_2, after which a second resonance spectrum was taken to investigate the binding of bBSA, see Figure 6.4. During an incubation period of one hour, the target molecules streptavidin (Pierce Biotechnology) were bound to the biotin molecules. The streptavidin buffer solution was a 20 mM potassium phosphate buffer with pH 6.5. Again, the membrane was rinsed in Milli-Q water and blown dry with N_2 before a third spectrum was taken as is shown in Figure 6.4.

Three cavities of each design ($H0_r$, $H0_{s\&r}$, $H1_r$, $H1_{s\&r}$ and L3) were investigated. For each design, the three cavities that had the highest sensitivities for the chemical sensing of the previous chapter were chosen. The incubations with bBSA of 1 and 20 hours were done on two different samples but for cavities with the same lithographic parameters.

6.2.2 Results

For a bBSA incubation time of 1 hour, Figure 6.4 shows the response of the cavities to the adsorption of proteins for an $H1_r$ cavity with parameters $a = 530$ nm and $r = 0.22a$. The hexapole mode in the reference spectrum is located at 1381.1 nm, and experiences a red shift of 0. nm for bBSA incubation and a blue shift of 0.6 nm for streptavidin incubation. The peaks corresponding to the quadrupole modes were found at 1404.2 and 1410.6 nm

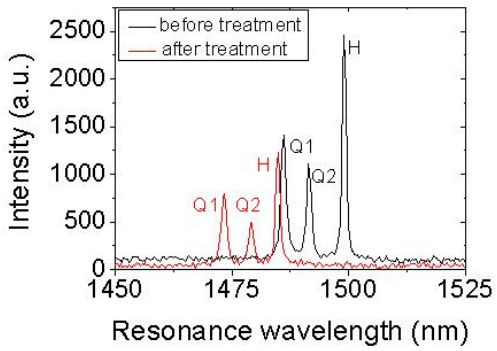

Figure 6.3: *The blue shifts due to the to O_2 and H_3PO_4 treatment on the InGaAsP PhC membrane nanocavities for an $H1_{s\&r}$ cavity with parameters $a = 518$ nm, $r = 0.23a$ and $s = 12$ nm. Q1 and Q2 are the quadrupole modes and H is the hexapole mode and their respective blue shifts are 12.8, 12.4 and 14.2 nm.*

in the reference spectrum. For bBSA incubation, a red shift of 0.4 and 0.3 nm was obtained, while for the streptavidin incubation a blue shift of 0.6 and 0.5 nm was seen. Note that compared to figure 6.3, the hexapole mode has changed position from being on the right of the quadrupole mode to being on the left in Figure 6.4. As can be seen in Figure 3.10, in most cases the hexapole mode lies on the right hand side of the quadrupole mode but it is also possible for the hexapole mode to be on the left hand side of the quadrupole mode.

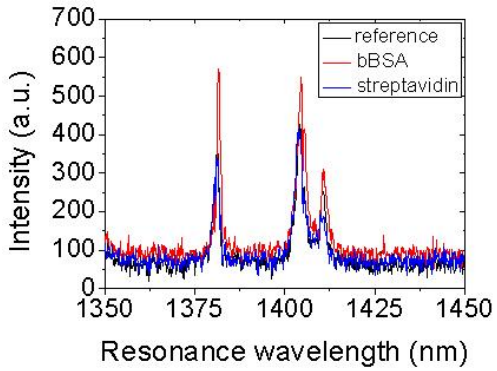

Figure 6.4: *An example of the change in resonance spectra with a one hour incubation of bBSA and streptavidin.*

All fifteen investigated cavities gave a small red shift after bBSA incubation with an average value of 0.4 nm as is shown in Figure 6.5. From simulations was expected that these values would be around 5 nm. This could mean that we do not have a full surface coverage of the cavity holes. After incubation with streptavidin, a red shift that is similar to the one due to bBSA is expected but Figure 6.5 (a) shows that on average, the resonance peaks have a

blue shift of 0.2 nm instead of a red shift. It is possible that the streptavidin buffer, which is slightly acidic, etches the membrane during that hour, canceling out the effect of streptavidin molecules binding to the biotin molecules.

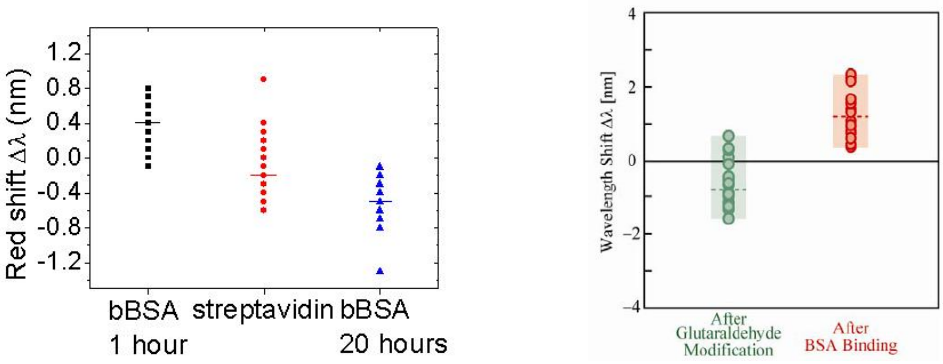

(a) (b)

Figure 6.5: *(a) The red shifts due to adsorption of bBSA to the InGaAsP and due to the binding of streptavidin to biotin and (b) the red shifts due to adsorption of glutaraldehyde and BSA [51].*

Our results are compared with the results of Kita et al. [51] in Figure 6.5 and it can be seen that both the graphs have a similar spread in $\Delta\lambda$. However, the graph from Kita et al. investigated the reproducibility in $\Delta\lambda$ of the same cavity while our data was obtained from different types of cavities and different modes. This means that for Kita et al., the spread in $\Delta\lambda$ shows the difference in protein adsorption between different experiments, but this is not necessarily the case for our results. Therefore, the shifts of Figure 6.5 (a) were normalized with the sensitivity values obtained for these cavities in Chapter 4. Figure 6.6 shows Δn, or $\Delta\lambda$/S, for each of the incubation steps. The average shifts in refractive index for one hour bBSA, streptavidin and twenty hours bBSA are 0.0017 $\pm$ 0.0009, -0.0007 $\pm$ 0.0025 and -0.003 $\pm$ 0.002, respectively. For each of the binding steps, a large spread in Δn is observed, indicating that also our red shifts $\Delta\lambda$ are caused by an unequal protein binding.

For a bBSA incubation time of 20 hours, Figure 6.7 shows the PL spectra of the same $H1_r$ cavity as before. By comparing Figures 6.4 and 6.7, it can be seen that the reference spectra for these two cavities with identical design parameters are not the same. This shows that even though two cavities are theoretically the same, the fabrication process for both cavities differs slightly which gives them different resonance wavelengths (see also Chapter 3).

Figure 6.7 shows that both the hexapole as the quadrupole resonance wavelengths shift towards the blue for this long incubation lime. For the other 14

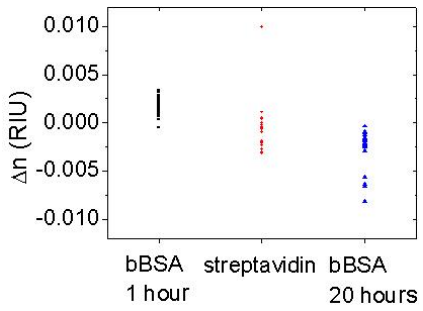

Figure 6.6: *The shifts in refractive index due to adsorption of bBSA to the InGaAsP and due to the binding of streptavidin to biotin.*

cavities, the same blue shift was observed when the bBSA incubation time was increase to 20 hours. The values ranged between 0.1 and 1.3 nm with an average of 0.5 nm as is seen from Figure 6.5 (a). As with the streptavidin buffer, the blue shift could be the result of the buffer etching the membrane due to the increased incubation time.

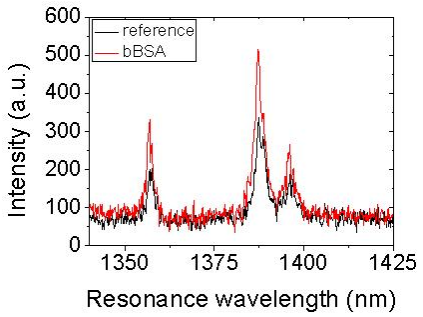

Figure 6.7: *An example of the change in resonance spectra with a twenty hours incubation time of bBSA. The hexapole peak shifts 0.3 nm towards the blue and the quadrupole peaks 0.5 and 0.2 nm.*

6.2.3 Conclusions

It was shown that the binding of proteins to the InGaAsP photonic crystal membrane cavities is possible and detectable but further work is needed to optimize the binding steps size a large spread in Δn was found. The effect of buffer solutions to the InGaAsP membrane should be removed if one wants to say with certainty that the observed shifts are solely due to the binding of proteins to the membrane or to the probe molecules. However, our results compare favorably with the results of other groups as is shown in Figure 6.5 (b). It can be concluded that determining which buffer solution to use is not a trivial problem and a thorough investigation is necessary.

Conclusions

Of the seven photonic crystal membrane cavity designs created, the heterostructure-based designs did not operate as expected. Therefore only the point defect cavities were investigated for their sensitivity. Because experiments with streptavidin-coated beads showed that biotinylated bovine serum albumin bound best to InP wafers that had received an oxygen and etch treatment, the InGaAsP samples were given these treatments too before incubation.

Spectroscopic ellipsometry experiments were performed to determine the thickness of the layer biotinylated bovine serum albumin but the results were not completely trustworthy; further spectroscopic ellipsometry measurements are necessary. The contact angle measurements showed that treated InP wafers were hydrophilic, which is why other than recent reports in literature, we did not have any problems infiltrating the photonic crystal holes. Because the simulated and experimental data points for the infiltrations coincided, the sensitivity values were found to be only dependent on the ambient refractive index and on the position of the mode inside the band gap of the photonic crystal. The observed sensitivities are among the highest reported in literature while the quality factor can be further increased to obtain lower detection limits.

Furthermore, it was shown that photonic crystal membrane nanocavities can be functionalized with probe molecules. It was not possible to detect the subsequent incubation with target molecules since the buffer solution containing the target molecules most likely etched the membrane. Further investigation is necessary to detect which buffer solutions are best used in combination with InGaAsP membranes. Alternatively, the use of linker molecules could be explored.

This report has shown that InGaAsP photonic crystal membrane nanocavities with embedded quantum dots are a promising platform for next generation optical biosensors. Furthermore, it was shown which parameters need to be considered when designing photonic crystal membrane nanocavities for sensing applications.

Appendix

The following tables give an overview of the current status of refractive index sensing optical biosensors. In each table, the detection limits of different designs of the same technological platform are compared.

For a refractive index based label-free optical biosensor the detection limit can be expressed in different units. First of all, it can be expressed in refractive index units (RIU) which is used when detecting a change in refractive index due to a change of bulk solution. The corresponding value is used to compare the performance of different sensors from the same or another platforms. When proteins are detected, other units are used. Either the detection limit is expressed in pg/mm^2, which corresponds to the surface mass density, or in ng/mL which corresponds to the sample concentration. Unlike the unit RIU, these units depend on the affinity of the target molecule to the bio-recognition molecule so one needs to specify to which biomolecule the value corresponds to.

When viruses or bacteria are detected, the detection limit units are pfu/mL or cfu/mL, respectively. The unit pfu stand for plaque-forming unit and is defined as the number of viruses that form a plaque, where a plaque is an area of cells that appear darker than other cells under a microscope. The unit cfu stands for colony forming unit. In a culture, each individual bacteria will start to multiply and form a colony. Each of these colonies is visible with the naked eye so they can be counted.

The detection limits of various optical biosensors categorized by technology platform: surface plasmon resonance in Table 6.1, interferometry in Table 6.2, waveguides in Table 6.5, ring resonators in Table 6.3, optical fibers in Table 6.4 and photonic crystals in Table 6.6.

Table 6.1: *Detection limits of various surface plasmon resonator (SPR) based optical sensors [127].*

Optical structure	Analyte	Detection limit	Reference
SPR	Bulk solution	10^{-5}-10^{-8} RIU	[130]-[135]
Long range SPR	Bulk solution	10^{-7}-10^{-8} RIU	[136, 137]
SPR	Bulk solution	10^{-5}-10^{-7} RIU	[138, 141]
Imaging SPR	Protein	1 nM	[142]
Optical heterodyne SPR	Protein	0.2 nM	[143]
Phase sensitive SPR	Protein	1.3 nM	[144]
Wavelength modulated SPR	DNA	10 pM	[145]
Imaging SPR	DNA and RNA	10 nM	[146]
Flow injection SPR	DNA	54 fM	[148]
		1.38 fM	[148]
Angle modulated SPR	Protein	0.15 ng/mL	[149]
SPR	Protein	66.7 unit/mL	[150]
SPR	Protein	50 ng/mL	[151]
Prism based SPR	Bacteria	10^6 cfu/mL	[152]
		100 cfu/mL	[153]
BIAcore 2000 SPR	Bacteria	25 cfu/mL	[154]

Table 6.2: *Detection limits of various interferometry (IF) based optical sensors [127].*

Optical structure	Analyte	Detection limit	Reference
Mach-Zehnder IF	Bulk solution	10^{-7} RIU	[155]
	Protein	20 pg/mm^2	[156]
Young's IF	Bulk solution	$\sim 10^{-7}$ RIU	[157, 158]
	Virus	1000 particles/mL	[159]
Hartman IF	DNA	4 ng/mL	[160]
	Protein	5 ng/mL	[160]
		0.1 ng/mL	[161]
	Virus	10^7 pfu/mL	[160]
	Bacteria	$5 \cdot 10^8$ cfu/mL	[160]
		$5 \cdot 10^5$ cfu/mL	[160]
Backscattering IF	Protein	fM	[162]
	Protein	pM	[163]

Table 6.3: *Detection limits of various ring resonator based optical sensors [127].*

Optical structure	Analyte	Detection limit	Reference
Ring on a chip	Bulk solution	10^{-4}-10^{-7} RIU	[30, 164–166]
	DNA	$\sim$ 100 nM	[167]
	Protein	250 pg/mm^2	[164]
		20	[169]
		0.1 nM	[168]
	Bacteria	10^5 cfu/mL	[167]
Dielectric microsphere	Bulk solution	10^{-7} RIU	[170]
	DNA	1 pg/mm^2	[171]
	Protein	10 pg/mL	[172]
		1 unit/mL	[173]
	Virus	$\sim$ 1 pg/mm^2	[174]
	Bacteria	100 cfu/mm^2	[175]
Capillary opto-	Bulk solution	10^{-6}-10^{-7} RIU	[176]
fluidic ring	DNA	4 pg/mm^2	[177]
		10 pM	[177]
	Protein	$\sim$ 1 pg/mm^2	[178]
		3 pM	[178]
	Virus	1000 particles/mL	[179]

Table 6.4: *Detection limits of various optical fiber based optical sensors [127].*

Optical structure	Analyte	Detection limit	Reference
Fiber Bragg grating	Bulk solution	$\sim 10^{-6}$ RIU	[180–185]
	DNA	0.7 μg/mL	[185]
		0.1 μM	[185]
Long period grating	Bulk solution	10^{-4} RIU	[186]
	Protein	2 μg/mL	[187]
Nanofiber	Bulk solution	10^{-7} RIU	[188]
Fiber coupler	Bulk solution	$4 \cdot 10^{-6}$ RIU	[189]
	Protein	0.5 μg/mL	[189]
Fiber Fabry-Perot	Bulk solution	10^{-5} RIU	[190, 191]
cavity	DNA	76 μM	[192]
		1.7 ng	[192]
	Protein	25 μg/mL	[193]

Table 6.5: *Detection limits of various waveguide (WG) based optical sensors [127].*

Optical structure	Analyte	Detection limit	Reference
Resonant mirror	Protein	~ 0.1 pg/mm^2	[194]
	Cell	10^6 cells/mL	[195]
Metal-clad WG	Bacterial spore	$\sim 10^5$ spores/mL	[196]
	Cell	~ 10 cells/mL	[197]
Reverse symmetry WG	Cell	60 cells/mm^2	[198]
Symmetrical metal-clad WG	Bulk solution	$2 \cdot 10^{-7}$	[199]

Table 6.6: *Detection limits of various photonic crystal based optical sensors [127].*

Optical structure	Analyte	Detection limit	Reference
2D PhC	Bulk solution	$\sim 10^{-5}$ RIU	[200, 201]
	Protein	0.4 pg/mm^2	[200, 201]
2D PhC Microcavity	Bulk solution	$\sim 10^{-3}$ RIU	[71, 117]
	Protein	1 fg	[124]
PhC waveguide	Protein	0.15 μM	[202]
1D PhC microcavity array	Bulk solution	$7 \cdot 10^{-5}$ RIU	[203]
PhC fiber	Bulk solution	10^{-4} RIU	[204]

Acknowledgments

A lot of people have contributed in some way to my master project and I would like to take the time to thank them. First of all, I would like to thank Rob van der Heijden and Leo van IJzendoorn for creating this project. It was the first time the groups Photonics and Semiconductor Nanophysics (PSN) and Molecular Biosensors for Medical Diagnostics (MBx) collaborated on a master project and I have enjoyed both worlds. I would like to thank both of them for this opportunity and for their guidance during this year. Furthermore, I would like to thank Rob for daily motivating me and for suggesting to submit an abstract for the IEEE Photonics Benelux Symposium. To both our surprise, I was given the opportunity to present my results and put the TU/e on the photonic crystal biosensor map.

I want to thank Mehmet Dündar for sharing this knowledge of photonic crystal membrane nanocavities, for preparing my samples and for showing us what real Turkish food is like. I wish you good luck in finishing your PhD. Thank you to Xander Janssen and Asha Jacob from MBx for teaching me how to work with BSA, beads and the inverted microscope.

The PSN group is a very warm and social group. I really enjoyed my time here, for which I want to thank all of you. A special thanks to Margriet van Doorne for her kind and motivating words and for making sure everything went smoothly. To Harm Kicken, we had a nice time sharing the office and I wish you all the best in your new job.

I also would like to thank my parents, family and friends for believing in me and supporting me. And last but not least, I would like to thank Jan Wera. Together we started this adventure in Eindhoven and faced all its challenges. Now that we are both graduated and our story here in the Netherlands comes to an end, we have a lot of memories to take back with us. And of course, our new adventure will start very soon.

Bibliography

[1] W.E. Moerner, *Single-molecule Chemistry and Biology Special Feature: New directions in single-molecule imaging and analysis*, Proc. Natl. Acad. Sci. **104** 12596-12602 (2007).

[2] D. Erickson, S. Mandal, A.H.J. Yang and B. Cordovez, *Nanobiosensors: optofluidic, electrical and mechanical approaches to biomolecular detection at the nanoscale*, Microfluid. Nanofuid. **4** 33-52 (2008).

[3] M.A. Cooper, *Optical biosensors: where next and how soon?*, Drug Discovery Today **11** 1061-1067 (2006).

[4] D. Psaltis, S.R. Quake and C. Yang, *Developing optofluidic technology through the fusion of microfluidics and optics*, Nature **442** 381-386 (2006).

[5] C. Monat, P. Domachuk and B.J. Eggleton, *Integrating optofluidics: A new river of light*, Nat. Photon. **1** 106-114 (2007).

[6] F.S. Ligler, *Perspective on Optical Biosensors and Integrated Sensor Systems*, Anal. Chem. **81** 519-526 (2009).

[7] J.A. Rogers and R.G. Nuzzo, *Recent progress in soft lithography*, Materials Today **8** 50-56 (2005).

[8] S.-H. Kim, J.-H. Choi, S.-K. Lee, S.-H. Kim, S.-M. Yang, Y.-H. Lee, C. Seassal, P. Regrency and P. Viktorovitch, *Optofluidic integration of a photonic crystal nanolaser*, Opt. Express **16** 6515-6527 (2008).

[9] M. Adams, G.A. DeRose, M. Lončar and A. Scherer, *Lithograpically fabricated optical cavities for refractive index sensing*, J. Vac. Sci. Technol. B **23** 3168-3173 (2005).

[10] M.L. Adams, Marko Lončar, A. Scherer and Yueming Qiu, *Microfluidic Integration of Porous Photonic Crystal Nanolasers for Chemical Sensing*, IEEE Journal On Selected Areas in Communications **23** 1348-1354 (2005).

[11] M.L. Adams, *Integration of Optoelectronics and Microfluidics for Biological and Chemical sensing*, master thesis California Institute of Technology (2004).

[12] R. Narayanaswamy and O.S. Wolfbeis, *Optical Sensors*, (Springer New York, 2004).

[13] C.D. Chin, V. Linder and S.K. Sia, *Lab-on-a-chip devices for global health: Past studies and future opportunities*, Lab Chip **7** 4157 (2007).

[14] S.Y. Yurish, N.V. Kirianaki and I.L. Mushkin, *World Sensors and MEMS Markets: Analysis and Trends*, Sens. Transducers **62** 456-461 (2005).

[15] K.R. Rogers, *Recent advances in biosensor techniques for environmental monitoring*, Anal. Chim. Acta **568** 222231 (2006).

[16] S. Rodriguez-Mozaz, M.J. López de Alda, M.-P. Marco and D. Barceló, *Biosensors for environmental monitoring, A global perspective*, Talanta **65** 291297 (2005).

[17] J.D. Joannopoulos, S.G. Johnson, J.N. Winn and R.D. Meade, *Photonic crystals - Molding the flow of light, second edition*, (Princeton University Press, 2008).

[18] J.W.S. Rayleigh, *On the remarkable phenomenon of crystalline reflexion described by Prof. Stokes*, Phil. Mag. **26** 256-265 (1888).

[19] E. Yablonovitch, *Inhibited Spontaneous Emission in Solid-State Physics and Electronics*, Phys. Rev. Lett. **58** 2059 (1987).

[20] S. John, *Strong Localization of Photons in Certain Disordered Dielectric Superlattices*, Phys. Rev. Lett. **58** 2486 (1987).

[21] E. Yablonovitch, T.J. Gmitter and K.M. Leung, *Photonic Band Structure: The Face-Centered-Cubic Case Employing Nonspherical Atoms*, Phys. Rev. Lett **67** 2295-2298 (1991).

[22] K.M. Ho, C.T. Chan, C.M. Soukoulis, R. Biswas and M. Sigalas, *Photonic band gaps in three dimensions: New layer-by-layer periodic structures*, Solid State Commun. **89** 413-416 (1994).

[23] T.F. Krauss, R.M. De La Rue and S. Brand, *Two-dimensional photonic-bandgap structures operating at near-infrared wavelengths*, Nature **383**, 699-702 (1996).

[24] S. Noda, K. Tomoda, N. Yamamoto and A. Chutinan, *Full Three-Dimensional Photonic Bandgap Crystals at Near-Infrared Wavelengths*, Science **289** 604-606 (2000).

[25] K. Sakoda, *Optical Properties of Photonic Crystals, second edition*, (Springer-Verlag Berlin Heidelberg, 2005).

[26] B.E.A. Saleh and M.C. Teich, *Fundamentals of Photonics* (John Wiley & Sons, Inc., 2005).

[27] C. Kittel, *Introduction to Solid State Physics, 8th ediction* (John Wiley & Sons, Inc., 1991).

[28] V.R. Almeida, Q. Xu, C.A. Barrios and M. Lipson, *Guiding and confining light in void nanostructure*, Opt. Lett. **29** 1209-1211 (2004).

[29] Q. Zu, V.R. Almeida, R.R. Panepucci and M. Lipson, *Experimental demonstration of guiding and confining light in nanometer-size low-refractive-index material*, Opt. Lett. **29** 1626-1628 (2004).

[30] C.A. Barrios, M.J. Bañuls, V. González-Pedro, K.B. Gylfason, B. Sánchez, A. Maquieira, H. Sohlström, M. Holgado and R. Casquel, *Label-free optical biosensing with slot-waveguides*, Opt. Lett. **33** 708-710 (2008).

[31] A. Di Falco, L. O'Faolain and T.F. Krauss, *Photonic crystal slotted slab waveguide*, Photonics Nanostruct. Fundam. Appl. **6** 38-41 (2008).

[32] A. Di Falco, L. O'Faolain and T.F. Krauss, *Dispersion control and slow light in slotted photonic crystal waveguides*, Appl. Phys. Lett. **92** 083501 (2008).

[33] S.-H. Kwon, T. Sünner, M. Kamp and A. Forchel, *Optimization of photonic crystal cavity for chemical sensing*, Opt. Express **16** 11709-11717 (2008).

[34] T. Yamamoto, M. Notomi, H. Taniyama, E. Kuramochi, Y. Yoshikawa, Y. Tori and T. Kuga, *Design of a high-Q air-slot cavity based on a width-modulated line-defect in a photonic crystal slab*, Opt. Express **16** 13809-13817 (2008).

[35] T.F. Krauss, *Photonic crystals: Cavities without leaks*, Nat. Mater. **2** 777-778 (2003).

[36] Y. Tanaka, T. Asano and S. Noda, *Design of Photonic Crystal Nanocavity With Q-Factor of* $\sim 10^9$, J. Lightwave Technol. **26** 1532-1539 (2008).

[37] S. Noda, *Progress and Future Prospects of Two- and Three-Dimensional Photonic Crystals*, J. Lightwave Technol. **24** 4554-4567 (2006).

[38] O. Painter, R.K. Lee, A. Scherer, A. Yariv, J.D. O'Brien, P.D. Dapkus and I. Kim, *Two-Dimensional Photonic Band-Gap Defect Mode Laser*, Science **284** 1819-1821 (1999).

[39] S. Anantathanasarn, R. Nötzel, P.J. van Veldhoven, T.J. Eijkemans and J. H. Wolter, *Wavelength-tunable (1.55-μm region) InAs quantum dots in InGaAsP/InP (100) grown by metal-organic vapor-phase epitaxy*, J. Appl. Phys. **98** 013503 (2005).

[40] D. Zhou, S. Anantathanasarn, P.J. van Veldhoven, F.W.M. van Otten, T.J. Eijkemans, T. de Vries, E. Smalbrugge and R. Nötzel, *Lateral wavelength control of InAs/InGaAsP/InP (100) quantum dots in the 1.55 μm region by selective-area metal organic vapor-phase epitaxy*, J. Appl. Phys. **100** 113512 (2006).

[41] A. Mock and J. OBrien, *Direct extraction of large quality factors and resonant frequencies from Padé interpolated resonance spectra*, Opt. Quant. Electron. **40** 11871192 (2008).

[42] K.S. Yee, *Numerical Solution of Initial Boundary Value Problems Involving Maxwell's Equations in Isotropic Media*, IEEE Trans. Antennas Propag. **14** 302-307 (1966).

[43] A. Taflove and S.C. Hagness, *Computational Electrodynamics: The Finite-Difference Time-Domain Method, second edition*, (Artech House Inc., 2000).

[44] G.H. Olsen, T.Z. Zamerowski, R.T. Smith and E.P. Bertin, *InGaAsP quaternary alloys: Composition, refractive index and lattice mismatch*, J. Electron. Mater. **9** 977-987 (1980).

[45] G.W. Burr, E. Chow, L.W. Mirkarimi, M.M. Sigalas and A. Grot, *Photonic Crystal Microcavities as Ultracompact Film-Thickness Monitors for Biosensing*, in Integrated Photonics Research and Applications/Nanophotonics for Information Systems, Technical Digest, Optical Society of America, paper NThC4 (2005).

[46] S. Zlatanovic, L.W. Mirkarimi, M.M. Sigalas, M.A. Bynum, E. Chow, K.M. Robotti, G.W. Burr, S. Esener and A. Grot, *Photonic crystal microcavity sensor for ultracompact monitoring of reaction kinetics and protein concentration*, Sens. Actuators B **141** 13-19 (2009).

[47] US patent *Photonic crystal sensors*, inventors: A. Grot, K.-C. Chow, L.W. Mirkarimi, M.M. Sigalas, assignee: Agilent Technologies Inc., patent number: 7489846, issue date: 10 Feb 2009, application number: 10/799,020.

[48] K. Nozaki and T. Baba, *Laser characteristics with ultimate-small modal volume in photonic crystal slab point-shift nanolasers*, Appl. Phys. Lett. **88** 211101 (2006).

[49] S. Kita, K. Nozaki and T. Baba, *Refractive index sensing utilizing a cw photonic crystal nanolaser and its array configuration*, Opt. Express **16** 8174-8180 (2008).

[50] S. Kita, K. Nozaki and T. Baba, *Refractive Index Sensing Utilizing CW Photonic Crystal Nanolaser and Its Arrayed Configuration*, in Conference on Lasers and Electro-Optics/Quantum Electronics and Laser Science Conference and Photonic Applications Systems Technologies, OSA Technical Digest, Optical Society of America, paper CMO6 (2008).

[51] S. Kita, Y. Nishijima, H. Misawa and T. Baba, *Label-Free Biosensing Utilizing Ultrasmall Photonic Crystal Nanolaser*, in Integrated Photonics and Nanophotonics Research and Applications, OSA Technical Digest, Optical Society of America, paper IMB3 (2009).

[52] J. Huh, J.-K. Hwang, H.-Y. Ryu and Y.-H. Lee, *Nondegenerate monopole mode of single defect two-dimensional triangular photonic band-gap cavity*, J. Appl. Phys. **92** 654-659 (2002).

[53] M. Shirane, S. Kono, J. Ushida, S. Ohkouchi, N. Ikeda, Y. Sugimoto and A. Tomita, *Mode identification of high-quality-factor single-defect nanocavities in quantum dot-embedded photonic crystals*, J. Appl. Phys. **101** 073107 (2007).

[54] D. Dalacu, S. Frédérick, J. Lapointe, P.J. Poole, G.C. Aers and R.L. Williams, *Modified single missing air-hole defects in InAs/InP quantum dot membrane photonic crystal microcavities*, J. Vac. Sci. Technol. A **24** 791-796 (2006).

[55] H.-Y. Ryu, M. Notomi, Y.-H. Lee, *High-quality-factor and small-mode-volume hexapole modes in photonic-crystal-slab nanocavities*, Appl. Phys. Lett. **83** 4294-4296 (2003).

[56] S. Chakravarty, P. Bhattacharya, S. Chakrabarti and Z. Mi, *Multiwavelength ultralow-threshold lasing in quantum dot photonic crystal microcavities*, Opt. Lett. **32** 1296-1298 (2007).

[57] A.R.A. Chalcrafta, S. Lam, D. O'Brien, T.F. Krauss, M. Sahin, D. Szymanski, D. Sanvitto, R. Oulton, M.S. Skolnick, A.M. Fox, D.M. Whittaker, H.-Y. Liu and M. Hopkinson, *Mode structure of the L3 photonic crystal cavity*, Appl. Phys. Lett. **90** 241117 (2007).

[58] S. Chakravarty, J. Topol'ancik, P. Bhattacharya, S. Chakrabarti, Y. Kang and M.E. Meyerhoff, *Photonic Crystal Microcavity Source based Ion Sensor*, Photonic Crystals and Photonic Crystal Fibers for Sensing Applications, Proceedings of the SPIE **6005** 746-749 (2005).

[59] A. Mock, L. Lu and J.D. O'Brien, *Spectral properties of photonic crystal double heterostructure resonant cavities*, Opt. Express **16** 9391-9397 (2008).

[60] B.-S. Song, S. Noda, T. Asano and Y. Akahane, *Ultra-high-Q photonic double-heterostructure nanocavity*, Nat. Mater. **4** 207 - 210 (2005).

[61] R. Herrmann, T. Sünner, T. Hein, A. Löffler, M. Kamp and A. Forchel, *Ultrahigh-quality photonic crystal cavity in GaAs*, Opt. Lett. **31** 1229-1231 (2006).

[62] A. Mock, L. Lu, E.H. Hwang, J. O'Brien and P.D. Dapkus, *Modal Analysis of Photonic Crystal Double-Heterostructure Laser Cavities*, IEEE J. Sel. Top. Quant. **15** 892-900 (2009).

[63] S.G. Johnson, P.R. Villeneuve, S. Fan and J.D. Joannopoulos, *Linear waveguides in photonic-crystal slabs*, Phys. Rev. B **62** 8212-8222 (2000).

[64] S. Tomljenovic-Hanic, C.M. de Sterke and M.J. Steel, *Design of high-Q cavities in photonic crystal slab heterostructures by air-holes infiltration*, Opt. Express **14** 12451-12456 (2006).

[65] T. Sünner, T. Stichel, S.-H. Kwon, T.W. Schlereth, S. Höfling, M. Kamp and A. Forchel, *Photonic crystal cavity based gas sensor*, Appl. Phys. Lett. **92** 261112 (2008).

[66] J. Topol'ancik, P. Bhattacharya, J. Sabarinathan and P.-C. Yu, *Fluid detection with photonic crystal-based multichannel waveguides*, Appl. Phys. Lett. **82** 1143-1145 (2003).

[67] A. Di Falco, L. O'Faolain and T.F. Krauss, *Slotted Photonic Crystal Waveguides and Cavities*, in Integrated Photonics and Nanophotonics Research and Applications, Optical Society of America, paper IMD2 (2008).

[68] A. Di Falco, L. O'Faolain and T.F. Krauss, *Chemical sensing in slotted photonic crystal heterostructure cavities*, Appl. Phys. Lett. **94** 063503 (2009).

[69] J. Gao, X. Yang, C.W. Wong, W.M.J. Green, Y. Vlasov and S. Assefa. *Demonstrations of an air-slot photonic crystal nanocavity with ultrasmall mode volumes for enhanced light-matter interactions*, in Conference on Lasers and Electro-Optics/Quantum Electronics and Laser Science Conference and Photonic Applications Systems Technologies, OSA Technical Digest, Optical Society of America, paper CFE5 (2009).

[70] S. Xiao and N.A. Mortensen, *Proposal of highly sensitive optofluidic sensors based on dispersive photonic crystal waveguides*, J. Opt. A **9** S463-467 (2007).

[71] M. Lončar, A. Scherer and Y. Qiu, *Photonic crystal laser sources for chemical detection*, Appl. Phys. Lett. **82** 4648-4650 (2003).

[72] D.A.Puelo and R. Bizios, *Biological Interactions on Materials Surface*, (Springer, 2009).

[73] K.C. Dee, D.A. Puleo and R. Bizios, *An Introduction To Tissue-Biomaterial Interactions*, (John Wiley & Sons Inc., 2002).

[74] http://en.wikipedia.org/wiki/Amino_acid.

[75] M.M. Browne, G.V. Lubarsky, M.R. Davidson and R.H. Bradley, *Protein adsorption onto polystyrene surfaces studied by XPS and AFM*, Surf. Sci. **553** 155-167 (2004).

[76] http://www.bio.miami.edu/~cmallery/150/protein/alpha-helix.jpg

[77] http://andromeda.rutgers.edu/~huskey/images/beta_sheet1_w.gif

[78] http://www.bio.miami.edu/~cmallery/150/gene/sf14x14.jpg

[79] http://biochemistryquestions.wordpress.com/2008/10/09/supersecondary-structures-motifs-and-domains/

[80] W.L. Hughes, In *The Proteins* (H. Neurath and K. Biley, Academic Press, 1954).

[81] T. Peters, *Serum Albumin*, Adv. Protein Chem. **37** 161-245 (1985).

[82] O.J.M. Bos, J.F.A. Labro, M.J.E. Fischer, J. Witling and L.H.M. Janssen, *The molecular mechanism of the Neutral-to-Base Transition of Human Serum Albumin*, J. Biol. Chem. **264** 953-959 (1989).

[83] J.R. Brown, *Structure of Bovine serum albumin*, Fed. Proc. **34** 591 (1975).

[84] D.C. Carter and J.X. Ho, *Structure of Serum Albumin*, Adv. Protein Chem. **45** 153-203 (1994).

[85] http://www.iob.uio.no/forskning/celler/teknikk/IH-bakgrunn.html

[86] P.C. Weber, D.H. Ohlendorf, J.J. Wendoloski and F.R. Salemme, *Structural Origins of High-Affinity Biotin Binding to Streptavidin*, Science **243** 85-88 (1989).

[87] B. Swerydo-Krawiec, H. Devaraj, G. Jacob and J.J. Hickman, *A new interpretation of Serum Albumin Surface Passivation*, Langmuir **20** 2054-2056 (2004).

[88] S.R. Whaley, D.S. English, E.L. Hu, P.F. Barbara and A.M. Belcher, *Selection of peptides with semiconductor binding specificity for directed nanocrystal assembly*, Nature **405** 665-668 (2000).

[89] J.R. Long, N. Oyler, G.P. Drobny and P.S. Stayton, *Assembly of α-helical Peptide Coatings on Hydrophobic Surfaces*, J. Am. Chem. Soc. **124** 6297-6303 (2002).

[90] L. Shi, V. De Paoli, N. Rosenzweig and Z. Rosenzweig, *Synthesis and Application of Quantum Dots FRET-Based Protease Sensors*, J. Am. Chem. Soc. **128** 1037810379 (2006).

[91] H.H. Park and A. Ivanisevic, *Formation and Characterization of Homogenous and Mixed Self-Assembled Monolayers of Peptides and Alkanethiols on Indium Phosphide surfaces*, J. Phys. Chem. C **111** 3710-3718 (2007).

[92] E. Estephan, M.-B. Saab, C. Larroque, M. Martin, F. Olsson, S. Lourdudoss and C. Gergely, *Peptides for functionalization of InP semiconductors* J. Colloid. Interface. Sci. **337** 358-363 (2009).

[93] H.P. Wampler and A. Ivanisevic, *Nanoindentation of gold nanoparticles functionalized with proteins*, Micron **40** 444-448 (2009).

[94] F. Seker, K. Meeker, T.F. Kuech and A.B. Ellis, *Surface Chemistry of Prototypical Bulk II-VI and III-V Semiconductors and Implications for Chemical Sensing*, Chem. Rev. **100** 2505-2536 (2000).

[95] M. Losurdo, S.D. Wolter, M.M. Griangregorio, F. Losco, M. Angelo, W.V. Lampert, G. Bruno and A. Brown, *Interplay between surface chemistry and optical behavior of semiconductor-biomolecule functionalized sensing systems: an optical investigation by spectroscopic ellipsometry*, Mater. Res. Soc. Symph. Proc. **1133** AA07-13 (2009).

[96] H. Urano and S. Fukuzaki, *Influence of Anionic Compounds on Adsorption Behavior of Bovine Serum Albumin at Oxide-Water Interfaces*, J. Ferment. Bioeng. **82** 261-266 (1997).

[97] K. Goede, P. Busch and M. Grundmann, *Binding Specificity of a Peptide on Semiconductor Surfaces*, Nano Lett. **4** 2115-2120 (2004).

[98] K. Adlkofer and M. Tanaka, *Stable Surface Coating of Gallium Arsenide with Octadecylthiol Monolayers*, Langmuir **14** 4267-4273 (2001).

[99] C. Krichner, M. George, B. Stein, W.J. Parak, H.E. Gaub and M. Seitz, *Corrosion Protection and Long-Term Chemical Functionalization of Gallium Arsenide in an Aqueous Environment*, Adv. Funct. Mater. **12** 266276 (2002).

[100] M. Schvartzman, V. Sidorov, D. Ritter and Y. Paz, *Surface passivation of (100) InP by organic thiols and polyimide as characterized by steady-state photoluminescence*, Semicond. Sci. Technol. **16** L68-L71 (2001).

[101] M. Schvartzman, V. Sidorov, D. Ritter and Y. Paza, *Passivation of InP surfaces of electronic devices by organothiolated self-assembled monolayers*, J. Vac. Sci. Technol. B **21** 148-155 (2003).

[102] H.A. Budz and R.R. LaPierrea, *Properties of octadecanethiol self-assembled monolayers deposited on GaAs from liquid and vapor phases*, J. Vac. Sci. Technol. A **26** 1425-1431 (2008).

[103] H.A. Budz, M.C. Biesinger and R.R. LaPierrea, *Passivation of GaAs by octadecanethiol self-assembled monolayers deposited from liquid and vapor phases*, J. Vac. Sci. Technol. B **27** 1425-1431 (2009).

[104] S.J. McClellan and E.I Franses, *Adsorption of bovine serum albumin at solid/aqueous interfaces*, Colloids Surf. A Physicochem. Eng. Asp. **260** 265-275 (2005).

[105] H. Fujiwara, *Spectroscopic Ellipsometry: Principles and Applications*, (John Wiley & Sons Inc., 2003).

[106] D. Gonçalves and E.A. Irene, *Fundamentals and applications of spectroscopic ellipsometry*, Quim. Nova **25** 794-800 (2002).

[107] H. Arwin, *Spectroscopic ellipsometry and biology: recent developments and challenges*, Thin Solid Films **313** 764-774 (1998).

[108] H. Arwin, *Ellipsometry on thin organic layers of biological interest: characterization and applications*, Thin Solid Films **337** 48-56 (2000).

[109] A. Tsargorodskaya, A.V. Nabok and A.K. Ray, *Ellipsometric study of the adsorption of bovine serum albumin into porous silicon*, Nanotechnology **15** 703709 (2004).

[110] L.M. Karlsson, M. Schubert, N. Ashkenov and H. Arwin, *Protein adsorption in porous silicon gradients monitored by spatially-resolved spectroscopic ellipsommetry*, Thin Solid Films **455** 726-730 (2004).

[111] E.C.I. Ryckebosch, M.A. Dündar, R. Nötzel, F. Karouta, L.J. van IJzendoorn and R.W. van der Heijden, *Refractive index sensing with an InGaAsP photonic crystal membrane cavity by means of photoluminescence*, Proceedings of the 2009 Annual Symposium of the IEEE Photonics Benelux Chapter 45-48 (2009).

[112] N.A. Mortensen, S. Ziao and J. Pedersen, *Liquid-infiltrated photonic crystals: enhanced light-matter interactions for lab-on-a-chip applications*, Microfluid. Nanofluid. **4** 117-127 (2007).

[113] I.M. White and X. Fan, *On the performance quantification of resonant refractive index sensors*, Opt. Express **16** 1020-1028 (2006).

[114] S. Tomljenovic-Hanic, A. Rahmani, M.J. Steel and C.M. de Sterke, *Comparison of the sensitivity of air and dielectric modes in photonic crystal slab sensors*, Opt. Express **17** 14552-14557 (2009).

[115] G. Barillaro, S. Merlo and L.M. Strambini, *Optical characterization of alcohol-infiltrated one-dimensional silicon photonic crystals*, Opt. Lett. **34** 12 (2009).

[116] S.-G. Li, S.-Y. Liu, Z.-Y. Song, Y. Han, T.-L. Cheng, G.-Y. Zhou and L.-T. Hou, *Study of the sensitivity of gas sensing by use of index-guiding photonic crystal fibers*, Appl. Opt. **46** 22 (2007).

[117] E. Chow, A. Grot, L. W. Mirkarimi, M. Sigalas and G. Girolami, *Ultra-compact biochemical sensor built with two-dimensional photonic crystal microcavity*, Opt. Lett. **29** 1093-1095 (2004).

[118] A. Di Falco, L. O'Faolain and T.F. Krauss, *Slotted photonic crystal waveguides and cavities for slow light and sensing applications*, 5th IEEE International Conference on Group IV Photonics 228-230 (2008).

[119] D.F. Dorfner, T. Hürlimann , T. Zabel, L.H. Frandsen, G. Abstreiter and J.J. Finley, *Photonic crystal nanostructures for refractive index sensing*, Appl. Phys. Lett. **93** 181103 (2008).

[120] D. Dorfner, T. Zabel, T. Hürlimann, N. Hauke, L. Frandsen, U. Rant, G. Abstreiter and J. Finley, *Photonic crystal nanostructures for optical biosensing applications*, Biosens. Bioelectron. **24** 3688-3692 (2009).

[121] G.M. Hale and M.R. Querry, *Optical constants of water in the 200 nm to 200 μm wavelength region*, Appl. Opt. **12** 555-563 (1973).

[122] F. Intonti, S. Vignolini, F. Riboli, M. Zani, D.S. Wiesma, L. Balet, L.H. Li, M. Francardi, A. Gerardino, A. Fiore and M. Gurioli, *Tuning of photonic crystal cavities by controlled removal of locally infiltrated water*, Appl, Phys. Lett. **95** 173112 (2009).

[123] B. Wild, R. Ferrini, R. Houdré, M. Mulot, S. Anand and C.J.M. Smith, *Temperature tuning of the optical properties of planar photonic crystal microcavities*, Appl. Phys. Lett. **84** 846-848 (2004).

[124] M.R. Lee and P.M. Fauchet, *Two-dimensional silicon photonic crystal based biosensing platform for protein detection*, Opt. Express **15** 4530-4535 (2007).

[125] F. Schneider, *Sugar Analysis-ICUMSA*, (International Commission for Uniform Methods of Sugar Analysis, 1979).

[126] B.-S. Song, T. Asano and S. Noda, *Heterostructures in two-dimensional photonic-crystal slabs and their application to nanocavities*, J. Phys. D **40** 2629-2634 (2007).

[127] X. Fan, I.M. White, S.I. Shopova, H. Zhy, J.D. Suter, Y. Sun, *Sensitive optical biosensors for unlabeled targets: A review*, Anal. Chim. Acta **620** 8-26 (2008).

[128] `http://www.virapur.com/?page_id=41`

[129] `http://en.wikipedia.org/wiki/Colony-forming_unit`

[130] N.J. Tao, S. Boussaad, W.L. Huang, R.A. Arechabaleta and J. D'Agnese, *High resolution surface plasmon resonance spectroscopy*, Rev. Sci. Instrum. **70** 4656-4660 (1999).

[131] R. Slavík, J. Homola and J. Čtyroký, *Single-mode optical fiber surface plasmon resonance sensor*, Sens. Actuators B Chem. **54** 74-79 (1999).

[132] D. Monzón-Hernández and J. Villatoro, *High-resolution refractive index sensing by means of a multiple-peak surface plasmon resonance optical fiber sensor*, Sens. Actuators B Chem. **115** 227-231 (2006).

[133] A. Suzuki, J. Kondoh, Y. Matsui, S. Shiokawa and K. Suzuki, *Development of novel optical waveguide surface plasmon resonance (SPR) sensor with dual light emitting diodes*, Sens. Actuators B Chem. **106** 383-387 (2005).

[134] F.C. Chien, C.Y. Lin, J.N. Yih, K.L. Lee, C.W. Chang, P.K. Wei, C.C. Sun and S.J. Chen, *Coupled waveguidesurface plasmon resonance biosensor with subwavelength grating*, Biosens. Bioelectron. **22** 2737-2742 (2007).

[135] J. Dostálek, J. Homola and M. Miler, *Rich information format surface plasmon resonance biosensor based on array of diffraction gratings*, Sens. Actuators B Chem. **107** 154-161 (2005).

[136] G.G. Nenninger, P. Tobiška, J. Homola and S.S. Yee, *Long-range surface plasmons for high-resolution surface plasmon resonance sensors*, Sens. Actuators B Chem. **74** 145-151 (2001).

[137] R. Slavík and J. Homola, *Ultrahigh resolution long range surface plasmon-based sensor*, Sens. Actuators B Chem. **123** 10-12 (2007).

[138] J.S. Shumaker-Parry and C.T. Campbell, *Quantitative Methods for Spatially Resolved Adsorption/Desorption Measurements in Real Time by Surface Plasmon Resonance Microscopy*, Anal. Chem. **76** 907-917 (2004).

[139] A. Zybin, C. Grunwald, V.M. Mirsky, J. Kuhlmann, O.S. Wolfbeis and K. Niemax, *Double-Wavelength Technique for Surface Plasmon Resonance Measurements: Basic Concept and Applications for Single Sensors and Two-Dimensional Sensor Arrays*, Anal. Chem. **77** 2393-2399 (2005).

[140] M. Piliarik, H. Vaisocherová and J. Homola, *A new surface plasmon resonance sensor for high-throughput screening applications*, Biosens. Bioelectron. **20** 2104-2110 (2005).

[141] T.M. Chinowsky, M.S. Grow, K.S. Johnston, K. Nelson, T. Edwards, E. Fu and P. Yager, *Compact, high performance surface plasmon resonance imaging system*, Biosens. Bioelectron. **22** 2208-2215 (2007).

[142] H.J. Lee, D. Nedelkov and R.M. Corn, *Surface Plasmon Resonance Imaging Measurements of Antibody Arrays for the Multiplexed Detection of Low Molecular Weight Protein Biomarkers*, Anal. Chem. **78** 6504-6510 (2006).

[143] W.-C. Kuo, C. Chou and H.-T. Wu, *Optical heterodyne surface-plasmon resonance biosensor*, Opt. Lett. **28** 1329-1331 (2003).

[144] W.-C. Law, P. Markowicz, K.-T. Yong, I. Roy, A. Baev, S. Patskovsky, A.V. Kabashin, H.-P. Ho and P.N. Prasad, *Wide dynamic range phase-sensitive surface plasmon resonance biosensor based on measuring the modulation harmonics*, Biosens. Bioelectron. **23** 627-632 (2007).

[145] L. He, M.D. Musick, S.R. Nicewarner, F.G. Salinas, S.J. Benkovic, M.J. Natan and C.D. Keating, *Colloidal Au-Enhanced Surface Plasmon Resonance for Ultrasensitive Detection of DNA Hybridization*, J. Am. Chem. Soc. **122** 9071-9077 (2000).

[146] B.P. Nelson, T.E. Grimsrud, M.R. Liles, R.M. Goodman and R.M. Corn, *Surface Plasmon Resonance Imaging Measurements of DNA and RNA Hybridization Adsorption onto DNA Microarrays*, Anal. Chem. **73** 1-7 (2001).

[147] F. Song, F. Zhou, J. Wang, N. Tao, J. Lin, R.L. Vellanowth, Y. Morquecho and J.W. Laidman, *Detection of oligonucleotide hybridization at femtomolar level and sequence-specific gene analysis of the Arabidopsis thaliana leaf extract with an ultrasensitive surface plasmon resonance spectrometer*, Nucleic Acids Res. **30** 14 (2002).

[148] X. Yao, X. Li, F. Toledo, C.Z. Lopez, M. Gutova, J. Momand and F. Zhou, *Sub-attomole oligonucleotide and p53 cDNA determinations via a high-resolution surface plasmon resonance combined with oligonucleotide-capped gold nanoparticle signal amplification*, Anal. Biochem. **354** 220-228 (2006).

[149] G.A.J. Besselink, R.P.H. Kooyman, P.J.H.J. van Os, G.H.M. Engbers and R.B.M. Schasfoorta, *Signal amplification on planar and gel-type sensor surfaces in surface plasmon resonance-based detection of prostate-specific antigen*, Anal. Biochem. **333** 165-173 (2004).

[150] J.W. Chung, R. Bernhardt and J.C. Pyun, *Additive assay of cancer marker CA 19-9 by SPR biosensor*, Sens. Actuators B Chem. **118** 28-32 (2006).

[151] Y. Teramura and H. Iwata, *Label-free immunosensing for ?-fetoprotein in human plasma using surface plasmon resonance*, Anal. Biochem. **365** 201-207 (2007).

[152] A.D. Taylor, Q. Yu, S. Chen, J. Homola and S. Jiang, *Comparison of E. coli O157:H7 preparation methods used for detection with surface plasmon resonance sensor*, Sens. Actuators B Chem. **107** 202-208 (2005).

[153] B.-K. Oh, Y.-K. Kim, K.W. Park, W.H. Lee and J.-W. Choi, *Surface plasmon resonance immunosensor for the detection of Salmonella typhimurium*, Biosens. Bioelectron. **19** 1497-1504 (2004).

[154] J.W. Waswa, C. Debroy and J. Irudayaraj, *Rapid Detection of SAalmonella Enteritidis and Escherichia Coli Using Surface Plasmon Resonance Biosensor*, J. Food Process Eng. **29** 373-385 (2006).

[155] R.G. Heideman and P.V. Lambeck, *Remote opto-chemical sensing with extreme sensitivity: design, fabrication and performance of a pigtailed integrated optical phase-modulated MachZehnder interferometer system*, Sens. Actuators B Chem. **61** 100-127 (1999).

[156] M. Weisser, G. Tovar, S. Mittler-Neher, W. Knoll, F. Brosinger, H. Freimuth, M. Lacher and W. Ehrfeld, *Specific bio-recognition reactions observed with an integrated MachZehnder interferometer*, Biosens. Bioelectron. **14** 405-411 (1999).

[157] A. Brandenburg, *Differential refractometry by an integrated-optical Young interferometer*, Sens. Actuators B Chem. **39** 266-271 (1997).

[158] A. Ymeti, J.S. Kanger, J. Greve, P.V. Lambeck, R. Wijn and R.G. Heideman, *Realization of a multichannel integrated Young interferometer chemical sensor*, Appl. Opt. **42** 5649-5660 (2003).

[159] A. Ymeti, J. Greve, P.V. Lambeck, T. Wink, S.W.F.M. van Hovell, T.A.M. Beumer, R.R. Wijn, R.G. Heideman, V. Subramaniam and J.S. Kanger, *Fast, Ultrasensitive Virus Detection Using a Young Interferometer Sensor*, Nano Lett. **7** 394-397 (2007).

[160] B.H. Schneider, J.G. Edwards and N.F. Hartman, *Hartman interferometer: versatile integrated optic sensor for label-free, real-time quantification of nucleic acids, proteins and pathogens*, Clin. Chem. **43** 1757-1763 (1997).

[161] B.H. Schneider, E.L. Dickinson, M.D. Vach, J.V. Hoijer and L.V. Howard, *Highly sensitive optical chip immunoassays in human serum*, Biosens. Bioelectron. **15** 13-22 (2000).

[162] D.A. Markov, K. Swinney and D.J. Bornhop, *Label-Free Molecular Interaction Determinations with Nanoscale Interferometry*, J. Am. Chem. Soc. **126** 16659-16664 (2004).

[163] D.J. Bornhop, J.C. Latham, A. Kussrow, D.A. Markov, R.D. Jones and H.S. Sorensen, *Free-Solution, Label-Free Molecular Interactions Studied by Back-Scattering Interferometry*, Science **317** 1732-1736 (2007).

[164] C.-Y. Chao, W. Fung and L.J. Guo, *Polymer microring resonators for biochemical sensing applications*, IEEE J. Sel. Top. Quantum Electron. **12** 134-142 (2006).

[165] A. Yalcin, K.C. Popat, J.C. Aldridge, T.A. Desai, J. Hryniewicz, N. Chbouki, B.E. Little, O. King, V. Van, S. Chu, D. Gill, M. Anthes-Washburn and M.S. Unlu, *Optical sensing of biomolecules using microring resonators*, IEEE J. Sel. Top. Quantum Electron. **12** 148-155 (2006).

[166] K. De Vos, I. Bartolozzi, E. Schacht, P. Bienstman and R. Baets, *Silicon-on-Insulator microring resonator for sensitive and label-free biosensing*, Opt. Express **15** 7610-7615 (2007).

[167] A. Ramachandran, S. Wang, J. Clarke, S.J. Ja, D. Goad, L. Wald, E.M. Flood, E. Knobbe, J.V. Hryniewicz, S.T. Chu, D. Gill, W. Chen, O. King and B.E. Little, *A universal biosensing platform based on optical micro-ring resonators*, Biosens. Bioelectron. **23** 939-944 (2008).

[168] A. Ksendzov and Y. Lin, *Integrated optics ring-resonator sensors for protein detection*, Opt. Lett. **30** 3344-3346 (2005).

[169] C.A. Barrios, M.J. Bañuls, V. González-Pedro, K.B. Gylfason, B. Sánchez, A. Griol, A. Maquieira, H. Sohlström, M. Holgado and R. Casquel, *Label-free optical biosensing with slot-waveguides*, Opt. Lett. **33** 708-710 (2008).

[170] N.M. Hanumegowda, C.J. Stica, B.C. Patel, I.M. White and X. Fan, *Refractometric sensors based on microsphere resonators*, Appl. Phys. Lett. **87** 201107 (2005).

[171] F. Vollmer, S. Arnold, D. Braun, I. Teraoka and A. Libchaber, *Multiplexed DNA Quantification by Spectroscopic Shift of Two Microsphere Cavities*, Biophys. J. **85** 1974-1979 (2003).

[172] N.M. Hanumegowda, I.M. White, H. Oveys and X. Fan, *Label-free protease sensors based on optical microsphere resonators*, Sens. Lett. **3** 315-319 (2005).

[173] H. Zhu, J.D. Suter, I.M. White and X. Fan, *Aptamer Based Microsphere Biosensor for Thrombin Detection*, Sensors **6** 785-795 (2006).

[174] S. Arnold, R. Ramjit, D. Keng, V. Kolchenko and I. Teraoka, *MicroParticle photophysics illuminates viral bio-sensing*, Faraday Discuss. **137** 65-83 (2008).

[175] D. Keng, S.R. McAnanama, I. Teraoka and S. Arnold, *Resonance fluctuations of a whispering gallery mode biosensor by particles undergoing Brownian motion*, Appl. Phys. Lett. **91** 103902 (2007).

[176] X. Fan, I.M. White, H. Zhu, J.D. Suter and H. Oveys, *Overview of novel integrated optical ring resonator bio/chemical sensors*, SPIE Laser Resonators and Beam Control X **6452** (2007).

[177] J.D. Suter, I.M. White, H. Zhu, H. Shi, C.W. Caldwell and X. Fan, *Label-free quantitative DNA detection using the liquid core optical ring resonator*, Biosens. Bioelectron. **23** 1003-1009 (2008).

[178] H. Zhu, I.M. White, J.D. Suter, P.S. Dale and X. Fan, *Analysis of biomolecule detection with optofluidic ring resonator sensors*, Opt. Express **15** 9139-9146 (2007).

[179] H. Zhu, I.M. White, J.D. Suter, M. Zourob and X. Fan, *Opto-fluidic micro-ring resonator for sensitive label-free viral detection*, Analyst **133** 356-360 (2008).

[180] K. Schroeder, W. Ecke, R. Mueller, R. Willsch and A. Andreev, *A fibre Bragg grating refractometer*, Meas. Sci. Technol. **12** 757-764 (2001).

[181] K.H. Smith, B.L. Ipson, T.L. Lowder, A.R. Hawkins, R.H. Selfridge and S.M. Schultz, *Surface-relief fiber Bragg gratings for sensing applications*, Appl. Opt. **45** 1669-1675 (2006).

[182] T.L. Lowder, J.D. Gordon, S.M. Schultz and R.H. Selfridge, *Volatile organic compound sensing using a surface-relief D-shaped fiber Bragg grating and a polydimethylsiloxane layer*, Opt. Lett. **32** 2523-2525 (2007).

[183] W. Liang, Y. Huang, Y. Xu, R.K. Lee and A. Yariv, *Highly sensitive fiber Bragg grating refractive index sensors*, Appl. Phys. Lett. **86** 151122 (2005).

[184] A.N. Chryssis, S.M. Lee, S.B. Lee, S.S. Saini and M. Dagenais, *High sensitivity evanescent field fiber Bragg grating sensor*, IEEE Photonics Technol. Lett. **17** 1253-1255 (2005).

[185] A.N. Chryssis, S.S. Saini, S.M. Lee, H. Yi, W.E. Bentley and M. Dagenais, *Detecting hybridization of DNA by highly sensitive evanescent field etched core fiber Bragg grating sensors*, IEEE J. Sel. Top. Quantum Electron. **11** 864-872 (2005).

[186] L. Rindorf, J.B. Jensen, M. Dufva, L.H. Pedersen, P.E. Hoiby and O. Bang, *Photonic crystal fiber long-period gratings for biochemical sensing*, Opt. Express **14** 8224-8231 (2006).

[187] M.P. DeLisa, Z. Zhang, M. Shiloach, S. Pilevar, C.C. Davis, J.S. Sirkis and W.E. Bentley, *Evanescent Wave Long-Period Fiber Bragg Grating as an Immobilized Antibody Biosensor*, Anal. Chem. **72** 2895-2900 (2000).

[188] F. Xu, P. Horak and G. Brambilla, *Optical microfiber coil resonator refractometric sensor: erratum*, Opt. Express **15** 9385-9385 (2007).

[189] H. Tazawa, T. Kanie and M. Katayama, *Fiber-optic coupler based refractive index sensor and its application to biosensing*, Appl. Phys. Lett. **91** 113901 (2007).

[190] W. Liang, Y. Huang, Y. Xu, R.K. Lee and A. Yariv, *Highly sensitive fiber Bragg grating refractive index sensors*, Appl. Phys. Lett. **86** 151122 (2005).

[191] T. Wei, Y. Han, H.-L. Tsai and H. Xiao, *Miniaturized fiber inline Fabry-Perot interferometer fabricated with a femtosecond laser*, Opt. Lett. **33** 536-538 (2008).

[192] X. Wang, K.L. Cooper, A. Wang, J. Xu, Z. Wang, Y. Zhang and Z. Tu, *Label-free DNA sequence detection using oligonucleotide functionalized optical fiber*, Appl. Phys. Lett. **89** 163901 (2006).

[193] Y. Zhang, H. Shibru, K.L. Cooper and A. Wang, *Miniature fiber-optic multicavity Fabry-Perot interferometric biosensor*, Opt. Lett. **30** 1021-1023 (2005).

[194] `http://www.neosensors.com`

[195] H.J. Watts, C.R. Lowe, D.V. Pollard-Knight, *Optical Biosensor for Monitoring Microbial Cells*, Anal. Chem. **66** 2465-2470 (1994).

[196] M. Zourob, S. Mohr, B.J.T. Brown, P.R. Fielden, M.B. McDonnell and N.J. Goddard, *An Integrated Metal Clad Leaky Waveguide Sensor for Detection of Bacteria*, Anal. Chem. **77** 232-242 (2005).

[197] N. Skivesen, R. Horváth, S. Thinggaard, N.B. Larsen and H.C. Pedersen, *Deep-probe metal-clad waveguide biosensors*, Biosens. Bioelectron. **22** 1282-1288 (2007).

[198] R. Horváth, H.C. Pedersen, N. Skivesen, D. Selmeczi and N.B. Larsen, *Optical waveguide sensor for on-line monitoring of bacteria*, Opt. Lett. **28** 1233-1235 (2003).

[199] Y. Wang, H. Li, Z. Cao, T. Yu, Q. Shen and Y. He, *Oscillating wave sensor based on the GoosHnchen effect*, Appl. Phys. Lett. **92** 061117 (2008).

[200] B. Cunningham, P. Li, B. Lin and J. Pepper, *Colorimetric resonant reflection as a direct biochemical assay technique*, Sens. Actuators B Chem. **81** 316-328 (2002).

[201] P.Y. Li, B. Lin, J. Gerstenmaier and B.T. Cunningham, *A new method for label-free imaging of biomolecular interactions*, Sens. Actuators B Chem. **99** 6-13 (2004).

[202] N. Skivesen, A. Têtu, M. Kristensen, J. Kjems, L.H. Frandsen and P.I. Borel, *Photonic-crystal waveguide biosensor*, Opt. Express **15** 3169-3176 (2007).

[203] S. Mandal and D. Erickson, *Nanoscale optofluidic sensor arrays*, Opt. Express **16** 1623-1631 (2008).

[204] L. Rindorf, J.B. Jensen, M. Dufva, L.H. Pedersen, P.E. Hoiby and O. Bang, *Photonic crystal fiber long-period gratings for biochemical sensing*, Opt. Express **14** 8224-8231 (2006).